Dissertation presented to the Instituto Tecnológico de Aeronáutica, in partial fulfillment of the requirements for the degree of Master of Science in the Program of Physics, Field of Plasma Physics.

Helen Caroline de Souza Barros

STUDY OF WO_{3-X} AND g-C_3N_4 PHOTOELECTRODES AIMED AT APPLICATION IN SOLAR HYDROGEN GENERATION

Dissertation approved in its final version the signatories below:

Prof. Dr. André Luis de Jesus Pereira

Advisor

Argemiro Soares da Silva

Prof. Dr. Argemiro Soares da Silva Sobrinho

Co-advisor

Campo Montenegro

São José dos Campos, SP – Brasil

2025

Cataloging-in-Publication Data
Documentation and Information Division

Barros, Helen Caroline de Souza Barros
Study of WO_{3-X} and g-C_3N_4 Photoelectrodes Aimed at Application in Solar Hydrogen Generation/ Helen Caroline de Souza Barros
São José dos Campos, 2025.
104f.

Dissertation of Master of Science – Program in Physics, Field of Plasma Physics – Instituto Tecnológico de Aeronáutica, 2025.
Advisor: Prof. Dr. André Luis de Jesus Pereira
Co-advisor: Prof. Dr. Argemiro Soares da Silva Sobrinho

1. Photoelectrodes 2. Magnetron Sputtering. 3. Green Hydrogen. I. Instituto Tecnológico de Aeronáutica. II. Study of WO_{3-X} and g-C_3N_4 Photoelectrodes Aimed at Application in Solar Hydrogen Generation

BIBLIOGRAPHIC REFERENCE

Barros, Helen. **Study of WO_{3-X} and g-C_3N_4 Photoelectrodes Aimed at Application in Solar Hydrogen Generation**. 2025. 104f. Dissertation of Master of Science in Plasma Physics – Instituto Tecnológico de Aeronáutica, São José dos Campos, 2025.

CESSION OF RIGHTS

AUTOR NAME: Helen Caroline de Souza Barros
PUBLICATION TITLE: Study of WO_{3-X} and g-C_3N_4 Photoelectrodes Aimed at Application in Solar Hydrogen Generation
PUBLICATION KIND/YEAR: Dissertation / 2025

It is granted to Instituto Tecnológico de Aeronáutica permission to reproduce copies of this dissertation to only loan or sell copies for academic and scientific purposes. The author reserves other publication rights and no part of this dissertation can be reproduced without his authorization.

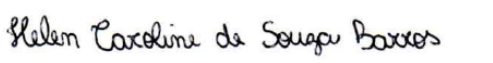

Helen Caroline de Souza Barros
Rua Doutor David Diamante, 236 – Dom Pedro I
CEP: 12232-810, São josé dos Campos SP

STUDY OF WO_{3-X} AND g-C_3N_4 PHOTOELECTRODES AIMED AT APPLICATION IN SOLAR HYDROGEN GENERATION

Helen Caroline de Souza Barros

Thesis Committee Composition:

Prof. Dr.	Douglas Marcel Gonçalves Leite	Chairperson	ITA
Prof. Dr.	André Luis de Jesus Pereira	Advisor	ITA
Prof. Dr.	Argemiro Soares da Silva Sobrinho	Co-advisor	ITA
Prof. Dr.	Luiz Fernando de Araújo Ferrão	Internal Member	ITA
Prof. Dr.	Jose Humberto Dias da Silva	External Member	UNESP

ITA

I dedicate this work to all who take the time to read it, hoping it may contribute to your learning, research, or curiosity.

Acknowledgments

First and foremost, I would like to express my deep gratitude to my family, especially my mother, Vânia, my godmother, Maria do Carmo, and my aunt, Edna Maria, for their unwavering support, encouragement, and presence throughout this journey.

To my love and partner, Marcus, thank you for always being by my side, for your unconditional support, and for enduring all the phases of this path. I love you.

I sincerely thank my advisor, Prof. André, and my co-advisor, Prof. Argemiro, who guided me since my undergraduate research and consistently supported my academic and personal growth.

A special thanks to Prof. Marcilene for all the support, advice, and teachings. Your guidance was essential, and you will always be my role model as a researcher and educator.

To the professors at LPP–ITA, Prof. Rodrigo, Prof. Petraconi, Prof. Douglas, Prof. Argemiro, Prof. André, and Prof. Gilmar, thank you for the knowledge shared and for all your contributions over the years. I also extend my gratitude to the entire LPP – ITA team: Allan, Álvaro, Angélica, Armstrong, Ariane, Bianca, Carla, Carol, Carlão, Cauana, Claudio, Diniz, Eduardo, Filipe, Gabriel, Garufe, Homerinho, Isabela H., Isabella G., Jade, Júlia, Letícia, Luan, Marcelo, Matheus, Miranda, Natali, Nilton, Paulo, Pedro, Rodrigo B., Rodrigo L., Seu Jorge, Thaís and Tia Eliane—thank you for every conversation, help, and shared moment.

I am especially grateful to my master's companion, Rafael, and to Michaela, Maria Gabrielle, Giovana, Mariane, David, and Letícia Carolaine, for all the support, partnership, and encouragement along the way.

I thank my longtime partner in university, work, and the lab, Betinho, who was always present and supportive even over 8,000 km away.

I am also grateful to Prof. Nicolas Martin for his valuable guidance during my exchange program and for his support in adapting to life in France. I extend my thanks to all those at the FEMTO-ST laboratory who contributed both to the research and to my experience in Besançon: Prof. Aurelien Besnard, Prof. Jean Baptiste, Nisrine, Andrei, Guilherme, Vinicius, Marina, Stefania, Fehima, Nicolas B., Guillem, Hamidreza, Lucero, and Aurora.

Finally, I thank the funding agencies CAPES, FAPESP, and CNPq for the financial support that made both the undergraduate research projects and this master’s study possible.

" A scientist in their laboratory is not merely a technician: they are also a child in the presence of natural phenomena, amazed as if witnessing a fairy tale".

(Marie Curie)

Resumo

A conversão direta da luz solar em hidrogênio por meio de células fotoeletroquímicas (PEC) surge como uma das estratégias mais promissoras para a descarbonização do setor energético, ao integrar, em um único dispositivo, a captação fotônica, a separação de cargas e as reações de evolução de H_2/O_2. No entanto, a eficiência global desses sistemas ainda é limitada por fatores como a baixa absorção espectral, a rápida recombinação de pares elétron-buraco e a instabilidade estrutural dos fotoeletrodos. Diante desse cenário, o presente trabalho mapeou de forma sistemática as relações entre as etapas de processamento, as características estruturais e as propriedades resultante de dois semicondutores abundantes, óxido de tungstênio subestequiométrico (WO_{3-x}) e nitreto de carbono grafítico (g-C_3N_4), visando à futura construção de fotoeletrodos *Z-scheme* para geração solar de hidrogênio. Filmes de WO_{3-x} foram depositados por pulverização catódica com rampas de O_2 (2–10 sccm) e pelo *Reactive Gas Pulsing Process* (RGPP) em *duty cycles* de 60 % e 90 % do período. A caracterização por Difração de Raios X (DRX), Espectroscopia Raman, Microscopia eletrônica de Varredura (MEV), Espectroscopia de Impedância Eletroquímica, voltametria cíclica e análises de Mott–Schottky demonstrou que, embora todas as amostras apresentem a fase γ-monoclínica do WO_{3-x}, aquelas obtidas com fluxos intermediários de O_2 (6–8 sccm) exibiram desempenho fotoeletroquímico superior, com menor resistência de transferência de carga, maior capacitância, densidade de energia e fotocorrente sob iluminação AM 1.5 G. No processo RGPP, o *duty cycle* de 90 % do período resultou na formação de filmes colunares e transparentes, enquanto o de 60 % do período produziu camadas mais densas. Essas amostras foram tratadas termicamente em atmosfera ambiente e em fluxo contínuo de argônio, revelando que a atmosfera de tratamento influenciou significativamente a transmitância óptica e as variações do band gap. Após o recozimento, substratos de vidro promoveram à formação de Na_2WO_4, ao passo que os substratos de óxido de estanho dopado com flúor (FTO) atuaram como barreira à difusão iônica, preservando a fase pura de WO_3. Pós de g-C_3N_4 foram obtidos por policondensação térmica da melamina entre 400 °C e 550 °C. Somente a calcinação a 550 °C conferiu as reflexões (100)/(002) em DRX e os modos Raman característicos, indicando estrutura grafítica ordenada adequada para futura deposição em filme ou esfoliação. Os resultados confirmam que o desempenho fotoeletroquímico de cada material depende criticamente do equilíbrio entre ordem cristalina e densidade de defeitos. A partir disso, estabeleceram-se orientações estratégicas para o acoplamento dos materiais: empregar WO_{3-x} moderadamente reduzido (6–8 sccm O_2 ou 60 % e 90 % de P tratados termicamente em

atmosfera de argônio), depositar g-C_3N_4 a 550 °C sobre WO_{3-x}, e utilizar substratos com propriedades difusivas e barreira, como o FTO. Embora a heteroestrutura não tenha sido finalizada, o estudo estabelece janelas ótimas de síntese e requisitos de interface que fundamentam etapas subsequentes rumo a fotoeletrodos compósitos mais eficientes, estáveis e economicamente viáveis para a conversão direta da energia solar em hidrogênio verde.

Abstract

The direct conversion of solar energy into hydrogen through photoelectrochemical (PEC) cells has emerged as one of the most promising strategies for decarbonizing the energy sector, as it integrates into a single device photon harvesting, charge separation, and the hydrogen/oxygen evolution reactions. However, the overall efficiency of these systems remains limited by factors such as low spectral absorption, rapid electron–hole recombination, and structural instability of the photoelectrodes. In this context, the present work systematically mapped the relationships between processing conditions, structural features, and the resulting properties of two earth-abundant semiconductors: sub-stoichiometric tungsten oxide (WO_{3-x}) and graphitic carbon nitride (g-C_3N_4), aiming at the future development of Z-scheme photoelectrodes for solar hydrogen production. WO_{3-x} films were deposited by reactive sputtering with O_2 flow gradients (2–10 sccm) and through the Reactive Gas Pulsing Process (RGPP) with duty cycles of 60% and 90% of the period. Characterization by X-ray Diffraction (XRD), Raman spectroscopy, Scanning Electron Microscopy (SEM), Electrochemical Impedance Spectroscopy (EIS), cyclic voltammetry, and Mott–Schottky analyses demonstrated that, although all samples exhibited the γ-monoclinic phase of WO_{3-x}, those obtained with intermediate O_2 flows (6–8 sccm) showed superior photoelectrochemical performance, including lower charge transfer resistance, higher capacitance, energy density, and photocurrent under AM 1.5 G illumination. In the RGPP process, a 90% duty cycle led to the formation of transparent columnar films, while a 60% duty cycle produced denser layers. These samples were thermally treated in both ambient air and flowing argon, revealing that the annealing atmosphere significantly influenced their optical transmittance and band gap variations. Upon annealing, sodium-containing glass substrates promoted the formation of Na_2WO_4, whereas Fluorine-doped Tin Oxide (FTO) substrates acted as ionic diffusion barriers, preserving the pure WO_3 phase. g-C_3N_4 powders were obtained by thermal polycondensation of melamine between 400 °C and 550 °C. Only calcination at 550 °C yielded (100)/(002) reflections in XRD and the characteristic Raman modes, indicating an ordered graphitic structure suitable for future film deposition. The results confirm that the photoelectrochemical performance of each material critically depends on the balance between crystalline order and defect density. Based on this, strategic guidelines were established for material coupling: employing moderately reduced WO_{3-x} (6–8 sccm O_2 or 60% and 90% of P thermally treated under argon), depositing g-C_3N_4 at 550 °C onto WO_{3-x}. Although the heterostructure has not yet been completed, this study

defines optimal synthesis windows and interfacial requirements that support subsequent stages toward the development of more efficient, stable, and economically viable composite photoelectrodes for the direct conversion of solar energy into green hydrogen.

List of Figures

List of Tables

Contents

1 Introduction

1.1 Contextualization

One of the most pressing challenges faced by humanity today is the development of clean, sustainable energy generation technologies. The widespread use of fossil fuels, particularly since the Industrial Revolution, has led to serious environmental consequences due to the emission of carbon dioxide and other greenhouse gases, which are the primary drivers of global warming [1,2]. The decarbonization of energy systems is one of the key pathways to stabilizing the planet's average temperature, and to prevent an increase of more than 2 °C, global emissions must be zero or negative by the second half of this century [1]. Contrary to this reality, studies indicate a continuous increase in demand, especially from industry, with projections that global energy consumption will rise from ~600 quadrillion British Thermal Units (BTU) in 2018 to ~900 quadrillion BTU in 2050 [2]. In this context, it is essential to develop alternative energy sources that are clean, efficient, cost-effective, and environmentally sustainable.

Among the possible alternatives, solar energy is the largest and most abundant renewable and carbon-free energy source available on Earth [1]. Since the amount of solar energy that reaches the Earth per second exceeds 1.465×10^{14} J (equivalent to the energy generated by ~5 million tons of coal), it becomes the most viable alternative to replace the currently most used energy sources [3]. However, before replacing fossil fuels, it is necessary to find suitable solutions for storing this energy, mainly because solar energy (and other renewable sources) is inherently intermittent. One of the most viable energy storage options is in the form of fuel, as it can be stored for long periods and used when most appropriate [1].

A convenient way to store solar energy is through the process of splitting water (H_2O) into hydrogen (H_2) and oxygen (O_2). This phenomenon, known in the scientific community as water splitting (WS), is inspired by the natural process of photosynthesis, as it uses sunlight to extract electrons from water and store these electrons in high-energy chemical bonds [1]. The energy stored in the H–H chemical bond is easily released in the presence of oxygen, with H_2O and heat being the main products of this reaction [4,5]. In quantitative terms, the combustion of 1 kg of H_2 releases ~142 MJ, whereas the combustion of 1 kg of gasoline produces ~47 MJ [6]. Due to occupying, in the liquid state, ~1/700 of the volume it would occupy in the gaseous state, hydrogen has been used as a fuel for rocket and space capsule propulsion, which require lightweight, compact fuels with high energy storage capacity [6].

Hydrogen produced sustainably is expected to play a fundamental role in the future of both energy systems and the chemical industry. However, one question remains: What is the

most cost-effective method to generate this "solar hydrogen?" According to Oruc and Dincer (2021), several techniques are currently employed for the production of molecular H_2 [5]. Among them, heterogeneous photocatalysis, which splits water molecules using solar radiation that continuously reaches the Earth's surface, is one of the most promising methods. This technique stands out mainly for being environmentally clean and having high cost-effectiveness [7]. Nevertheless, despite promising advances in heterogeneous photocatalysis, there are still some obstacles to overcome, such as the high recombination rate of electron–hole pairs and the low redox kinetics occurring on the surface of the photocatalyst [8]. An interesting strategy to partially overcome these limitations is depositing two types of photocatalysts—usually semiconductors—in thin films on conductive substrates and placing them in a photoelectrochemical cell (Photoelectrochemistry – PEC) [1,8]. This process, which will be explained in more detail in the next section, simultaneously reduces the recombination rate and increases the charge transfer rate at the semiconductor surface, favoring greater efficiency of the WS process [8].

It is estimated that, depending on the technique, the production costs of solar H_2 via PEC cells range from US$1.60 to US$10.40 per kilogram of H_2 [9]. However, as recently pointed out by T. Jesper Jacobsson [10] the best PEC device currently available is still unable to surpass the performance of commercial photovoltaic devices, indicating that there is still a long way to go before PEC technology for H_2 generation becomes a viable reality. From a practical standpoint, several factors must converge to make the PEC-based H_2 generation process both efficient and sustainable. Among these factors, the following can be highlighted [7]:

i – when illuminated by sunlight, the semiconductor must generate a potential of at least 1.23 eV to split the water molecule;

ii – the bandgap of the semiconductor must be small enough to absorb solar radiation;

iii – the valence band (VB) and conduction band (CB) edge potentials at the semiconductor surface must encompass the redox potentials of H and O;

iv – the system must exhibit high stability against corrosion in aqueous electrolytes;

v – Charge transfer at the semiconductor–solution interface must be facilitated to minimize energy losses.

Despite the significant advances in materials science, many research groups worldwide are still searching for materials that can simultaneously fulfill all these criteria while offering a favorable cost-benefit ratio for large-scale applications. In practical terms, the solar-to-hydrogen (STH) conversion efficiency and the device’s operational lifetime are considered the most critical factors influencing the cost of hydrogen fuel. Some authors estimate that PEC cells

will become viable when the STH efficiency exceeds 5% and the device exhibits a lifespan of at least five years [1,11,12]. Additionally, the costs associated with the fabrication of photoelectrodes must always be taken into account [1].

Water splitting via PEC processes was first reported by Fujishima and Honda in 1972 [13], using titanium dioxide (TiO_2) as a light-absorbing photoelectrode, and since then, many studies have been carried out to understand the fundamental processes and enhance the photocatalytic efficiency of TiO_2 [13]. Although it possesses desirable properties from a sustainability perspective, the light absorption of pure TiO_2 is limited to the UV region, as it has a bandgap of 3.2 eV [14]. As a result, most of the solar radiation reaching Earth is not utilized, given that sunlight is composed of approximately ~6.8% UV ($\lambda < 400$ nm), ~38.9% visible ($\lambda = 400–700$ nm), and ~54.3% near-infrared (NIR) ($\lambda = 700–3000$ nm) [15]. This has led to the search for semiconductors with band gaps in the 1.0–2.0 eV range that can promote WS by harvesting a broader portion of the solar spectrum. The first materials to exhibit relatively high efficiency included $GaInP_2$ [16], InP [17], Cu [In, Ga] $[S, Se]_2$ (CIGS) [18], and $CuInS_2$ (CIS) [19]. Combining some of these materials has resulted in WS efficiencies close to the theoretical maximum. However, the fabrication costs of these materials are very high, and some contain elements that are not Earth-abundant, such as indium, which hampers scalability [14]. Thus, real technological advancement in this field is directly linked to the search for catalysts with high catalytic efficiency, selectivity, and effective hydrogen accumulation.

Among the materials explored for photoanode applications, tungsten trioxide (WO_3) stands out due to its stability in acidic media, well-defined crystalline structure, and low production cost [20,21]. WO_3 is an n-type semiconductor with an indirect bandgap ranging from 2.5 to 2.8 eV, allowing it to absorb visible light. However, its performance is limited by the fast recombination of photogenerated electron–hole pairs and suboptimal charge separation. To address these challenges, strategies involving defect engineering and the construction of heterostructures have been proposed [22].

In parallel, graphitic carbon nitride (g-C_3N_4) has gained attention for PEC applications owing to its optical bandgap (~2.6–2.8 eV), structural stability, and simple synthesis routes. Its structure consists of π–π stacked triazine or heptazine rings, and its elemental composition (C and N) contributes to its sustainability [23,24]. Nevertheless, g-C_3N_4 suffers from intrinsic limitations, including low electrical conductivity and rapid charge recombination.

These drawbacks can be mitigated by introducing structural defects or combining g-C_3N_4 with other semiconductors. When integrated with WO_{3-x}, g-C_3N_4 functions as an electron donor, facilitating more efficient charge separation and extending light absorption through

synergistic band alignment. This type-II heterostructure enhances photocatalytic activity, improving hydrogen production and pollutant degradation [22,25].

Although the heterostructures proposed in this study have not yet been experimentally characterized, the independent analyses of WO_{3-x} and g-C_3N_4 provide valuable insights for future material integration and performance optimization [20,26–28].

In this context, the present study evaluates how oxygen gradients and Reactive Gas Pulsing Process (RGPP) parameters influence the structural, optical, and photoelectrochemical properties of WO_{3-x} thin films deposited by magnetron sputtering, while also assessing the performance of g-C_3N_4 produced by thermal polycondensation of melamine. Comparing these results deepens the understanding of the physicochemical mechanisms that govern photoelectrochemical efficiency and lays the foundation for developing advanced composite electrodes geared toward solar hydrogen generation. The following section presents the general and specific objectives that guided this investigation.

1.2 General and Specific Objectives

Given the context of this work, its main objective is the deposition of WO_{3-x} thin films and g-C_3N_4 nanoparticles to evaluate their potential as photoanodes in photoelectrochemical (PEC) cells for hydrogen (H_2) generation using the full solar spectrum. To achieve this goal, the research was guided by the following specific objectives:

- Deposit WO_{3-x} layers on FTO, Si(100), and glass substrates by DC magnetron sputtering while imposing a continuous O_2-flow gradient (2–10 sccm);
- Investigate the structural, morphological, optical, and preliminary electrochemical properties of the oxygen-gradient samples;
- Grow additional WO_{3-x} films via DC magnetron sputtering operated in RGPP mode at duty cycles of 60 % and 90 %, introducing a periodic modulation of the reactive atmosphere.
- Investigate the structural, morphological, optical, and preliminary electrochemical properties of the RGPP samples;
- Produce g-C_3N_4 by thermal polymerization of melamine at selected calcination temperatures (400–550 °C) and assess its crystallinity, bonding environment, and microstructure;
- To assess the photoelectrochemical performance of the WO_{3-x} films through cyclic voltammetry (CV), electrochemical impedance spectroscopy (EIS), and Mott–Schottky analysis in a three-electrode PEC setup.

2 STATE OF THE ART

2.1 Principles of a Photoelectrochemical (PEC) Cell

A PEC cell consists of at least two electrodes responsible for oxidation and reduction independently [29]. **Figure 1** presents the main physical and chemical processes involved in photoinduced processes within a conventional PEC cell. The basic principle of WS in PEC processes is based on collecting solar light to dissociate water molecules into their components ($O_2 + H_2$) with the help of a photocatalyst. The WS phenomenon is based on two half-reactions: i) at the cathode (counter-electrode), the hydrogen evolution reaction (HER) takes place; ii) at the photoanode (working electrode), the oxygen evolution reaction (OER) occurs. In a conventional PEC cell, photoanode irradiation induces intrinsic ionization of the photoanode, producing electrons (e^-) in the CB and holes (h^+) in the VB:

$$2hv \rightarrow 2e^- + 2h^+ \qquad \textbf{R.1}$$

The photogenerated holes are responsible for one of the half-reactions, oxidizing and splitting water into O_2 and H^+ ions:

$$2h^+ + H_2O \rightarrow \tfrac{1}{2}O_2(g) + 2H^+ \qquad \textbf{R.2}$$

The photogenerated electrons in the anode are transferred to the cathode through an external electrical circuit. The H^+ ions reach the cathode by crossing (when applicable) an ion-exchange membrane and are reduced, producing gaseous H_2:

$$2H^+ + 2e^- \rightarrow H_2(g) \qquad \textbf{R.3}$$

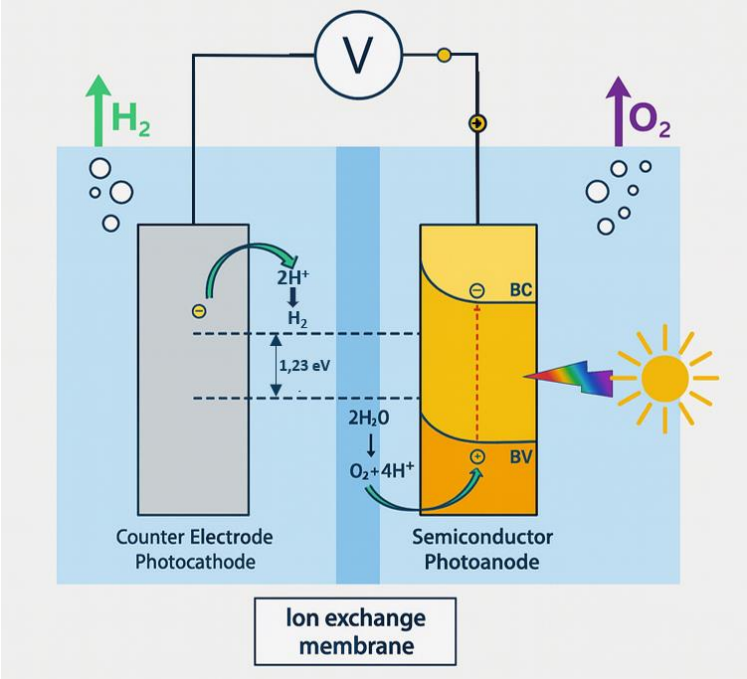

Figure 1 - Energy diagram of a typical PEC cell. Adapted from YAO et al., 2018 [29]

In the presence of light, semiconductors absorb photons with energy equal to or greater than their respective band gaps, generating photocarriers. Under the action of an electric field induced at the semiconductor/electrolyte interface (Ein), charges are separated, resulting in the appearance of a photovoltage (Vph) that is responsible for the electrochemical reactions [29]. Thermodynamically, for water molecule splitting to occur, the following relationship must be satisfied:

$$H_2O\ (liquid) + 237.2\ kJ{\cdot}mol^{-1}\ (Vph) + 48.6\ kJ{\cdot}mol^{-1}\ (heat) \rightarrow H_2 + \tfrac{1}{2}O_2 \quad \textbf{R.3}$$

This relationship indicates that a certain amount of potential energy and heat will be stored in the H_2 molecules after the WS process. The Gibbs free energy of 237.2 $kJ{\cdot}mol^{-1}$ can be converted into 1.23 eV per electron, the minimum value of Vph required for water splitting into H_2 and O_2. [14].

To drive the reaction effectively, an extra potential (overpotential) is necessary, which is converted into heat and stored in the H_2 molecules. [14]. The total energy of 285.8 $kJ{\cdot}mol^{-1}$ (1.48 eV) is the theoretical minimum potential for an electrolytic cell to operate at 25 °C [14]. In practice, potential losses due to resistance throughout the cell must also be considered [29]. The energy stored as heat is usually extracted from the environment and becomes relevant only

when H_2 is used for combustion. Conventionally, to calculate WS process efficiency, only the potential of 1.23 eV is used [14].

In a PEC cell, this energy is obtained through light absorption, meaning that photons with energy of at least 1.23 eV (wavelengths <1010 nm) per electron are required for the entire WS process to occur. The theoretical maximum photovoltage that a semiconductor can generate is ~400 mV below the bandgap energy [30], indicating that the bandgap of the semiconductor used should be >1.6 eV for the reaction to occur at a reasonable rate. However, the higher the bandgap value, the lower the amount of light that can be absorbed and, consequently, the lower the efficiency of the PEC cell under sunlight [14]. Therefore, to design a PEC cell with acceptable efficiency, a balance must exist between the bandgap energy of the semiconductor and the spectral region of light absorbed.

2.2 WO_{3-x} compounds and thin films

Tungsten trioxide (WO_3) is a transition metal oxide of significant scientific and technological relevance, mainly due to its photocatalytic, electrochromic, and photoelectrochemical properties [23,31,32]. Composed of tungsten in a +6 oxidation state coordinated by oxygen atoms, WO_3 forms a framework of WO_6 octahedra. These octahedra are distorted and variably connected, resulting in various structural polymorphs (**Figure 2**). The importance of WO_3 arises from its band structure, chemical stability, visible light absorption, and compatibility with large-scale deposition techniques such as sputtering [33].

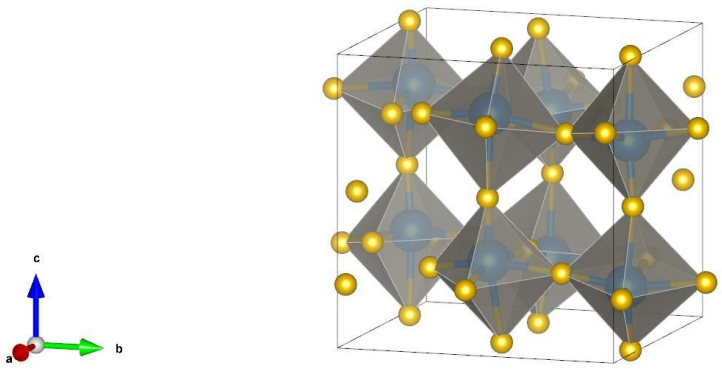

Figure 2 - Crystal structure of monoclinic WO_3, composed of corner-sharing WO_6 octahedra. Tungsten atoms are shown in blue and oxygen atoms in yellow. Structure rendered using VESTA based on crystallographic data from the ICSD (PDF 01-089-4476).

Structurally, WO_3 is known for its rich polymorphism, exhibiting several crystalline phases that depend on temperature and preparation conditions. These include monoclinic (γ-WO_3), triclinic, orthorhombic, tetragonal, and cubic forms [23,33]. Among them, monoclinic WO_3 is the most stable phase at room temperature and is widely used in PEC research due to its optimal charge transport characteristics and higher density of active sites [21,34]. Less stable phases may emerge at high temperatures or under specific synthesis conditions and tend to revert to the monoclinic form upon cooling or annealing [23,33].

From an electronic perspective, WO_3 is an n-type semiconductor with an indirect bandgap typically ranging from 2.6 to 2.8 eV [23,33,35]. Its valence band is primarily composed of O 2p orbitals, while the conduction band originates from W 5d states. This configuration enables the generation of electron–hole pairs under visible light, where holes can participate in the oxygen evolution reaction (OER) [32].

The synthesis of WO_3 can be achieved through various techniques, including sol-gel [36], hydrothermal [34], spray deposition [37], and, particularly, DC reactive magnetron sputtering. Sputtering enables high uniformity, precise control of stoichiometry, and compatibility with large-area substrates [23,36]. In this process, a tungsten target is sputtered in the presence of an Ar/O_2 plasma, and the oxygen partial pressure is finely tuned to yield stoichiometric WO_3. Parameters such as substrate temperature, deposition rate, and post-deposition annealing influence the crystallinity, texture, and phase purity of the films.

The physico-chemical properties of WO_3 include high thermal and chemical stability in acidic environments, excellent optical transparency in the visible region, and good electron mobility along specific crystallographic directions [23,37]. Its compact morphology, when deposited by sputtering, provides high adhesion and long-term operational durability. These attributes are beneficial in PEC cells, where WO_3 films function as photoanodes for water oxidation [34].

The first reported use of WO_3 as a photoanode in a PEC cell was in 1976 by Hodes et al., who demonstrated its capacity for anodic photocurrent generation under UV illumination in aqueous electrolytes. This study marked a milestone in PEC research and positioned WO_3 as a foundational material for photoelectrodes [38].

WO_3 photoanodes have demonstrated promising performance under solar illumination. Their stability in acidic media, fast hole transport, and ease of integration into multilayer structures are key advantages. However, limitations include low quantum efficiency in the red region of the spectrum, a narrow absorption range, and an insufficient conduction band position for hydrogen generation. Furthermore, photogenerated holes may recombine rapidly with electrons if not efficiently extracted, reducing overall PEC efficiency [32,35].

Recent research efforts have focused on overcoming these limitations by coupling WO_3 with co-catalysts, forming heterojunctions with other semiconductors, and engineering its surface to enhance charge separation [23,33]. The incorporation of nanostructuring strategies and plasmonic elements is also under exploration. These modifications aim to increase light harvesting, reduce recombination losses, and extend the functional range of WO_3-based systems [39].

Despite being nominally stoichiometric, WO_3 often exhibits slight oxygen deficiencies, which impact its electronic and catalytic properties. These sub-stoichiometric phases, referred to as WO_{3-x}, will be addressed in detail in the following section. Their controlled formation opens new pathways for defect engineering and performance optimization in PEC and photocatalytic applications, thus bridging the gap between intrinsic material properties and device-level functionalities.

2.2.1 Defect Engineering and Oxygen Vacancies in WO_{3-x}

Oxygen vacancies (O_v) are intrinsic point defects that arise from the absence of oxygen atoms in the crystal lattice of transition metal oxides, such as tungsten trioxide (WO_3). These vacancies play a crucial role in tuning the electronic, structural, and surface properties of WO_{3-x}, particularly in its applications as a photoanode in photoelectrochemical (PEC) water splitting

[40,41]. In stoichiometric WO_3, each tungsten atom is coordinated by six oxygen atoms arranged in distorted WO_6 octahedra [40,41]. When one or more of these oxygen atoms are missing, localized excess electrons appear, typically linked to the partial reduction of W^{6+} to W^{5+}. These vacancies introduce shallow donor states near the conduction band minimum (CBM), modifying the band structure, increasing n-type conductivity, shifting the Fermi level, and enhancing charge carrier density [20,40,41]. Therefore, oxygen vacancies are potent tools for adjusting the structural and electronic properties of WO_3, which is particularly relevant for applications in photoelectrochemical (PEC) water splitting.

Historically, oxygen-deficient tungsten oxides have been studied since the mid-20th century, but only in recent decades have advances in techniques such as X-ray photoelectron spectroscopy (XPS), electron paramagnetic resonance (EPR), and density functional theory (DFT) simulations enabled a mechanistic understanding of their roles [42,43]. These studies have shown that O_v induce bandgap narrowing due to mid-gap states and can give rise to quasi-metallic behavior when present in high densities. Moreover, the structural changes resulting from O_v formation include local lattice distortions, increased surface energy, and often the formation of nanostructured morphologies with high specific surface areas. Such morphological changes further enhance the surface reactivity of WO_3, benefiting charge transfer and catalytic reactions [20,43].

Vacancy engineering strategies in the literature typically involve modulation of the oxygen content during deposition or through post-treatment. Reactive DC magnetron sputtering, for instance, allows for the synthesis of sub-stoichiometric WO_{3-x} films by adjusting the O_2/Ar ratio in the plasma environment [44]. Several studies report the use of distinct and fixed oxygen flow conditions (e.g., 10%, 20%, 40% O_2) to produce films with varying vacancy concentrations and assess their influence on optical, electronic, and photoelectrochemical properties [43]. In this work, a continuous modulation of the oxygen flow rate was applied throughout the deposition process, allowing the formation of a graded defect profile across the film thickness. Although this specific approach has been less frequently reported in the literature, it offers a promising route for investigating the correlation between oxygen vacancy distribution and functional properties.

Beyond flow modulation strategies, an advanced method for controlling the spatial and temporal distribution of oxygen vacancies is the Reactive Gas Pulsing Process (RGPP) [31,45,46]. Unlike continuous sputtering, RGPP introduces oxygen in periodic pulses, enabling precise control over the plasma chemistry at the substrate surface. This technique is particularly suitable for producing layered architectures with alternating stoichiometry or tailored defect

profiles [31,45–47] . In this study, RGPP was employed to synthesize WO_{3-x} thin films using pulsed oxygen injection sequences with specific duty cycles.

Post-deposition treatments can further modulate the population and stability of oxygen vacancies. Annealing in reducing atmospheres (e.g., H_2, Ar/H_2) and doping with aliovalent cations are commonly used to either promote or stabilize sub-stoichiometric states [48,49]. These strategies complement in situ deposition approaches and provide additional flexibility for tuning surface and bulk defect densities.

From a functional perspective, oxygen vacancies have a strong influence on the PEC behavior of WO_{3-x}. Vacancy-rich films exhibit increased electrical conductivity, bandgap narrowing, Fermi level shifts, and improved visible-light absorption. Zhang et al. (2017) [50] demonstrated that WO_{3-x} nanoplates achieved photocurrent densities of 2.15 $mA \cdot cm^{-2}$ at 1.23 V vs. RHE under AM 1.5G illumination—approximately 60% higher than their stoichiometric counterparts. Similarly, Zhan et al. (2019) reported a cathodic shift of −0.15 V in onset potential and a 1.6-fold increase in incident photon-to-current efficiency (IPCE) due to thermally induced oxygen vacancies [51].

However, an excessive concentration of surface vacancies can act as recombination centers, potentially counteracting the benefits of enhanced conductivity and carrier mobility. Stability under prolonged operation, especially in acidic or alkaline electrolytes, also remains a challenge, as surface defects may evolve or become passivated over time [50,52].

Looking ahead, integrating WO_{3-x} into heterojunctions, such as with graphitic carbon nitride ($g\text{-}C_3N_4$) or bismuth vanadate ($BiVO_4$), has shown promise for synergistic improvements in light harvesting and carrier dynamics, according to reports by Li et al. (2025) and Yelan Cheng et al. (2025) [40,53]. Such composite systems can leverage the benefits of engineered O_V while mitigating their downsides. Therefore, oxygen vacancy engineering stands as a critical pathway for the development of next-generation photoanodes and photocatalysts based on tungsten oxide.

2.3 Graphitic Carbon Nitride ($g\text{-}C_3N_4$)

Graphitic carbon nitride ($g\text{-}C_3N_4$) is a polymeric semiconductor composed primarily of carbon and nitrogen atoms arranged in a two-dimensional (2D) layered structure (**Figure 3**). It is structurally derived from tri-s-triazine (C_6N_7) units, forming a planar network held together by van der Waals forces [54,55]. Its molecular structure confers high thermal and chemical stability, and its composition from earth-abundant elements makes it an environmentally

friendly and cost-effective material for photocatalytic and photoelectrochemical applications [26].

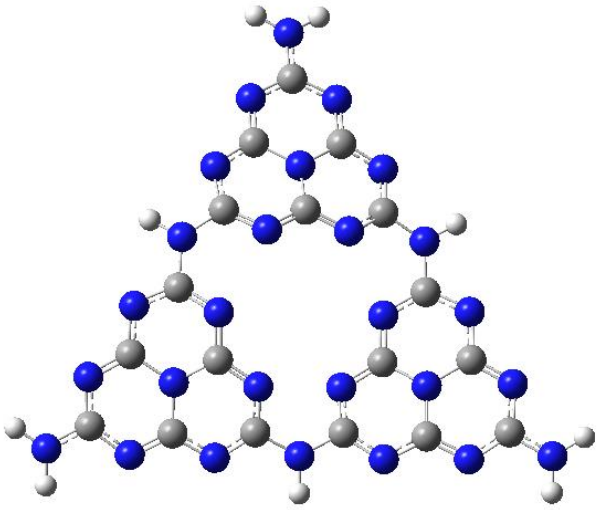

Figure 3 - Molecular model of graphitic carbon nitride (g-C_3N_4). Carbon atoms are depicted in grey, nitrogen in blue, and terminal hydrogen atoms in white.

The electronic structure of g-C_3N_4 is characterized by a moderate bandgap, typically in the range of 2.6 to 2.8 eV, which allows the absorption of visible light up to ~450 nm [54–56]. The valence band is mainly composed of nitrogen 2p orbitals, while the conduction band originates from carbon 2p orbitals, resulting in a band alignment suitable for the reduction of water to hydrogen under illumination [27,55]. However, the conduction band edge of pristine g-C_3N_4 is not sufficiently negative to efficiently drive the hydrogen evolution reaction (HER) without modification or coupling with co-catalysts [26].

In terms of stoichiometry, g-C_3N_4 is often approximated as C_3N_4; however, in practice, it frequently exhibits structural imperfections and partial polymerization, resulting in a degree of disorder that can impact its optoelectronic behavior. These imperfections, such as nitrogen vacancies or carbon-rich domains, can be exploited to enhance photocatalytic performance through defect engineering [27,57].

g-C_3N_4 has been explored in a wide array of applications, including pollutant degradation, CO_2 reduction, antibacterial surfaces, and, more recently, in photoelectrochemical water splitting [22,55,58]. As a photocatalyst, it is commonly synthesized in powder form and dispersed in aqueous media. However, recent efforts have been made to immobilize g-C_3N_4 onto conductive substrates to serve as photoelectrodes in PEC systems, although this

application is still emerging and faces challenges such as poor conductivity and weak adhesion to substrates [26].

The most common synthetic routes for g-C_3N_4 involve thermal polycondensation of nitrogen-rich precursors such as melamine, urea, thiourea, or dicyandiamide [54,56,57]. Among these, melamine is the most frequently used due to its well-defined molecular structure and high nitrogen content. The synthesis typically involves calcination in a muffle furnace at temperatures ranging from 450 to 600°C under air or inert atmospheres, yielding a yellow powder with layered morphology [54,59].

Polycondensation mechanism from melamine to g-C_3N_4. During heating, melamine first dimerizes to melam via elimination of ammonia (NH_3). Subsequent intramolecular rearrangement yields melem, whose core consists of a heptazine ring (also termed *tri-s-triazine*, C_6N_7). Continued deamination links multiple heptazine units into one-dimensional melon chains, which finally condense laterally above ~520 °C to produce the fully conjugated 2D network of g-C_3N_4. In this sequence the triazine ring (C_3N_3) serves as the basic aromatic motif in melamine, while the heptazine ring becomes the structural backbone of the final material. **Figure 4** summarises these key intermediates and the stepwise release of NH_3 that drives the reaction forward [60,61].

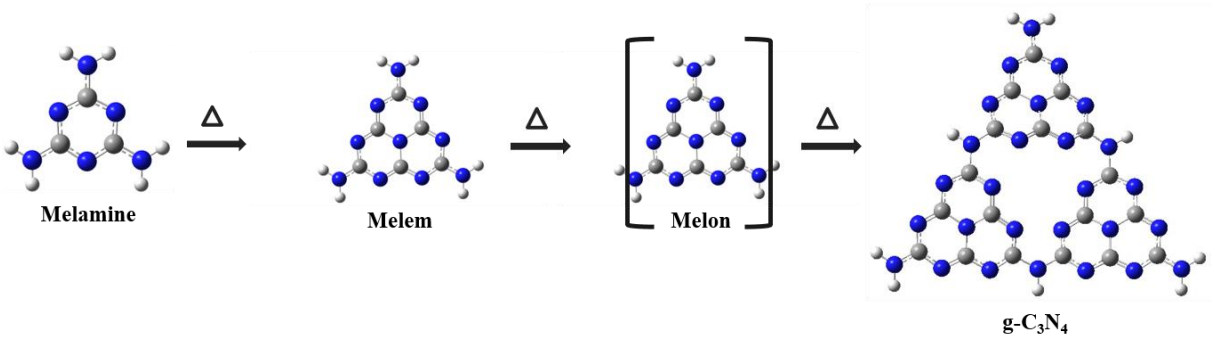

Figure 4 - Schematic representation of the thermal polycondensation pathway from melamine to graphitic carbon nitride (g-C_3N_4). Blue, grey, and white spheres represent nitrogen, carbon, and hydrogen atoms, respectively. Adapted from Alaghmandfard et al, 2022 [60]

The gradual aromatization and growth of π-conjugation during polycondensation narrow the bandgap slightly and introduce defect sites (e.g., −NH− bridges and =N− vacancies) that can modulate charge transport. Kinetic parameters such as heating rate, dwell time, and ambient atmosphere critically influence the crystallinity, porosity, and defect density of the resulting g-C_3N_4, thereby tuning its photocatalytic performance [54,60].

Several factors, including crystallinity, morphology, surface area, and defect concentration, govern the photocatalytic performance of g-C_3N_4. Various modifications have been proposed to overcome its inherent limitations, such as rapid charge recombination and limited light absorption. These include doping with metals or non-metals, formation of heterojunctions with other semiconductors, and textural modifications like exfoliation and templating [26,55].

Overall, g-C_3N_4 represents a promising platform for sustainable photocatalysis and, with further development, for PEC hydrogen production. Its non-toxic nature, facile synthesis, and tunable properties make it a valuable candidate for integration with other semiconductors, such as WO_3, in composite photoelectrodes for efficient solar-driven water splitting [27,54,55].

2.4 WO_3/g-C_3N_4 Heterostructures for Enhanced Hydrogen Production

Semiconductor heterostructures for photocatalysis have garnered increasing attention in the field of sustainable hydrogen production due to their ability to optimize electron–hole pair separation and enhance the efficiency of light-induced redox processes [62,63]. These structures consist of two or more semiconductors with distinct energy bands, enabling the formation of interfaces that facilitate charge transfer and reduce carrier recombination [27]. In particular, heterostructures formed by tungsten oxide (WO_3) and graphitic carbon nitride (g-C_3N_4) have emerged as promising systems for photoelectrochemical applications [63].

Historically, the concept of semiconductor heterostructures was established within the domain of solid-state physics and has since been extensively utilized in electronic and optoelectronic devices [64]. The application of heterostructures in photocatalysis emerged subsequently, marked by a pivotal contribution from Fujishima and Honda in 1972, who introduced the TiO_2/Pt system for water splitting [13,62]. Since that time, various semiconductors have been integrated into heterostructures to improve hydrogen evolution performance [25,63].

Heterostructures can be systematically categorized into three principal types: type I, type II, and the Z-scheme, as described by Chen et al. (2024) [65]. Type I heterostructures tend to accumulate both electrons and holes within the same material, thereby promoting recombination due to the absence of a driving force for charge separation [63]. In the case of type II heterostructures, the conduction band minimum (CBM) and valence band maximum (VBM) of one semiconductor are situated at lower energy levels compared to those of the other, facilitating the migration of electrons to the lower CBM and the movement of holes to the higher

VBM [63,64]. This phenomenon results in spatial charge separation; however, it also diminishes the redox effectiveness [64] . Conversely, the Z-scheme model emulates the electron transfer mechanism observed in natural photosynthesis. In this model, photogenerated electrons from the conduction band of the less oxidative semiconductor recombine with holes from the valence band of the more reductive semiconductor at a solid–solid interface or an electron mediator [65]. This model effectively retains the electrons with higher reductive power and holes with greater oxidative potential within their respective semiconductors [63]. The designation "Z-scheme" originates from the zigzag configuration depicted in the energy diagram, which illustrates the two-step photoexcitation and recombination pathway. This concept was initially proposed by Bard in 1979 for the advancement of artificial photosynthesis systems [64,65]

In the specific case of WO_3 and g-C_3N_4, recent studies have indicated that these materials predominantly form Z-scheme heterostructures, particularly when WO_3 presents oxygen vacancies (WO_{3-x}) [28]. These vacancies facilitate electron transfer from the conduction band of WO_3 to the valence band of g-C_3N_4, thereby allowing both materials to sustain their significant redox potential and enhance the efficiency of photoinduced reactions [63].

Their complementary properties justify the combination of WO_3 and g-C_3N_4 [65]. WO_3 demonstrates strong oxidative capacity (Egap between 2.4 and 2.8 eV), while g-C_3N_4 displays good reducing capability and visible-light absorption (Egap ~ 2.7 eV) [27]. By integrating these semiconductors, individual limitations—such as rapid charge recombination in g-C_3N_4 and the positively shifted conduction band of WO_3—are overcome, resulting in improved photocatalytic activity [64].

From a structural perspective, HRTEM and XPS analyses confirm the formation of 2D/2D interfaces between the materials, which facilitate efficient charge transfer [64]. Oxygen vacancies in WO_{3-x} serve as electron trapping sites and modulate energy levels, broadening the spectral absorption and enhancing carrier separation [28].

The physicochemical properties of these heterostructures include high surface area, strong thermal and chemical stability, broad visible-light absorption, and enhanced redox capacity [26]. Electrochemical tests such as electrochemical impedance spectroscopy (EIS) and photocurrent measurements indicate reduced charge transfer resistance and improved electron–hole separation compared to isolated materials [25,66].

Among the main advantages of WO_3/g-C_3N_4 systems are their low cost, abundance of precursors, facile synthesis, and chemical robustness [62]. However, challenges remain

regarding precise control of the heterointerface, long-term stability of WO_{3-x} phases, and scalable reproducibility [25].

Recent studies have reported significant improvements in hydrogen evolution under visible light, with rates up to five times higher than those of individual semiconductors and excellent stability across multiple cycles [63]. In addition to hydrogen production, selective hydrocarbon oxidation and pollutant degradation have also been demonstrated [64].

Current trends focus on defect engineering, metal doping, and coupling with plasmonic nanoparticles [65]. Despite the progress, there is a lack of studies directly correlating interfacial structure with in situ spectroscopic data and performance under simulated sunlight [27]. Moreover, further efforts are required to develop integrated devices and long-term operational studies for industrial-scale applications [66].

3 MATERIALS AND METHODS

3.1 DC Magnetron Sputtering

Magnetron sputtering is a physical vapour deposition process in which the film grows from the ejection of atoms off a cathodic target bombarded by ions; the phenomenon is sustained by a self-consistent plasma maintained at pressures of 10^{-3}–10^{-2} Torr. Under such rarefied conditions, free electrons are accelerated by the negative electric field applied to the cathode and, upon colliding with neutral argon atoms, generate new ionised species that sustain the glow discharge; this mechanism establishes a dynamic equilibrium in which the electron density reaches 10^{16}–10^{18} m^{-3} while the heavy species remain close to room temperature, a regime commonly referred to as a low-temperature or “cold” plasma [67] . In contrast to thermal plasmas—where electrons, ions and neutrals share temperatures of several thousand kelvin—the non-thermal regime employed in sputtering enables intense chemical activation without imposing significant thermal load on the substrate [67] .

Once the discharge is established, Ar^+ ions are accelerated towards the metallic target by the high negative potential (~ 300–600 V) applied to the cathode. The momentum transfer that occurs during ion–target collisions dislodge neutral atoms from the surface—a phenomenon known as sputtering—which then traverse the chamber’s free path and condense on the substrate, forming the thin film [68]. The distinctive feature of magnetron sputtering lies in the introduction of a magnetic field parallel to the target by permanent magnets; the field forces electrons into tangential helical trajectories, confining them near the surface and drastically increasing the probability of ionizing collisions. This “magnetic trap” raises the local

plasma density, allows operation at even lower pressures, boosts the deposition rate, reduces substrate heating and generates the characteristic racetrack erosion profile, as illustrated in **Figure 5**.

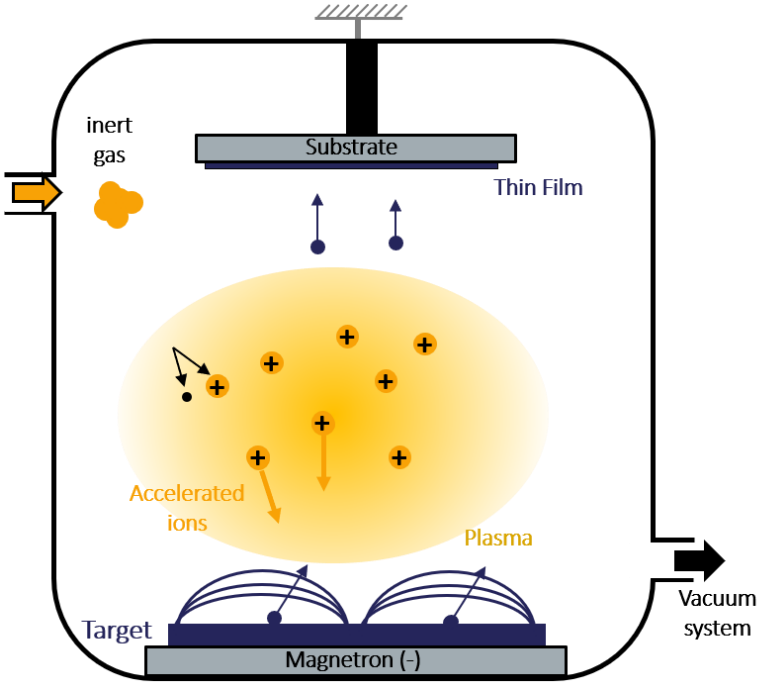

Figure 5 - Schematic illustration of the magnetron sputtering deposition process.

The process can operate in DC mode for conductive targets or in RF mode (13.56 MHz) when sputtering insulators, since the alternating polarity prevents surface charging. More recent advances include HiPIMS, in which power pulses in the $kW.cm^{-2}$ range generate highly ionized plasmas that favors denser, better-adhering films, as reviewed by Anders [68]. The method's flexibility is further expanded by reactive sputtering, wherein gases such as O_2 or N_2 are introduced and react chemically with the metallic flux to form compounds directly during deposition; the associated hysteresis phenomena and control mechanisms in reactive atmospheres have been analysed by Depla et al [69] .

From an application standpoint, magnetron sputtering is valued for its ability to produce coatings of high purity, excellent adhesion, and fine control of thickness and stoichiometry, enabling the fabrication of transparent electrodes, diffusion barriers in semiconductors, and functional films for photoelectrochemical devices. Comprehensive reviews published recently identify remaining challenges, such as mitigating defects induced by ion bombardment and scaling HiPIMS configurations to industrial throughput, yet concur in positioning the technique as a cornerstone of thin-film engineering in the near future [68].

3.2 Deposition of WO_{3-x} thin films by DC Magnetron Sputtering

Tungsten oxide thin films were deposited on glass, silicon (100), and fluorine-doped tin oxide (FTO) substrates. Before deposition, the substrates were pre-cleaned in an ultrasonic bath using acetone and ethanol for 10 minutes each to remove surface contaminants and ensure proper film adhesion.

The deposition process was carried out using a DC dual magnetron sputtering system (**Figure 6(a)**), equipped with a 100 mm diameter tungsten target with 99% purity (**Figure 6(b)**). Before deposition, the chamber was evacuated to a residual pressure of approximately 10^{-6} torr using a turbomolecular pump backed by a mechanical pump to ensure a clean and controlled environment. The process was conducted under controlled conditions: a fixed target power of 150 W, an argon flow of 10 sccm, a deposition time of 60 minutes, and an ambient substrate temperature.

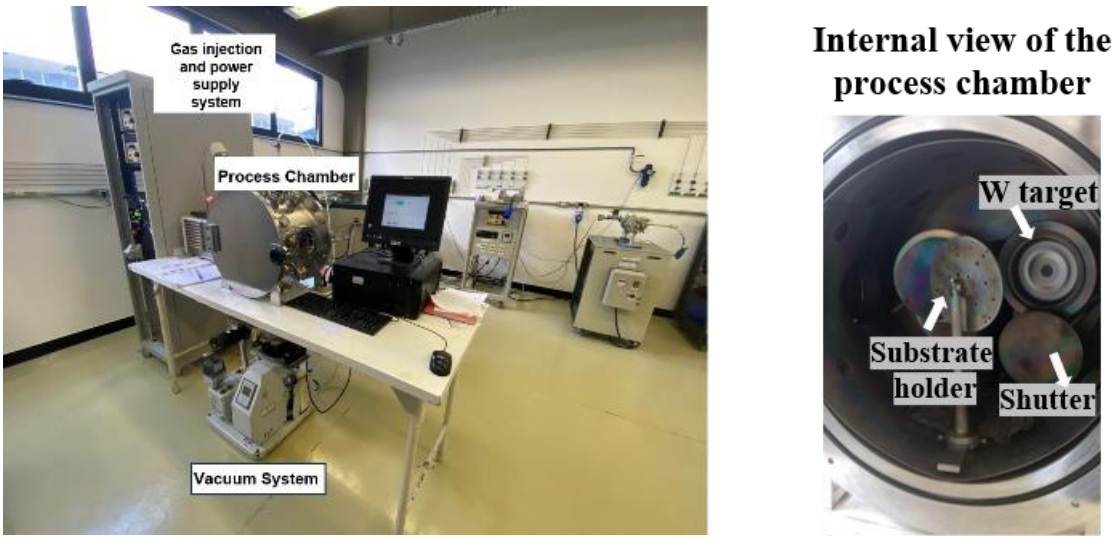

(**a**) (**b**)

Figure 6 – (a) DC dual magnetron sputtering system used for thin film deposition. (b) Internal view of the deposition chamber showing the tungsten target and the substrate holder arrangement.

To induce an oxygen gradient in the WO_{3-x} films, a ramped oxygen flow was applied during the deposition process. The oxygen flow was initially set to specific starting values (2, 4, 6, or 8 sccm) and then gradually increased to a maximum of 10 sccm over 60 minutes, using a dynamic gas flow controller. This procedure created a controlled ramp of oxygen flow throughout the deposition. Additionally, a control sample was prepared under constant

conditions, with the oxygen flow maintained at 10 sccm throughout the entire deposition process.After deposition, the samples were heat-treated for 2 hours at 450 °C with a heating rate of 1°C/min in an ambient atmosphere. This post-deposition annealing step, while essential for structural stabilization, may have promoted partial or total reoxidation of the films, particularly in the upper layers. As a result, the oxygen stoichiometry gradient initially induced during deposition could have been attenuated or even eliminated in some samples. This factor should be taken into account when interpreting the subsequent structural, optical, and functional characterizations. The resulting samples were labeled as WO_{3-x}–2, WO_{3-x}–4, WO_{3-x}–6, WO_{3-x}–8, and WO_{3-x}–10, corresponding to the initial oxygen flow in sccm used during deposition.

3.3 Deposition of WO_{3-x} thin films by DC Magnetron Sputtering and Reactive Gas Pulsing Process (RGPP)

The deposition of tungsten oxide (WO_{3-x}) thin films by the Reactive Gas Pulsing Process (RGPP) was carried out during a master's research internship, under the supervision of Prof. Dr. Nicolas Martin, in collaboration with the FEMTO-ST laboratory in France. This stage was made possible through a research internship scholarship abroad and was conducted using a DC magnetron sputtering system equipped with RGPP, a resource not available at the home laboratory in Brazil.

This investigation continued the study previously initiated using an oxygen gradient deposition approach (described in Section 3.2), and expanded it by employing the Reactive Gas Pulsing Process (RGPP) to enable precise control over oxygen incorporation during film growth, aiming to modulate stoichiometry and oxygen vacancy density.

3.3.1 Hysteresis Study and Definition of the Operating Regime

Prior to deposition, a hysteresis curve study was conducted to determine the operating parameters in the stable reactive regime.

To carry out this study, a test deposition was conducted using a custom-built DC reactive magnetron sputtering system, equipped with a 2-inch tungsten target with a purity of 99.9 %. (illustrated in **Figure 7(a)**, along with the internal view of the deposition chamber shown in **Figure 7(b)**). Before deposition, the chamber was evacuated to an final pressure of approximately 10^{-7} mbar using a turbomolecular pump backed by a mechanical pump to ensure a clean and controlled environment for the sputtering process under controlled conditions: A fixed current of 100 mA, an argon flow of 13% of 20 sccm (2.6 sccm), and a pumping speed of

13 L/s. The oxygen flow was increased by 1% every 2 minutes, ranging from 0 to 15% of 20 sccm, and then this percentage was reduced every 1% intervals until returning to zero. Throughout the process, the total system pressure and the voltage at the tungsten target were recorded every two minutes.

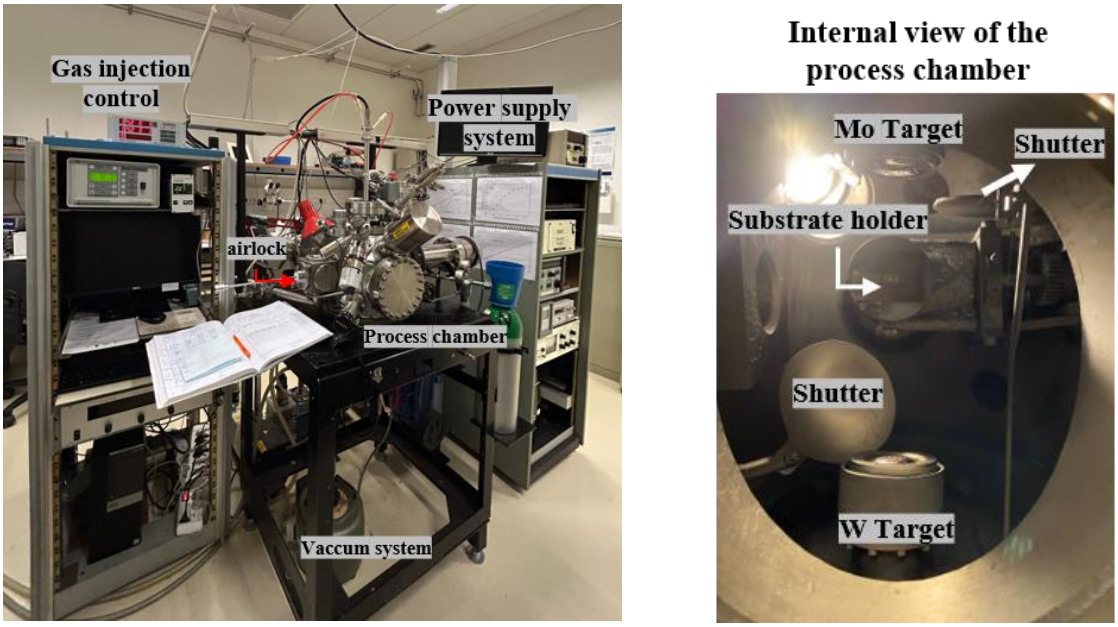

(**a**) (**b**)

Figure 7 – (a) DC magnetron sputtering system used for the deposition of WO_{3-x} films via Reactive Gas Pulsing Process (RGPP). (b) Internal view of the deposition chamber showing the tungsten target and the substrate holder arrangement.

The results obtained from the test deposition are illustrated in **Figure 8**. At the beginning of the deposition, without the presence of oxygen, the potential of the tungsten target is 311 V, corresponding to a completely metallic film. With the initiation of oxygen gas injection, the potential increases to 338 V and continues to rise gradually until reaching a maximum of 498 V for an oxygen flow of 14%. As for the total system pressure, with the start of oxygen injection, there is a decrease from 2.79×10^{-3} to 2.34×10^{-3} mbar at 2% oxygen flow, and then it begins to increase until it reaches a maximum value of 3.54×10^{-3} mbar at 14% oxygen flow, continuing to rise as the oxygen flow decreases. To guarantee a stable operation in the reactive mode, the oxygen flow chosen for the next experiments was set to 14% of 20 sccm (2.8 sccm).

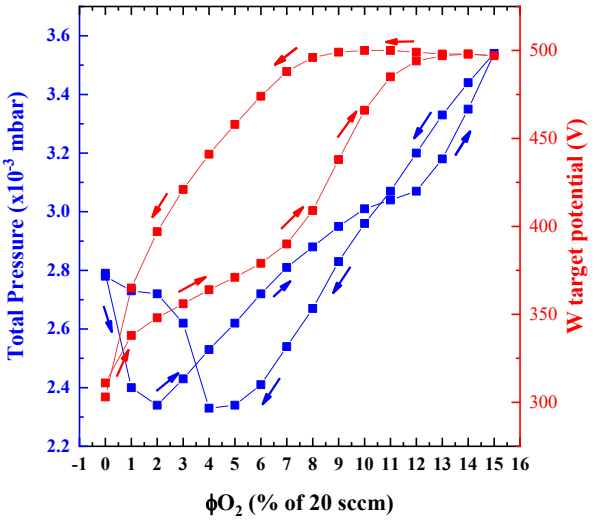

Figure 8 - Hysteresis curve of the sputtering system showing the evolution of total pressure and target voltage as a function of oxygen flow rate.

3.3.2 Choosing a period (P)

The objective of this experiment was to determine the ideal pulsing period (P) to ensure complete and stable alternation between the metallic and oxidized modes during the reactive sputtering process of tungsten. The methodology employed consisted of using an oxygen flow varying between a maximum of 2.8 sccm and a minimum of 0 sccm, a pumping speed (S) of 13 L/s, and a duty cycle fixed set at 50% of P. The duty cycle is defined as the ratio of the Ton (the time during which oxygen is actively injected) to the total pulsing period (P), expressed as dc=Ton/T. Ton and Toff represent, respectively, the duration of maximum oxygen flow and the absence of oxygen during the pulsing cycle [46]. An illustrative example of the oxygen pulsing profile is shown in **Figure 9(b)**, which helps to visualize the alternation between ON and OFF segments during the gas pulsing cycle

The results of the experiment are presented in **Figure 9(a)** indicated that the Tcrossover, the time required for the system to fully alternate between the metallic and oxidized modes, is approximately 10 seconds. To ensure greater stability and allow for complete transitions, 50% of Tcrossover was added, resulting in an ideal pulsing period of 15 seconds, as the final recommended parameter for future experiments.

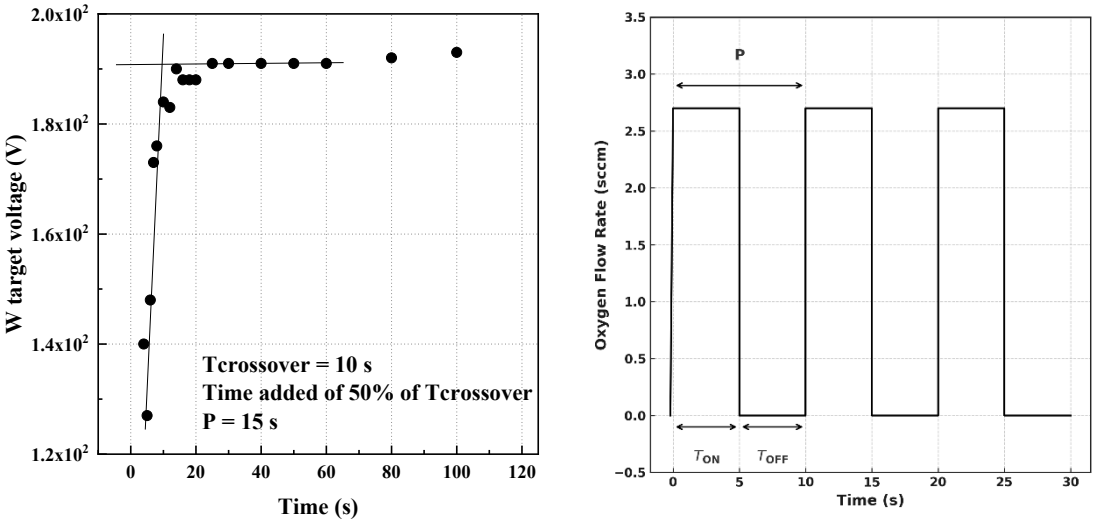

(a) **(b)**

Figure 9 – (a) Evolution of target voltage during the initial seconds of oxygen exposure, indicating the system's crossover time (Tcrossover) used to define the pulse period. (b) An example of the pulsed oxygen flow rate vs. time.

3.3.3 Deposition Time

To determine the optimal deposition time for obtaining thin films with a thickness of approximately 500 nm, preliminary depositions were performed using duty cycle values of 60% and 90% of P. These values were selected from a broader experimental set including duty cycles of 60%, 65%, 70%, 75%, 80%, 85%, and 90%. The 60% and 90% duty cycles were chosen for presentation in this dissertation because they represent the extremes of the tested range and showed the most pronounced differences in structural and optical properties, allowing for a clear comparative analysis.

The depositions were carried out under the following parameters: A fixed current of 100 mA, an argon flow of 2.6 sccm, a pumping speed of 13 L/s, and an oxygen flow of 0 to 2.8 sccm. The deposition time was set to 15 minutes for all tests. The resulting film thicknesses were analyzed using mechanical profilometry, and the following results were obtained (**Table 1**):

Table 1 - Thickness and deposition rate of WO_{3-x} thin films deposited using 60% and 90% duty cycles. The values were obtained by mechanical profilometry.

Duty Cycle (% of T)	Thickness (nm)	Deposition Rate (nm/min)
60	686 ± 23	34.3 ±1.2
90	713 ± 20	35.7 ± 1.0

After the initial tests to define the deposition parameters, WO_x thin films were deposited using the same system. During the process, the tungsten target current was kept constant at I_w= 100 mA, while the argon flow rate was maintained at q_{Ar} = 2.6 sccm. A constant pumping speed of S = 13 L/s resulted in an argon partial pressure of p_{Ar}= 2.8×10^{-3} mbar.

The oxygen flow rate was pulsed during the deposition process using the Reactive Gas Pulsing Process (RGPP). A constant pulsing period of P=15 s was employed, with a maximum oxygen flow rate of qO_{2Max}= 2.8 sccm during T_{on}, and a minimum oxygen flow rate of qO_{2Min}= 0 sccm during T_{off}. The duty cycle was varied to investigate its effect on film deposition, and thin films were deposited with values of 60% and 90% of P, yielding seven distinct samples labeled as WO_{3-x}-60 and WO_{3-x}-90.

The substrates used for deposition included glass, silicon (100), and fluorine-doped tin oxide (FTO). Before deposition, the substrates were thoroughly cleaned in an ultrasonic bath using acetone for 10 minutes, followed by ethanol for an additional 10 minutes, to remove surface contaminants and ensure proper adhesion of the films

After deposition, all samples were subjected to thermal treatment to evaluate the influence of annealing conditions on the structural and optical properties of the films. The glass and silicon substrates were physically divided into two halves: one-half of each sample was annealed at 450 °C for 2 hours in an ambient atmosphere (air), and the other half in an inert argon atmosphere, both with a heating rate of 5 °C/min. As the FTO substrates could not be physically sectioned, new films were deposited under identical conditions to serve as counterparts for the respective thermal treatments.

3.4 Synthesis of g-C_3N_4

To produce graphitic carbon nitride (g-C_3N_4), 1 g of melamine (Sigma-Aldrich, 99%) was placed in a crucible and wrapped in aluminum foil to minimize material loss during the thermopolymerization process. The melamine was then heated at different temperatures—400 °C, 450 °C, 500 °C, and 550 °C—for 4 hours, with a heating rate of 5 °C per minute. The resulting samples were labeled M40, M45, M50, and M55, respectively. **Figure 10** illustrates the sample preparation procedure.

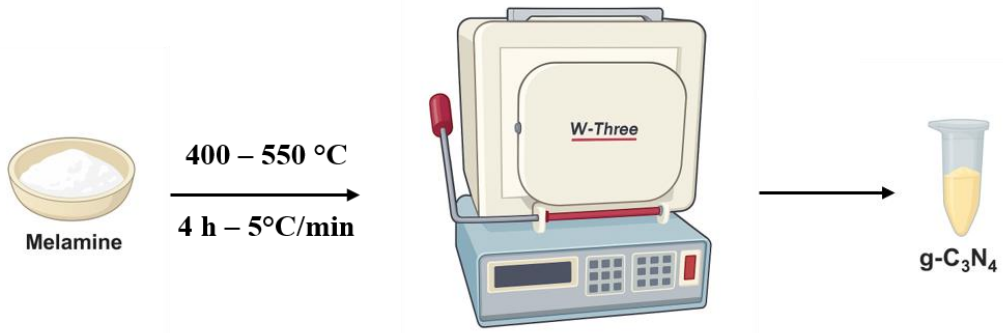

Figure 10 - Schematic representation of the g-C_3N_4 preparation process.

3.5 Characterization techniques

3.5.1 Characterization of Gradient Oxygen Samples

The tungsten oxide thin films deposited with an oxygen gradient were characterized through a comprehensive set of techniques to evaluate their structural, optical, and surface properties, thereby supporting the photoelectrochemical performance analysis.

X-ray diffraction (XRD) analyses were performed using a PANalytical Empyrean diffractometer operating at 40 kV and 40 mA, equipped with a Cu Kα radiation source (λ = 0.15418 nm). The diffraction patterns were collected over a 2θ range from 20° to 90°, with a fixed divergence slit of 1/2°, a 10 mm mask, and a step size of 0.013° with a counting time of 0.013 s per step. Phase identification was performed through Le Bail refinement [70,71] using the HighScore Plus software (Malvern PANalytical) [70], allowing for the accurate fitting of the diffraction profiles and confirmation of the crystalline phases present in the samples.

Raman spectroscopy was conducted using a Horiba Evolution system with a 532 nm laser wavelength. A 600 mm/gr diffraction grating and a 100x lens were employed for focusing. The acquisition time was set to 45 seconds with three accumulations, and a 25% filter was applied. The spectral range measured was from 100 to 1200 cm^{-1}.

Optical transmittance measurements were performed using a UV-Vis Evolution 220 spectrometer (Thermo Scientific), which covers a wavelength range from 190 nm to 1100 nm. A Ramé-Hard Model 500 goniometer was used for contact angle measurements, with deionized water and diiodomethane as the test liquids. Film thickness and surface roughness were

measured using a KLA Tencor P7 profilometer. The morphology of the films was examined using a Tescan Vega 3 scanning electron microscope (SEM) operated at 5 kV.

3.5.2 Characterization of RGPP Samples

The tungsten oxide films synthesized via the Reactive Gas Pulsing Process (RGPP) were characterized using advanced structural, morphological, and spectroscopic techniques. All characterizations were conducted at the MIMENTO technology center in France. Surface morphology was examined using an Apreo Slow-vacuum scanning electron microscope (ThermoFisher), operated in immersion mode with secondary electron detectors (T2/T3). The system was configured with an accelerating voltage of 2.00 kV, a beam current of 25 or 50 pA, and a working distance of 5 mm. Grazing incidence XRD (GIXRD) patterns were recorded using a Malvern Panalytical Aeris diffractometer with Cu Kα radiation (λ = 1.5418 Å), operating at 30 kV and 10 mA, with a fixed incidence angle of 0.8° and a 2θ scan range from 20° to 90°. Optical properties were assessed through transmittance spectra measured with a Lambda 900 UV–Vis spectrophotometer (PerkinElmer), operating in the 200–1100 nm range with a scan speed of 1 nm/s. Surface chemical composition and elemental states were investigated by X-ray photoelectron spectroscopy (XPS), employing Al Kα radiation (1486.6 eV), with a spot size of 200 µm, power of 50 W, and voltage of 15 kV. Survey and high-resolution spectra were collected using pass energies of 280 eV and 55 eV, respectively. Pass energy = 280 eV/55 eV pour spectres/fenêtres

3.5.3 Characterization of g-C_3N_4 Powder

The g-C_3N_4 powder obtained via thermal polycondensation was subjected to a set of morphological, structural, and spectroscopic characterizations to elucidate its physicochemical features. Morphology was examined using a Tescan Mira 3 field-emission scanning electron microscope (FE-SEM), operated with a beam energy of 10 eV, using the secondary electron detection mode. Elemental composition was evaluated through energy-dispersive X-ray spectroscopy (EDX) using an Oxford EDX system coupled to a Tescan Vega 3 SEM. Functional groups and bonding environments were investigated by Fourier-transform infrared spectroscopy (FTIR) using a PerkinElmer spectrometer in UATR mode, acquiring 32 scans over the spectral range of 4000–400 cm^{-1}. XRD measurements were conducted on a PANalytical Empyrean diffractometer equipped with a Cu Kα source (λ = 0.1542 nm), operating in θ–2θ mode with sample rotation at 16 rpm. Complementary Raman analysis was

carried out using a HORIBA LabRAM Odyssey system, equipped with a 785 nm laser, a 50× objective lens, and a 300 gr/mm diffraction grating.

3.6 Photoelectrochemistry setup and conditions

Photoelectrochemical (PEC) measurements were performed using a Metrohm AUTOLAB PGSTAT 302N potentiostat equipped with a frequency response analysis (FRA) module (**Figure 11**). A conventional three-electrode configuration was utilized, consisting of an Ag/AgCl (saturated KCl) reference electrode, a platinum wire as the counter electrode, and the WO_{3-x}-based films (exposed area: 0.9 cm^2) as the working electrode. The experiments were conducted using a 0.5 M Na_2SO_4 cell in a quartz-window PEC aqueous electrolyte. Before each measurement, the electrolyte was freshly replaced for each sample.

Electrochemical impedance spectroscopy (EIS) was performed at open circuit potential (OCP) and under polarization at 0.36 V vs. Ag/AgCl, a potential determined from photocurrent density measurements under illumination. The measurements were conducted before and after cyclic voltammetry to assess possible changes in interfacial properties. EIS spectra were recorded over a frequency range from 10^5 Hz to 0.1 Hz, using a sinusoidal perturbation of 0.1 Vrms.

Mott–Schottky plots were acquired at a fixed frequency of 1000 Hz to estimate flat-band potential and donor density. The measurements were performed under dark conditions.

Cyclic voltammetry (CV) was performed in the dark and under illumination, within a potential window ranging from –0.4 to +1.0 V vs. Ag/AgCl, using a scan rate of 25 $mV \cdot s^{-1}$. Illumination was provided by a solar simulator (ABET Technologies, model 10500), equipped with a 150 W DC xenon lamp and an AM 1.5G filter. The simulator was positioned at a fixed distance of 15 cm from the PEC cell. The same simulator was utilized to determine the potential corresponding to maximum photoresponse, which guided the choice of polarization potential in the EIS measurements.

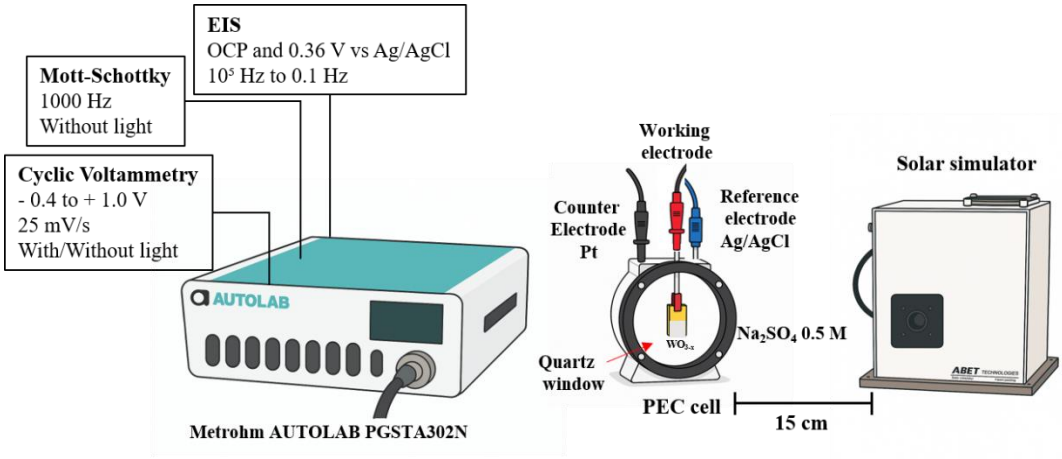

Figure 11 - Schematic of the photoelectrochemical (PEC) setup employed in this study.

4 RESULTS AND DISCUSSION

4.1 WO_{3-x} thin films by oxygen gradient

4.1.1 Structure, morphology, and composition

The bias voltage (Vb) was monitored in real time throughout the deposition to elucidate how the programmed O_2 flow ramps influence plasma dynamics and film growth conditions. **Figure 12(a)** shows the synchronous traces of Vb and oxygen flow rate (ΦO_2) for each experiment. During the argon pre-sputtering interval (−5 to 0 min), Vb remained below 450 V, a level typical of the metallic sputtering mode for tungsten [72]. Immediately after O_2 injection (t = 0 min), Vb rose sharply as the target surface oxidized; once the voltage reached approximately 510 V, the discharge stabilized in the compound regime, in agreement with the threshold reported for comparable W–O systems [72]. Films deposited under slower oxygen ramp conditions (WO_{3-x}-2 and WO_{3-x}-4) took several minutes to reach this plateau, evidencing slower target poisoning. In contrast, higher initial O_2 flows (WO_{3-x}-6, -8, and -10) quickly attained the steady-state voltage, indicating a rapid transition to a fully oxidized target and a stable reactive plasma.

Figure 12(b) confirms that the observed variation in bias voltage correlates with the oxygen flow rate applied during deposition. The linear increase in ΦO_2 for each condition illustrates the programmed ramp profiles used to control the oxidation dynamics of the growing films.

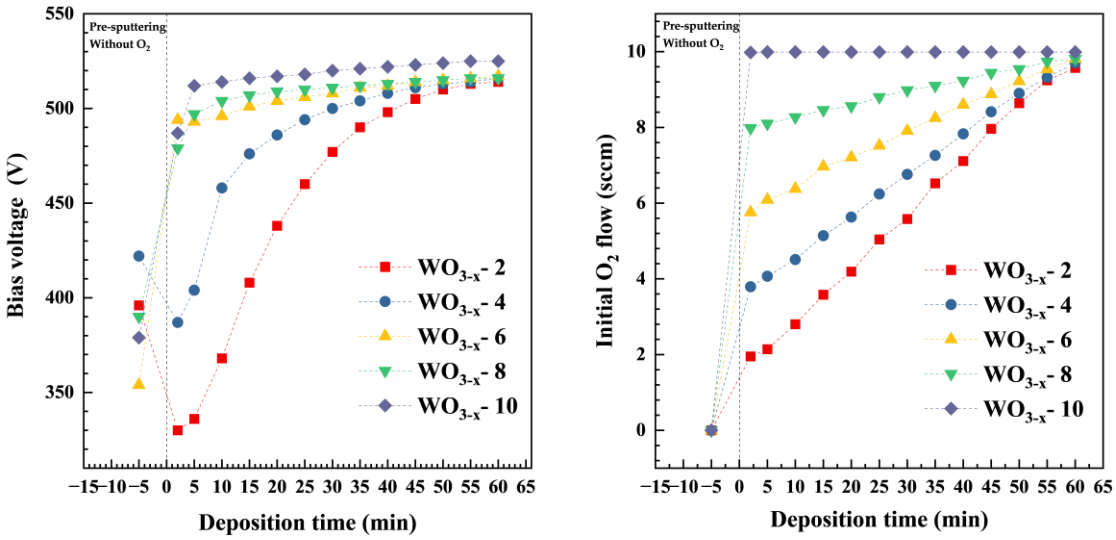

Figure 12 - (a) Evolution of bias voltage as a function of deposition time for WO_{3-x} films synthesized under different oxygen ramp conditions. The pre-sputtering step (–5 to 0 min) was performed under a pure argon atmosphere to stabilize the plasma before oxygen introduction. (b) Oxygen flow profiles (ΦO_2) were programmed during the deposition of each sample.

The thickness and surface morphology of the WO_{3-x} thin films were first evaluated using 2D profilometry. The measurements revealed an inverse trend between film thickness and the oxygen flow applied during deposition. The WO_{3-x}–2 sample (2 sccm) presented the highest average thickness (1157 ± 50 nm), while WO_{3-x}–10 (10 sccm) showed the lowest value (536 ± 40 nm), as illustrated in **Figure 13(a)** and **Table 2**. This gradual reduction is associated with the progressive transition to the compound regime during reactive sputtering, in which poisoning of the target by oxygen reduces the deposition rate by forming an insulating oxide layer on the cathode. Similar results were reported by Olejníček et al. (2022), who demonstrated the decrease in thickness with increasing oxygen flow due to sputtering suppression in highly oxidizing regimes [73].

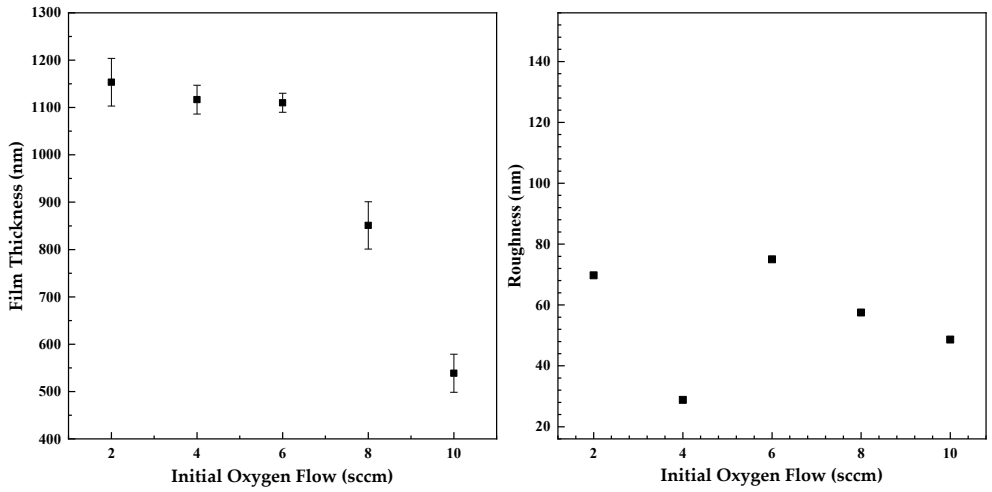

(**a**) (**b**)

Figure 13 - (a) Film thickness as a function of initial oxygen flow rate. Error bars show the standard deviation from multiple profilometry scans. (b) Surface roughness variation with initial oxygen flow rate.

Table 2 - Average film thickness and surface-roughness of WO_{3-x} thin films.

Sample	Thickness (nm)	Roughness (nm)
WO_{3-x} - 2	1157 ± 50	69.7
WO_{3-x} - 4	1117 ± 30	28.8
WO_{3-x} - 6	1112 ± 20	75.0
WO_{3-x} - 8	862 ± 50	57.5
WO_{3-x} - 10	536 ± 40	48.6

In parallel, the roughness values obtained from 3D profilometry (**Figure 14**) revealed a non-monotonic behavior. The highest roughness was observed for WO_{3-x}–6 (75 nm), while WO_{3-x}–4 exhibited the smoothest surface (28.8 nm), suggesting that intermediate oxygen flow ramps favor surface instabilities or heterogeneous granular growth. In contrast, under extreme flows, roughness is governed respectively by high growth rates and disordered nucleation (low flow), or by reduced surface mobility and resputtering (high flow), in agreement with discussions by Hrubantová et al. (2022) on complex oxide films grown by DC sputtering [74].

From these observations, it becomes evident that oxygen flow control is a critical variable not only for modulating film thickness but also for engineering surface roughness, a key factor in the mechanical and functional robustness of the electrodes. Surfaces with moderate roughness and hierarchical architecture, as observed in WO_{3-x}–6 and WO_{3-x}–8, promote greater

adhesion to the substrate and lower mechanical fragility, attributes also discussed by Singh et al. (2024) for films applied in optoelectronic devices [75]

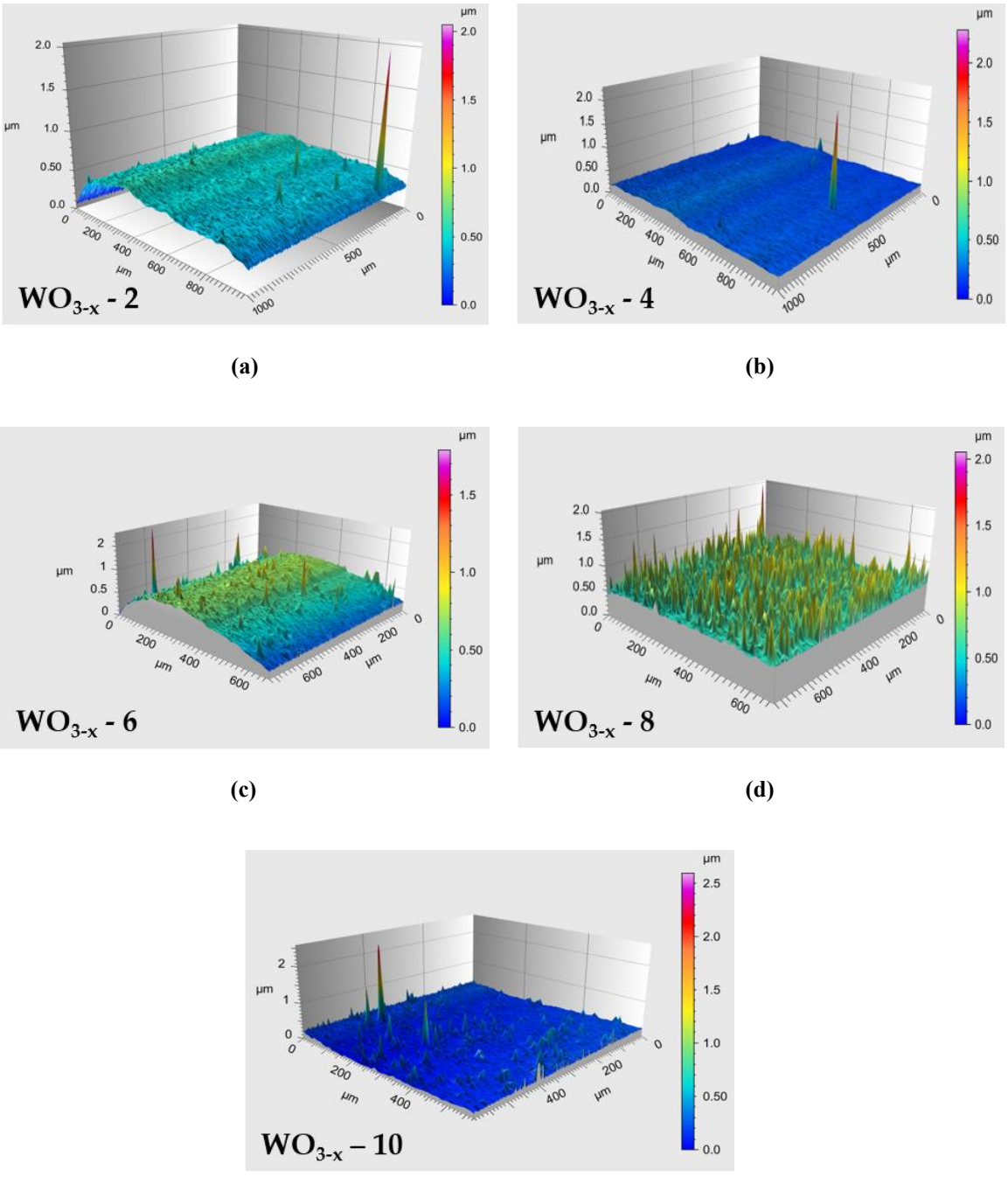

Figure 14 - Three-dimensional surface topography of WO_{3-x} thin films synthesized under different O_2 ramps: (a) WO_{3-x}-2, (b) WO_{3-x}-4, (c) WO_{3-x}-6, (d) WO_{3-x}-8 and (e) WO_{3-x}-10. Colour scales represent height variations relative to the mean plane.

These morphological observations are further supported by the cross-sectional SEM images presented in **Figure 15** which also confirm the thickness trends observed in

profilometry, with a margin of deviations within ± 4 %. Films deposited with the lowest initial oxygen flows (WO_{3-x}–2 and WO_{3-x}–4) exhibit a clearly defined bilayer architecture consisting of a dense metallic sublayer (183 nm and 115 nm, respectively) overlain by a significantly thicker oxidized layer. This stratification results from the initial oxygen-deficient plasma conditions that favor metallic tungsten (W^0) growth. As the oxygen flow increases and the cathode bias gradually approaches ~510 V, the system transitions into the compound sputtering regime, enabling the formation of a WO_{3-x} layer atop the metallic base.

The thickness of the metallic sublayer in WO_{3-x}–2 exceeds that of WO_{3-x}–4, reflecting the longer duration during which the target remained in the metallic regime. This delay in reaching the compound mode is linked to the slower ramping of oxygen, allowing more W^0 to accumulate before full target poisoning occurred. Conversely, films grown under higher oxygen ramp rates (WO_{3-x}–6, -8, and -10) reach the compound regime within the first minute of deposition, leading to a single-phase, compositionally homogeneous structure across the entire thickness. This dynamic transition underscores the correlation between the applied bias voltage, structural morphology, and film architecture, which has been reported in the literature for sputtered transition metal oxides under similar plasma conditions [73,75,76].

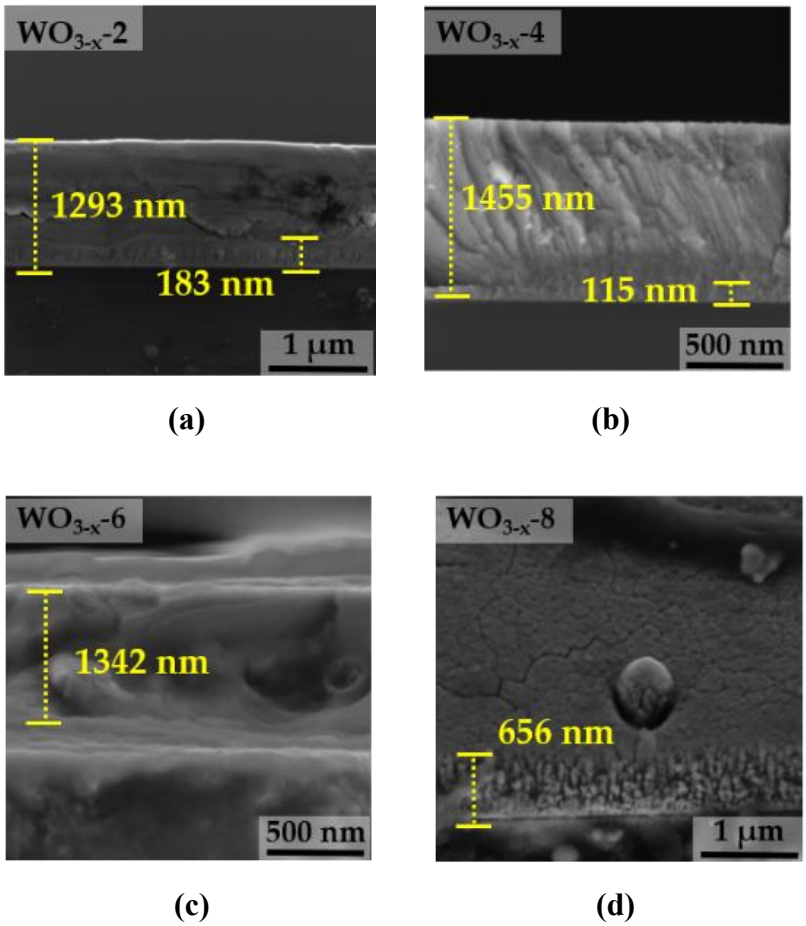

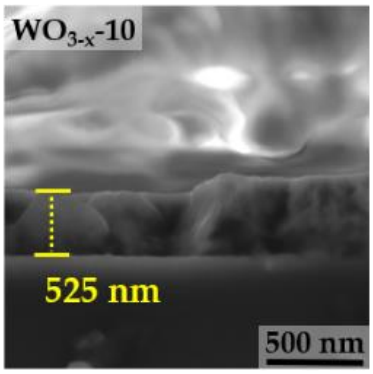

(e)

Figure 15 - Cross-sectional SEM images and corresponding thickness measurements of WO_{3-x} films deposited under progressively higher initial oxygen-flow ramps: (a) WO_{3-x}-2, (b) WO_{3-x}-4, (c) WO_{3-x}-6, (d) WO_{3-x}-8, and (e) WO_{3-x}-10.

Static contact-angle measurements with polar (water) and apolar (diiodomethane) liquids, analysed through the geometric model for surface-energy calculations, provided information on the surface wettability of WO_{3-x} thin films; the results are presented in **Table 3** and **Figure 16**. All samples exhibited hydrophilic behaviour, as confirmed by water contact angles below 40°, in agreement with previous studies [77,78]. Sample WO_{3-x}–8 showed the lowest angle (15.3°) and the highest total surface free energy (76.45 $mJ \cdot m^{-2}$); similarly high values were recorded for WO_{3-x}–6 (74.32 $mJ \cdot m^{-2}$) and WO_{3-x}–4 (75.64 $mJ \cdot m^{-2}$). These more energetic surfaces, enriched in polar components, favour both the adsorption of reactive species and the separation and extraction of charge carriers during photoelectrochemical operation. This behavior is further reinforced by the combination of moderate surface roughness and enhanced surface polarity, particularly in samples obtained under intermediate oxygen flows, which promote hierarchical morphologies beneficial to wettability and catalytic efficiency. Such correlations between microstructure, roughness, and wettability have also been reported in the literature for nanoporous WO_3 films, where surface architecture plays a decisive role in interfacial charge transfer processes [44]. In contrast, WO_{3-x}–10 exhibited the largest contact angle (39.7°) and the lowest total surface free energy (65.27 $mJ \cdot m^{-2}$), whereas WO_{3-x}–2 displayed 34.9° and 69.47 $mJ \cdot m^{-2}$, respectively, indicating relatively more apolar surfaces compared with the films obtained under intermediate oxygen ramps.

Table 3 - Static contact angles and surface-free-energy components of WO_{3-x} films

Sample	Water (Angle)	Diiodomethane (Angle)	Polar Component (mJ/m^2)	Dispersive Component (mJ/m^2)	Surface Free Energy (mJ/m^2)
WO_{3-x} - 2	34.95 ± 0.01	25.21 ± 0.04	23.40 ± 0.01	46.08 ± 0.01	69.47 ± 0.01
WO_{3-x} - 4	18.76 ± 0.01	28.19 ± 0.01	30.69 ± 0.01	44.95 ± 0.01	75.64 ± 0.01
WO_{3-x} - 6	21.31 ± 0.01	30.67 ± 0.01	30.38 ± 0.01	43.94 ± 0.01	74.32 ± 0.01
WO_{3-x} - 8	15.33 ± 0.01	29.26 ± 0.01	31.92 ± 0.01	44.53 ± 0.01	76.45± 0.01
WO_{3-x} - 10	39.71 ± 0.01	33.33 ± 0.01	22.48 ± 0.01	42.79 ± 0.01	65.27 ± 0.01

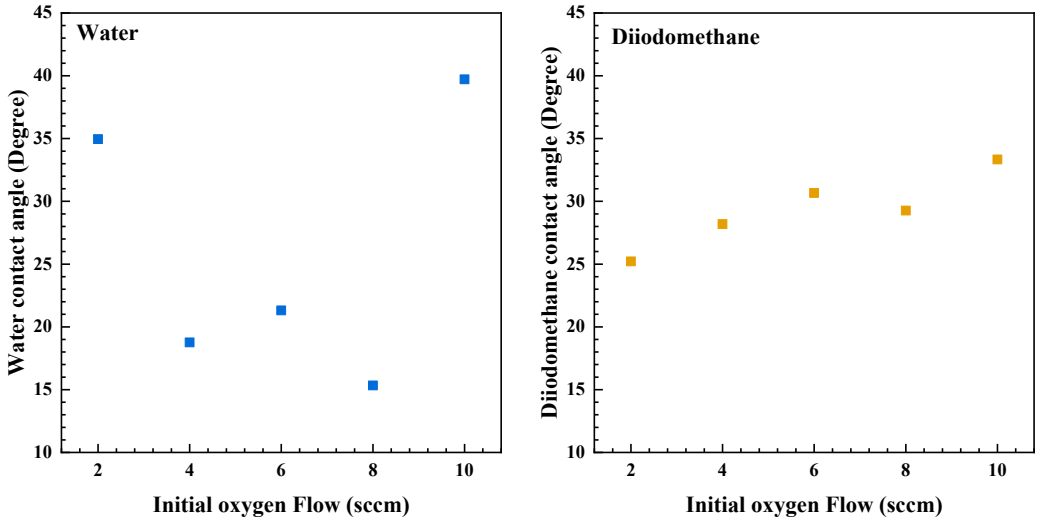

(a) **(b)**

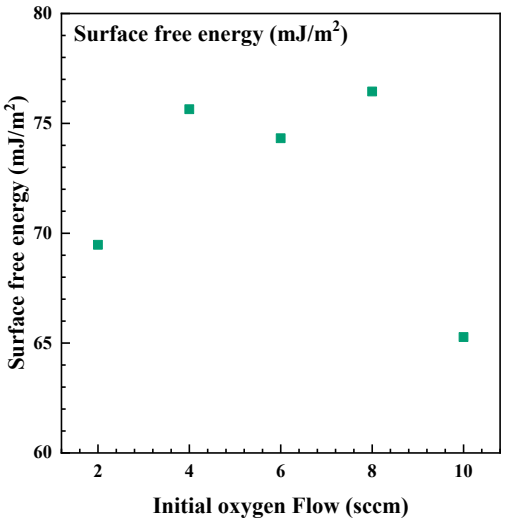

(c)

Figure 16 - Influence of the initial oxygen flow on (a) the contact angles of water (b) the contact angles of diiodomethane and (c) the total surface free energy of WO_{3-x} films.

In summary, the combined analyses of deposition parameters, film thickness, surface roughness, microstructure, and wettability provide a comprehensive understanding of how reactive sputtering conditions influence the physical characteristics of WO_{3-x} films. These insights lay the groundwork for the following discussion on the crystallographic structure and vibrational behavior of the samples.

4.1.2 Crystallographic and Vibrational Analysis

The X-ray diffraction (XRD) analysis was performed to identify the crystalline phases present in the WO_{3-x} films. This technique is based on the diffraction of monochromatic X-rays by the periodic arrangement of atoms in a crystalline solid, enabling the determination of phase composition, crystallite size, and structural strain. The patterns were refined using the Le Bail method [70,71], a whole-pattern fitting procedure that allows extraction of unit cell parameters without requiring knowledge of atomic positions. The refinements were implemented in the HighScore Plus software package [79], which enables reliable deconvolution of overlapping peaks and precise determination of lattice parameters.

The diffraction patterns (**Figure 17**) show that all samples exhibit exclusively the monoclinic γ-WO_3 phase ($P2_1/n$, space group 14; ICSD PDF 01-089-4476). The only additional peaks detected originate from the fluorine-doped tin oxide (FTO) substrate and are clearly indicated in the diffractograms. No reflections from metallic tungsten or sub-stoichiometric tungsten oxides were observed, suggesting that even the film deposited under the lowest initial oxygen flow conditions is predominantly oxidized. This behavior is consistent with studies reported in the literature, which indicate that the monoclinic phase remains stable up to 400 °C in WO_3 nanoparticles, with phase transition to β-WO_3 only occurring at 500 °C [21,74].

Refinement results are summarized in **Table 4**. Among the films, WO_{3-x}–2 displays the largest unit cell volume, which progressively contracts with increasing oxygen flow, stabilizing near 424.5 Å³ for flows above 4 sccm. This contraction is attributed to the reduced concentration of oxygen vacancies as more oxygen is incorporated into the lattice, leading to restoration of W–O bonds and shortening of lattice parameters [74]. Similar structural relaxation with decreasing vacancy concentration has also been reported for WO_{3-x} films deposited via sputtering under different oxygen regimes [74].

Furthermore, the microstrain (ε), which reflects lattice distortions due to defects or stress, decreases from 0.60% in WO_{3-x}–2 to 0.43% in WO_{3-x}–8, corroborating the progressive lattice relaxation as the film approaches stoichiometry. A slight increase in ε to 0.46% for

WO_{3-x}–10 may be related to residual stresses induced by lower deposition rates and enhanced ion bombardment in highly oxidizing plasma environments, as also noted by Hrubantova et al. (2022) in similar sputtering conditions [74].

The average crystallite size also follows a trend consistent with reduced disorder and improved crystalline quality under increased oxygen flow. It increases from 31 nm in WO_{3-x}–2 to a maximum of 43.7 nm in WO_{3-x}–8. This observation aligns with previous findings where enhanced oxidizing atmospheres during sputtering promoted grain growth and crystallinity [74].

These structural insights reinforce the direct relationship between the reactive sputtering atmosphere, defect concentration, and resulting crystalline quality of WO_{3-x} films, offering a solid foundation for interpreting their functional behavior in subsequent photoelectrochemical and vibrational analyses.

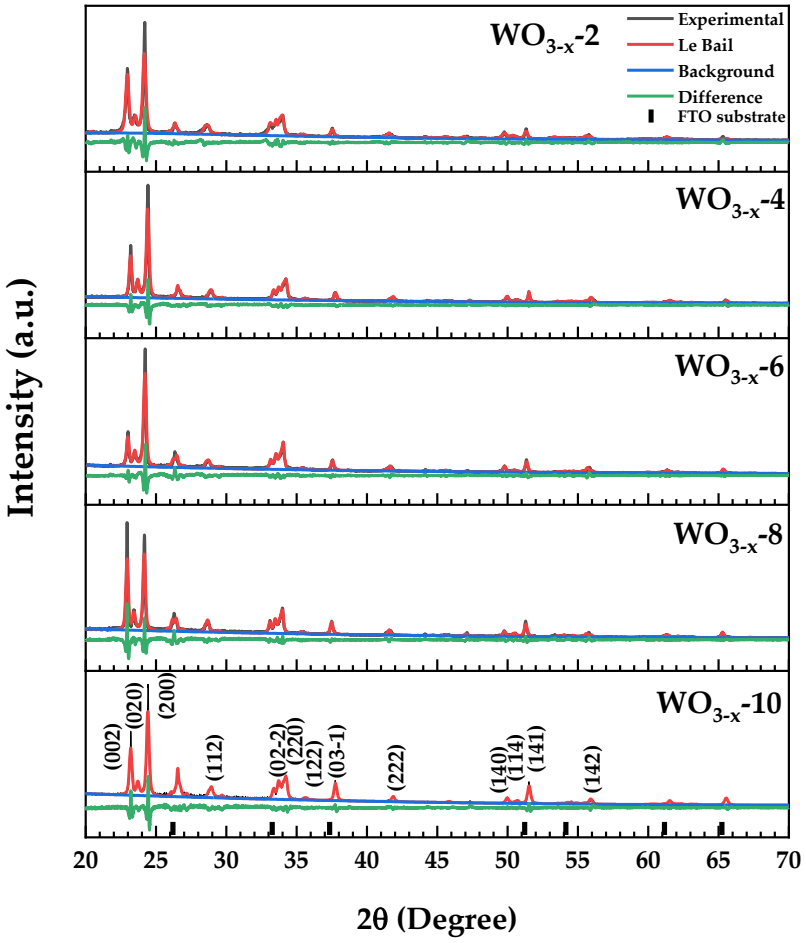

Figure 17 - X-ray diffraction patterns of WO_{3-x} films. For each sample, the experimental profile (black) is overlaid with the Le Bail refinement (red), the fitted background (blue), and the difference curve (green). Reflection indices correspond to monoclinic γ-WO_3 (ICDD PDF 01-089-4476); tick marks at the bottom indicate peaks from the FTO substrate.

Table 4 - Refined structural parameters of monoclinic γ-WO_3 thin films. Listed are the lattice constants a, b, c, mono-clinic angle β, unit-cell volume, microstrain, volume-averaged, crystallite size, and the goodness-of-fit indicators χ^2, R_{exp} and R_{wp} obtained from Le Bail refinements of the X-ray diffraction data.

Sample	α (Å)	b (Å)	c (Å)	β (deg)	Unit cell vol (Å^3)	Microstrain (%)	Crystallite size (nm)	X^2	R_{exp}	R_{wp}
WO_{3-x} - 2	7.3570(1)	7.5520(7)	7.7390(1)	90.648(9)	429.9539	0.600	31.45±0.51	4.255	5.5128	11.3729
WO_{3-x} - 4	7.3130(6)	7.5276(5)	7.6926(6)	90.513(6)	423.4560	0.480	38.16±0.025	3.001	5.7150	9.9112
WO_{3-x} - 6	7.3190(3)	7.5367(3)	7.6959(4)	90.510(6)	424.5050	0.476	39.61±0.023	3.213	5.7819	10.3656
WO_{3-x} - 8	7.3205(9)	7.5389(6)	7.700(1)	90.505(7)	424.9583	0.433	43.65±0.10	4.140	5.8721	11.9481
WO_{3-x} - 10	7.3173(7)	7.533(4)	7.6984(5)	90.547(7)	424.3309	0.461	40.49±0.046	2.446	6.2945	9.8451

As a complementary technique to X-ray diffraction, Raman spectroscopy was employed to investigate the vibrational modes of the WO_{3-x} films and to support the identification of the crystalline phases. The spectra obtained (**Figure 18**) exhibit the typical vibrational fingerprint of monoclinic γ-WO_3, with no evidence of secondary or amorphous phases [80].

Raman spectroscopy revealed the main vibrational modes of the monoclinic γ-WO_3 phase at approximately 132, 182, 271, 325, 714, and 806 cm^{-1}. These bands are attributed to lattice vibrations (≤ 200 cm^{-1}), O–W–O bending (~270–330 cm^{-1}), and W–O stretching modes (~712–810 cm^{-1}), consistent with the monoclinic γ-phase of WO_3. The assignments are corroborated by previous studies, which associate the bands at ~270 and 326 cm^{-1} with O–W–O bending modes and the bands at ~712 and 806 cm^{-1} with asymmetric and terminal W=O stretching modes, respectively [73,74,81].

The broadening of the Raman peaks in the lower frequency region for WO_x-2 and WO_x-4 suggests increased structural disorder and a higher concentration of oxygen vacancies. The progressive blue-shift of the 714 cm^{-1} band and the intensity rise of the 806 cm^{-1} band with increasing O_2 flow indicate a local oxidation of tungsten sites, consistent with previous observations [81,82].

The persistence of all major vibrational modes across the entire series of samples, regardless of the oxygen flow conditions, reinforces the structural findings from XRD and confirms the dominance of the monoclinic γ-WO_3 phase throughout the set.

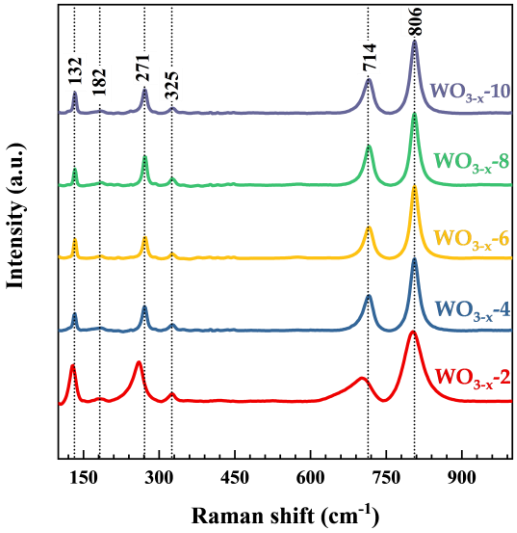

Figure 18 - Raman spectra (λ exc = 532 nm) of WO_{3-x} films. The dashed lines mark the main vibra-tional modes of monoclinic γ-WO_3.

4.1.3 Optical Properties

UV-Vis transmittance spectroscopy is a widely employed technique for the optical characterization of semiconductor thin films, as it enables the evaluation of electromagnetic radiation absorption as a function of the energy of incident photons. Through analysis of the transmittance spectra, it is possible to estimate fundamental properties such as the optical bandgap energy (Eg), the presence of intermediate states, and the structural quality of the material. Transmittance is sensitive to variations in thickness, morphology, and stoichiometry, making it an essential tool for the assessment of materials intended for optoelectronic devices, solar cells, and photoelectrodes.

In this study, the spectra obtained for WO_{3-x} thin films revealed typical behavior of semiconductors with an indirect bandgap, exhibiting significant transmittance in the visible range and an absorption edge that shifts toward longer wavelengths as the oxygen flow during deposition decreases.

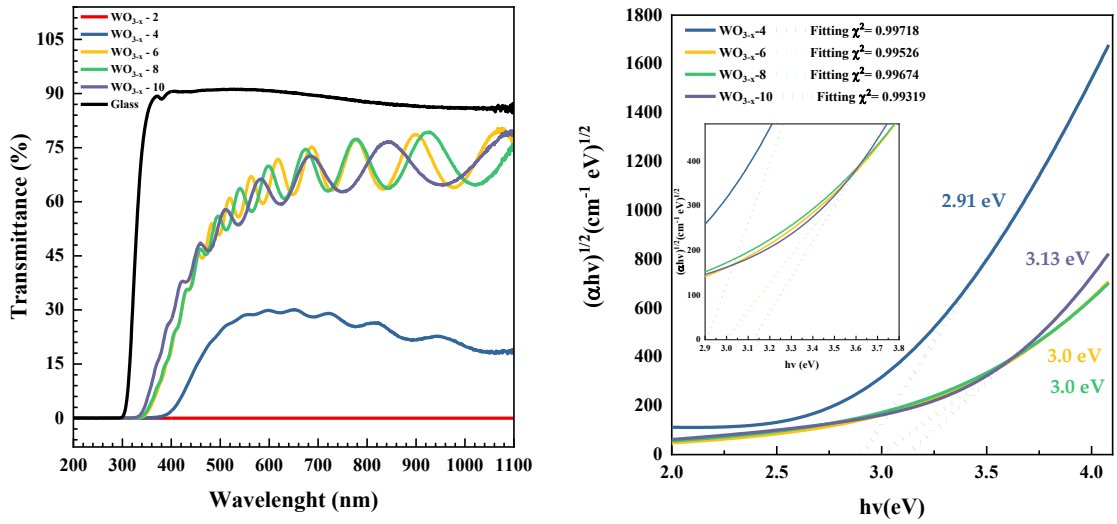

(**a**) (**b**)

Figure 19 - (a) UV–Vis–NIR transmittance spectra (200–1100 nm) of WO_{3-x} films grown with initial oxygen flows of 2, 4, 6, 8 and 10 sccm. (b) Tauc plots for the translucent samples; dotted lines are the linear fits used to determine the indirect optical band gap.

The transmittance spectra clearly demonstrate a strong influence of the initial O_2 flow on the optical transparency of the films (**Figure 19(a)**). The sample WO_{3-x}-2 is practically opaque throughout the entire spectral range, due to its high thickness (~ 1.3 μm) and dark coloration. For oxygen flows between 4 and 10 sccm, the visible transmittance reaches 70–75%, displaying well-defined interference fringes that confirm good thickness uniformity and low extinction coefficients.

The optical bandgap energy (Eg) was determined using the Tauc method, which is widely used for the analysis of semiconductor materials [83]. This method relates the absorption coefficient (α) to the photon energy (hv) through the following **Eq.2**:

$$(\alpha h\nu)^{1/n} = A(h\nu - E_g), \qquad \textbf{Eq.2}$$

where A is a constant, Eg represents the bandgap energy, and the exponent n depends on the type of electronic transition involved [83]. For indirect transitions, as in the case of WO_{3-x}, the exponent n is equal to 0.5. This selection is supported by the structural characteristics of tungsten oxide and is confirmed in the recent literature [44,73,76,84]. Thus, the plot was constructed by plotting $(\alpha h\nu)^{0.5}$ versus hv, and the Eg value was obtained by extrapolating the linear portion of the curve to the energy axis.

The analysis (**Figure 19(b)**) indicates that the indirect optical bandgap increases with stoichiometry: from 2.91 eV in WO_{3-x}-4 to 3.13 eV in WO_{3-x}-10, passing through 3.00 eV in WO_{3-x}-6 and WO_{3-x}-8. One hypothesis is that this bandgap widening is associated with a gradual decrease in the concentration of oxygen vacancies and W^{5+} cations, whose presence in WO_{3-x}-4 reduces the band separation by introducing shallow donor levels. As the target becomes rapidly poisoned (flows ≥ 6 sccm), the W^{6+} content increases and donor states are suppressed, shifting the absorption edge toward higher energies.

The coincidence between the gap values (~ 3.0–3.1 eV) and the region of maximum surface free energy (WO_{3-x}-6 and WO_{3-x}-8) suggests that an intermediate concentration of vacancies simultaneously optimizes transparency, surface activity, and photoelectrochemical performance. WO_{3-x}-10, although more transparent and exhibiting a wider bandgap, presents lower surface polarity and therefore a reduced electrochemically active area.

Previous studies support the interpretation of these results. CHANANONNAWATHORN et al. (2012) demonstrated that reducing the oxygen flow during the sputtering deposition of WO_3 leads to a decrease in the bandgap energy, due to the increased concentration of vacancies and greater structural disorder [44]. HRUBANOVA et al. (2022) reported variations in Eg values ranging from 2.6 to 3.1 eV, depending on the stoichiometry and thermal treatment applied to the films [76].

Therefore, the transmittance results demonstrate that the control of oxygen flow during film deposition is a crucial factor for engineering the band structure of WO_{3-x} films, allowing the tuning of their optical properties as desired, in agreement with findings reported in the literature.

4.1.4 Photoelectrochemistry Properties

Electrochemical impedance spectroscopy (EIS) is a powerful technique used to probe interfacial charge transfer phenomena and the electrical behavior of electrochemical systems over a range of frequencies. In the context of photoelectrochemical (PEC) water splitting, EIS allows the investigation of key parameters such as solution resistance (R_s), charge transfer resistance (R_1), and diffusion or recombination-related resistance in the bulk or interface (R_p). These parameters, extracted via fitting with equivalent circuits, provide insight into the semiconductor/electrolyte interface dynamics, the effectiveness of charge separation, and the degree of disorder or defectiveness within the electrode material [85].

In this study, EIS measurements were performed under open circuit potential (OCP) and under anodic polarization at +0.36 V vs. Ag/AgCl, both before and after cyclic voltammetry

under simulated solar illumination. The Nyquist plots obtained are presented in **Figure 20**, and the equivalent circuit used for fitting is shown in **Figure 21**. This model comprises two-time constants: one associated with the electrode/electrolyte interface ($R_1||CPE_1$), and another with transport or accumulation within the film ($R_p||CPE_2$).

The fitting parameters are summarized in **Table 5**. The solution resistance R_s remained nearly constant across all samples (15–21 Ω), indicating that the observed impedance differences are primarily attributed to interfacial phenomena. Under OCP conditions, the charge transfer resistance R_1 decreased significantly with increasing O_2 flow, from 25 kΩ in WO_{3-x}-2 to 4.9 kΩ in WO_{3-x}-8, before increasing again in WO_{3-x}-10 (63 kΩ). This behavior is indicative of an optimal concentration of oxygen vacancies and improved surface hydrophilicity at intermediate flows.

A similar trend was observed for R_p, which reached its lowest value in WO_{3-x}-8 (~ 64 kΩ), suggesting enhanced charge mobility within the film, possibly due to better crystallinity and defect distribution. After light exposure, both R_1 and R_p decreased further for all samples, with more pronounced changes in WO_{3-x}-4 and WO_{3-x}-6. These results point to photoinduced passivation of shallow traps associated with sub-stoichiometric defects, which promotes more efficient charge separation and increases the capacitance of the electrical double layer.

Under polarization at +0.36 V, the semicircles shifted to higher frequencies, maintaining the resistance hierarchy. Once again, WO_{3-x}-6 and WO_{3-x}-8 exhibited the lowest R_1 and R_p values, with reductions of approximately 40% after illumination. This suggests that light-induced effects persist under bias and reinforce interfacial charge transfer. Additionally, the increase in the CPE_2 exponent (n_2) for these samples indicates a more homogeneous interface, which is consistent with structural refinement driven by the oxygen gradient.

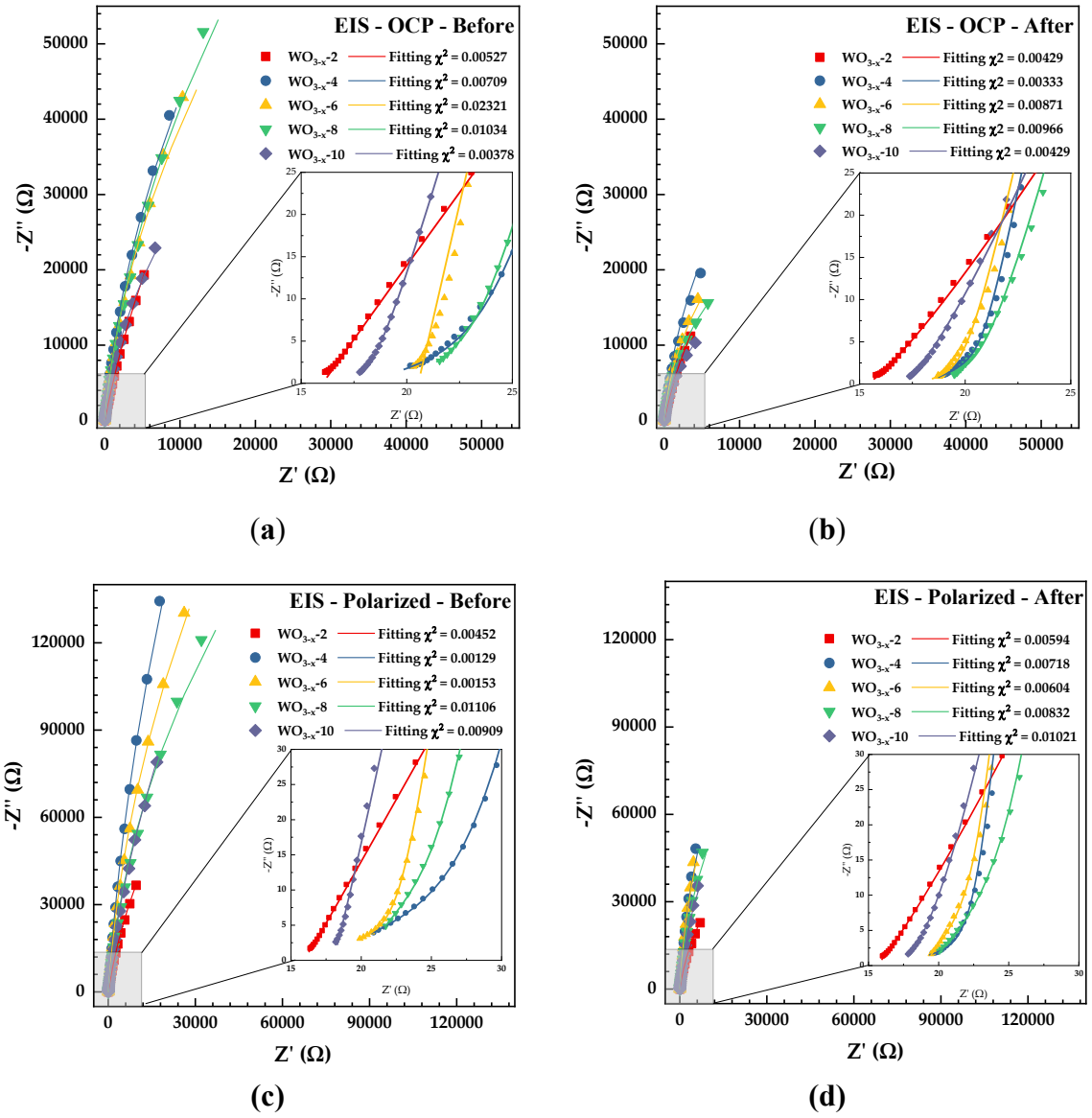

Figure 20 - Nyquist plots obtained from electrochemical impedance spectroscopy (EIS) for the WO_{3-x} electrodes under four experimental conditions: (a) open-circuit potential (OCP) before photoe-lectrochemical testing, (b) OCP after illumination, (c) under anodic polarisation before illumina-tion and (d) under the same polarisation after illumination.

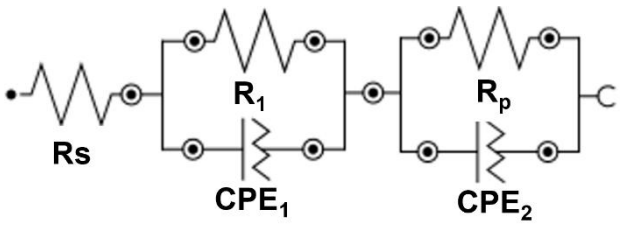

Figure 21 - Equivalent electrical circuit employed to fit the EIS data.

Table 5 - Fitted electrochemical-impedance parameters for WO_{3-x} electrodes under different measurement conditions.

Sample	Condition	Rs (Ω)	R1 (Ω)	Y_{01} (μMho·s^n)	N_1	Rp (Ω)	Y_{02} (μMho·s^n)	N_2
WO_{3-x}-2	OCP Before	16.0	25.3	996.0	0.701	285000	73.7	0.878
	OCP After	15.3	18.7	6060	0.509	112000	124	0.878
	Polarized Before	15.9	66.8	487	0.688	356000	39.3	0.907
	Polarized After	15.6	29.7	1540	0.602	162000	61.0	0.909
WO_{3-x}-4	OCP Before	17.9	8.74	1410	0.472	307000	35.6	0.945
	OCP After	18.2	2.73	493	0.672	147000	74.7	0.951
	Polarized Before	16.7	15.8	352	0.522	189000	11.5	0.957
	Polarized After	17.1	6.35	930	0.483	563000	32.2	0.971
WO_{3-x}-6	OCP Before	20.5	94200	53.3	0.929	475000	81.0	0.967
	OCP After	17.8	2.79	2650	0.504	81700	87.9	0.946
	Polarized Before	16.2	6.89	96.7	0.623	975000	11.4	0.955
	Polarized After	19.0	3.64	279	0.777	546000	35.7	0.97
WO_{3-x}-8	OCP Before	20.0	3.76	276	0.683	318000	27.0	0.935
	OCP After	50.8	4.93	166000	0.00313	64500	86.3	0.939
	Polarized Before	20.2	4.99	49.3	0.834	645000	11.5	0.945
	Polarized After	19.2	6.89	521	0.669	352000	32.5	0.964
WO_{3-x}-10	OCP Before	15.6	3.65	3460	0.384	131000	60.8	0.928
	OCP After	17.1	399000	134	0.943	39000	3630	0.591
	Polarized Before	18.0	30600	73.9	0.857	843000	23.6	0.993
	Polarized After	16.7	297000	42.7	0.956	703000	14800	0.365

Cyclic voltammograms revealed significant differences in the electrochemical behavior of the films as a function of their oxygen content, as shown in **Figure 22** - Cyclic-voltammetry curves of WO_{3-x} electrodes at a scan rate of 25 mV s^{-1}. (a) Responses under dark conditions; (b) photo-assisted responses under AM 1.5G illumination (100 mW cm^{-2}).. Notably, the WO_{3-x}-2 and WO_{3-x}-4 samples exhibited an anodic peak around −0.1 V vs. Ag/AgCl, which was absent in the other samples. This peak, observed exclusively under dark conditions, was attributed to the oxidation of W^{5+} to W^{6+} species, a process favored by the higher density of oxygen vacancies in the films with lower oxygen content [49,85]. The presence of oxygen vacancies tends to stabilize reduced tungsten states (W^{5+}), which, upon oxidation during the forward scan, give rise to a characteristic anodic peak at negative potentials. This behavior is consistent with the

literature, where the $W^{5+} \rightarrow W^{6+}$ oxidation process is reported to be predominant in sub-stoichiometric WO_3 films, particularly in neutral electrolytes that do not promote significant ionic intercalation [85,86].

In contrast, the WO_{3-x}-6, WO_{3-x}-8, and WO_{3-x}-10 samples, which contain higher oxygen concentrations, did not exhibit this anodic peak, indicating that the concentration of W^{5+} species is substantially lower or negligible in these compositions. In these cases, the electrochemical behavior was predominantly capacitive, with more stable and symmetric currents in both branches of the voltammetric curve. Under dark conditions, the current densities ranged from −0.035 to 0.0025 mA·cm^{-2}. Upon light irradiation, all samples exhibited a significant increase in current, with values ranging from −0.07 to 1.3 mA·cm^{-2}. This behavior is characteristic of the photoelectrochemical activation of WO_3 films, whose bandgap enables the generation of electron–hole pairs under illumination. The photocurrent response was particularly pronounced for the WO_{3-x}-8 sample, indicating higher efficiency in photogenerated charge separation and electronic transport [86,87]. Moreover, the absence of the anodic peak at −0.1 V under illumination further supports the hypothesis that this feature is exclusively associated with redox-active tungsten species stabilized under dark conditions.

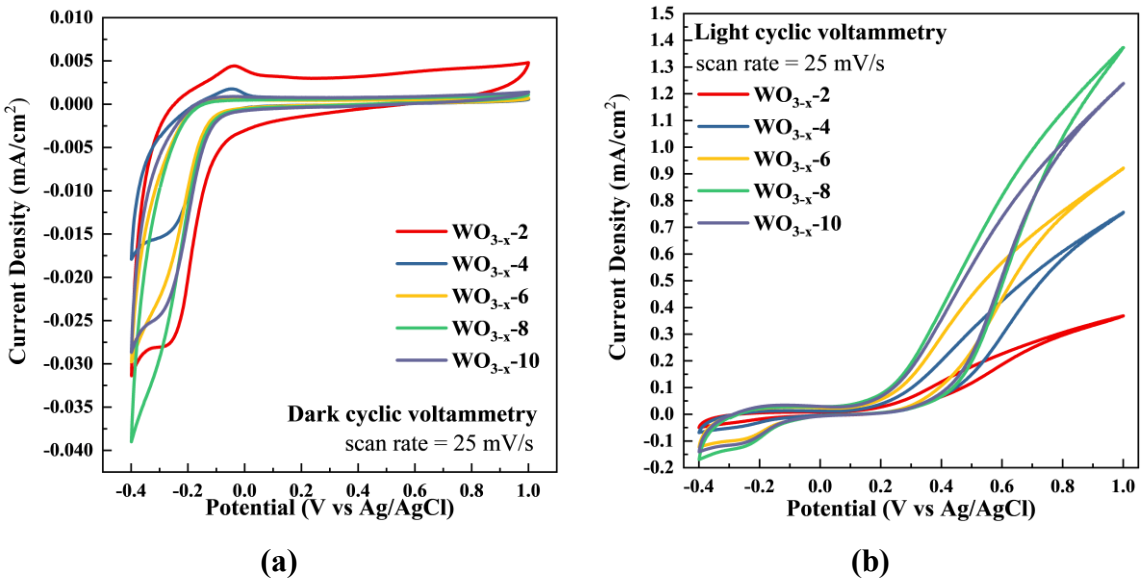

Figure 22 - Cyclic-voltammetry curves of WO_{3-x} electrodes at a scan rate of 25 mV s^{-1}. (a) Responses under dark conditions; (b) photo-assisted responses under AM 1.5G illumination (100 mW cm^{-2}).

The quantitative analysis of the electrochemical properties was performed based on specific capacitance (Cs), specific energy (Es), and specific power (Ps), as shown in **Figure 23** and summarized in **Table 6**.

The specific capacitance values varied among the samples according to the film composition. The WO_{3-x}-8 sample exhibited the highest specific capacitance (0.376 $mF \cdot cm^{-2}$), followed by WO_{3-x}-10 and WO_{3-x}-2. The lowest value was recorded for WO_{3-x}-4 (0.188 $mF \cdot cm^{-2}$), indicating that an increase in oxygen content does not necessarily lead to a proportional increase in capacitance. The WO_{3-x}-8 sample stood out with the highest values across all metrics, suggesting an optimal point in the concentration of oxygen vacancies. This behavior supports the idea that there is an ideal balance between the density of oxygen vacancies and structural integrity to maximize electrochemical performance [42,88].

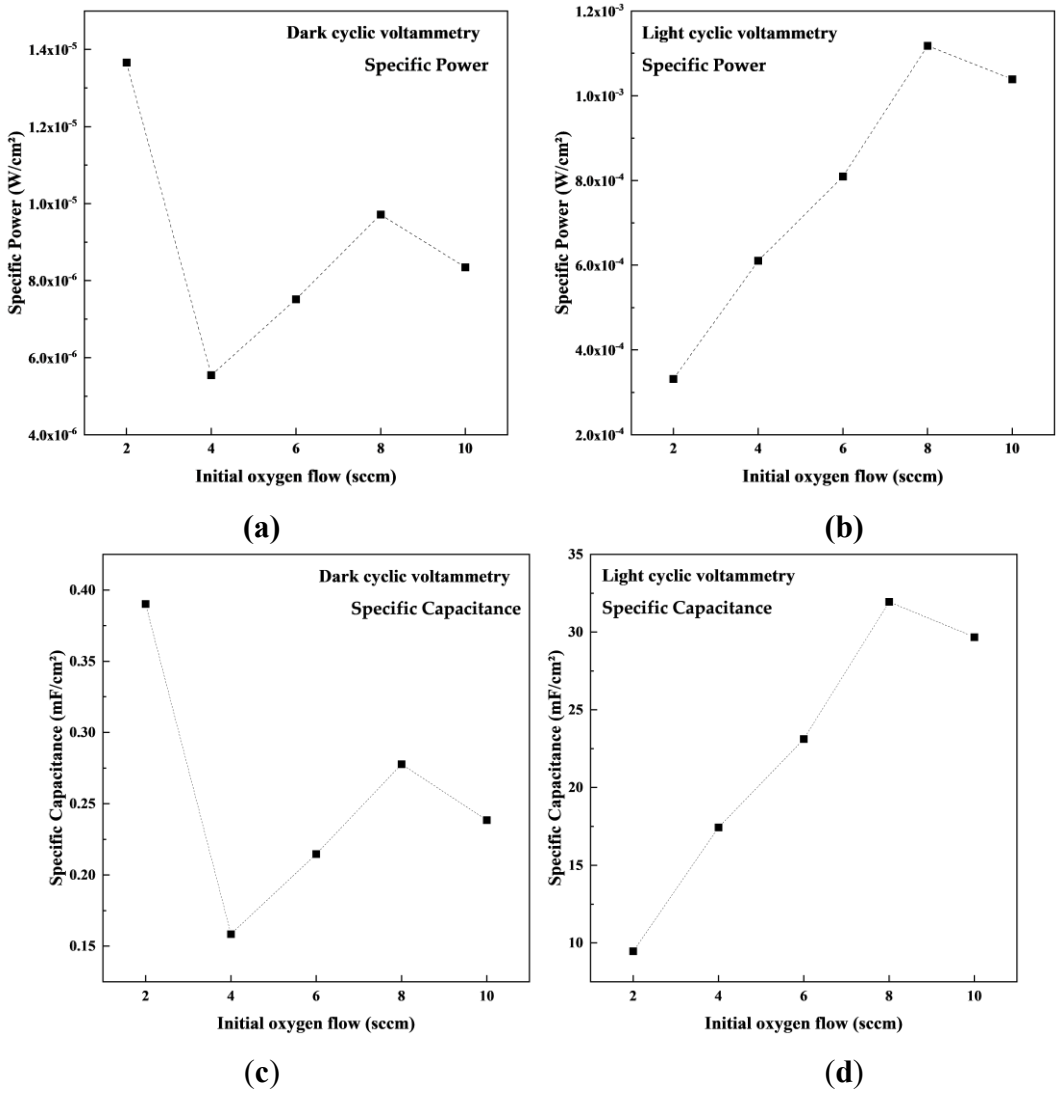

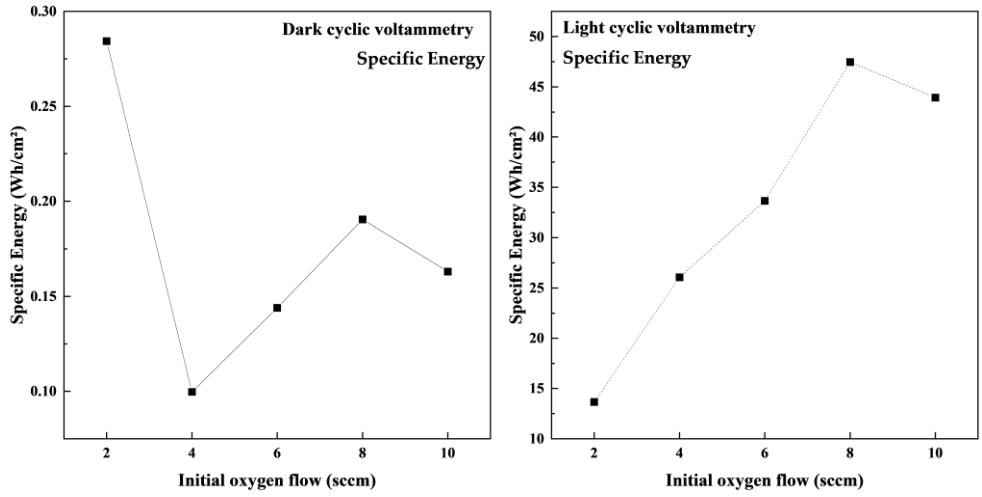

(**e**) (**f**)

Figure 23 - Influence of initial oxygen flow during deposition on electrochemical performance parameters under dark and illuminated conditions. (a, b) Specific power. (c, d) Specific capacitance. (e, f) Specific energy calculated from cyclic voltammetry data under dark and light conditions.

Table 6 - Photo-enhanced electrochemical performance metrics of WO_{3-x} electrodes extracted from cyclic-voltammetry data.

Sample	Specific Capacitance (mF/cm²)	Specific Power (W/cm²)	Specific Energy (Wh/cm²)
WO_{3-x} – 2_dark	0.29	8.0E-06	0.42
WO_{3-x} – 2_light	11.0	3.8E-04	32.4
WO_{3-x} – 4_dark	0.18	5.3E-06	0.22
WO_{3-x} – 4_light	19.8	5.5E-04	60.4
WO_{3-x} – 6_dark	0.28	7.9E-06	0.36
WO_{3-x} – 6_light	28.9	8.1E-04	86.7
WO_{3-x} – 8_dark	0.37	9.7E-06	0.49
WO_{3-x} – 8_light	39.3	1.0E-03	110
WO_{3-x} – 10_dark	0.30	8.5E-06	0.40
WO_{3-x} – 10_light	36.0	1.0E-03	109

The specific energy exhibited a similar trend: WO_{3-x}-8 again stood out with the highest value (0.490 $Wh \cdot cm^{-2}$), while WO_{3-x}-4 showed the poorest energy performance (0.225 $Wh \cdot cm^{-2}$). This superior performance of the WO_{3-x}-8 sample can be attributed to its optimized oxygen vacancy structure, which is sufficient to promote surface redox processes without compromising structural stability, unlike samples with either excess or deficiency of oxygen. Similarly, the specific power, which depends on the discharge time and the charge transport rate, also peaked for WO_{3-x}-8 (1.05×10^{-5} $W \cdot cm^{-2}$), further corroborating the excellent overall performance of this composition. These results suggest that there is an optimal concentration of oxygen vacancies that simultaneously favors charge storage mechanisms and enhances electrochemical response speed.

Oxygen vacancies are critical structural defects that drastically influence the electronic and electrochemical properties of transition metal oxides. In the case of WO_3, these vacancies introduce intermediate electronic states (donor defects) that facilitate electronic conduction and the formation of W^{5+} species [49]. However, an excessive presence of vacancies can compromise material stability and lead to the degradation of capacitive performance, as observed for the WO_{3-x}-4 sample. Conversely, in the more oxygen-rich samples, the absence of active redox species reduces faradaic storage, resulting in predominantly non-faradaic (purely capacitive) behavior.

Thus, a nonlinear relationship between oxygen content and electrochemical performance is observed. The balance between a sufficient density of oxygen vacancies enabling surface redox reactions—and an ordered structure that maintains electro-chemical stability appears to be achieved in the WO_{3-x}-8 sample, which exhibited the best results in terms of capacitance, energy, and power, as well as the highest efficiency under illumination.

Mott–Schottky (MS) analysis is a classical technique widely employed to evaluate the semiconductor–electrolyte interface properties in photoelectrochemical (PEC) systems. By measuring the interfacial capacitance (C) as a function of the applied potential (V), it is possible to extract two key parameters: the flat-band potential (V_{fb}), which indicates the alignment of energy bands with respect to the redox levels of the electrolyte; and the donor density (N_D), which provides insight into the concentration of free carriers within the semiconductor. In an ideal n-type semiconductor, a linear region in the $1/C^2$ vs. V plot is expected, where the slope is inversely proportional to N_D. In the context of PEC water splitting, these parameters are critical for assessing band energetics and carrier transport behavior under operational conditions.

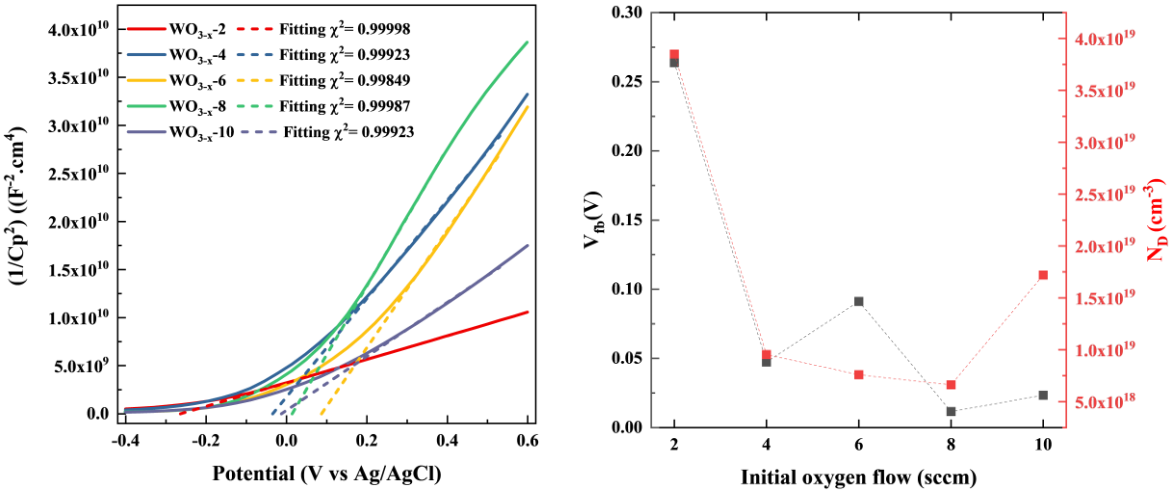

Figure 24 - (a) Mott–Schottky plots for WO_{3-x} electrodes; the dashed lines are linear fits used to extract the donor density N_D and flat-band potential V_{fb}. (b) Evolution of V_{fb} (black squares, left axis) and N_D (red circles, right axis) as a function of the initial oxygen-flow ramp employed during film deposition.

Table 7 - Flat-band potential V_{fb} and donor density N_D obtained from Mott–Schottky analysis of WO_{3-x} films as a function of the initial oxygen-flow ramp during deposition

Sample	V_{fb} (V)	N_D (cm^{-3})
WO_{3-x} – 2	0.2637	3.85×10^{19}
WO_{3-x} – 4	0.0472	9.53×10^{18}
WO_{3-x} – 6	0.0911	7.59×10^{18}
WO_{3-x} – 8	0.0116	6.61×10^{18}
WO_{3-x} – 10	0.0233	1.72×10^{19}

The $1/C^2$ vs. V curves obtained for WO_{3-x} films deposited under different initial O_2 flow ramps are shown in **Figure 24**. The corresponding values of V_{fb} and N_D, extracted from the linear region of the plots, are summarized in **Table 7**. A parabolic trend was observed in both parameters, highlighting a strong dependence on oxygen stoichiometry.

The sample WO_{3-x}-2, prepared with minimal oxygen flow, exhibited the most positive flat-band potential (V_{fb} = 0.2637 V) and the highest donor density ($N_D = 3.85 \times 10^{19}$ cm^{-3}). These values indicate a degenerate doping regime, likely due to a high concentration of oxygen vacancies acting as shallow donors. However, this excessive donor concentration can also lead to significant recombination, as evidenced by the poor photocurrent and high charge transfer resistance seen in previous electrochemical impedance spectroscopy (EIS) results.

As the oxygen flow increased to 4 and 6 sccm, both V_{fb} and N_D decreased markedly. In WO_{3-x}-4, the flat-band potential dropped to 0.0473 V and N_D to 9.53×10^{18} cm^{-3}. In WO_{3-x}-6,

V_{fb} reached 0.0912 V and N_D dropped further to 7.59×10^{18} cm^{-3}. This decrease suggests improved band alignment and a more favorable depletion layer for photoinduced charge separation. Notably, these samples also presented lower R_1 values in EIS and enhanced photocurrent response in cyclic voltammetry, demonstrating a coherent correlation across techniques.

WO_{3-x}-8 exhibited the most negative flat-band potential (V_{fb} = 0.0116 V), alongside a moderate donor density of 6.61×10^{18} cm^{-3}. The strong negative shift in V_{fb} implies an enhanced band bending, favoring the migration of holes toward the electrolyte. This sample also showed the highest interfacial capacitance (CPE_1) and the lowest charge transfer resistance under light ($R_1 \sim 2.7$ kΩ), reinforcing the hypothesis that the PEC performance is maximized when the carrier density is high enough to ensure conductivity, but not so high as to induce recombination.

At the highest oxygen flow (WO_{3-x}-10), V_{fb} increased slightly (0.0234 V), while N_D rose to 1.72×10^{19} cm^{-3}. This partial recovery in carrier density might result from a reintroduction of sub-stoichiometric defects. Nevertheless, the structural and optical characterizations indicated lower crystallinity and reduced visible light absorption in this sample, which together with its relatively high R_p value in EIS, compromise its overall PEC efficiency.

Importantly, the MS results are consistent with trends observed in the optical bandgap and surface wettability. The samples with intermediate oxygen flow (WO_{3-x}-6 and WO_{3-x}-8) presented lower bandgaps (~3.0 eV), higher polar surface free energy, and better contact angle performance, indicating a synergistic effect among structural order, surface chemistry, and electronic properties.

In summary, Mott–Schottky analysis confirms that the initial oxygen flow modulates the electronic structure of WO_{3-x} films, primarily by controlling the density of donor-like oxygen vacancies and shifting the flat-band potential. Optimal PEC performance is achieved in a narrow window (6–8 sccm), where charge carrier density, interfacial energetics, and structural properties are all favorably balanced.

The combined photoelectrochemical analyses reveal that the performance of WO_{3-x} thin films is strongly governed by the interplay between oxygen vacancy concentration and the resulting modifications in interfacial energetics, charge transport, and redox activity.

Electrochemical impedance spectroscopy (EIS) demonstrated that samples synthesized with intermediate oxygen flow (WO_{3-x}-6 and WO_{3-x}-8) exhibit the lowest charge transfer resistance (R_1), highest interfacial capacitance (CPE_1), and significantly enhanced photoconductive behavior under illumination. These results reflect a favorable balance between

electrical conductivity and interfacial band alignment, enabling efficient separation and transport of photoinduced carriers. Mott–Schottky analysis further supported these findings, revealing optimized flat-band potentials and moderate donor densities in the same samples, which correlated well with improved charge carrier dynamics and enhanced band bending at the semiconductor/electrolyte interface. Notably, WO_{3-x}-8 exhibited the most negative V_{fb} and ideal donor concentration, reinforcing its superior charge separation efficiency and PEC behavior. Complementarily, cyclic voltammetry measurements revealed a clear distinction between faradaic and non-faradaic regimes across the series. The WO_{3-x}-2 and WO_{3-x}-4 films showed distinct anodic peaks associated with $W^{5+} \rightarrow W^{6+}$ oxidation, indicating the prevalence of redox-active species stabilized by oxygen vacancies under dark conditions. However, only WO_{3-x}-8 demonstrated a strong, stable photocurrent under illumination, along with the highest values of specific capacitance, energy, and power, suggesting that an optimal concentration of oxygen vacancies not only promotes efficient charge storage and redox activity but also preserves structural integrity. Taken together, the integrated analysis confirms that a nonlinear, defect-mediated regime governs the PEC properties of WO_{3-x} films, with the WO_{3-x}-8 composition representing a critical point of functional optimization. This synergy between structural, optical, and electrochemical properties underscores the importance of precise oxygen modulation during deposition to maximize the material's photoelectrochemical performance.

4.1.5 Partial Conclusions

The comprehensive characterization of the WO_{3-x} thin films allowed for a deeper understanding of how deposition conditions influence their structural, optical, surface, electrochemical, and functional properties. XRD and Raman analyses confirmed the formation of the γ-monoclinic phase in all samples, with no clear evidence of vibrational features associated with significant oxygen vacancy concentrations. SEM imaging revealed a nanoplatelet morphology, with variations in compaction and roughness, which correlated with the differences in film thickness determined by profilometry.

In terms of optical behavior, samples deposited under lower oxygen flow exhibited more intense coloration, lower transmittance, and a slight bandgap reduction, features consistent with the presence of mid-gap states and partial reduction of W^{6+}. The WO_{3-x}–8 sample showed the highest transmittance and bandgap, along with an absence of defect-related Raman modes, suggesting a less defective structure compared to the others.

Electrochemical analyses through EIS, Mott–Schottky plots, and cyclic voltammetry provided a broad view of the photoelectrochemical performance of the materials. WO_{3-x}–8

exhibited the lowest charge transfer resistance and highest carrier density, which translated into superior photocurrent generation. Cyclic voltammetry revealed distinct behaviors among the samples, with prominent anodic peaks observed in WO_{3-x}–2 and WO_{3-x}–4 around –0.1 V (vs Ag/AgCl), assigned to the oxidation of W^{5+} to W^{6+}, and detected exclusively under dark conditions, highlighting the influence of tungsten redox states on the electrochemical response.

Although an oxygen gradient strategy was applied during film deposition, all samples were subsequently subjected to thermal treatment in ambient atmosphere at 450 °C for two hours. This annealing step likely promoted the reoxidation of the films, potentially attenuating or even reversing the oxygen stoichiometry gradient initially induced during deposition. The only exception was the WO_{3-x}–2 sample, which remained dark-colored after the heat treatment, suggesting the retention of reduced tungsten states and possibly a higher concentration of oxygen vacancies. From WO_{3-x}–4 onward, all samples exhibited clear appearance and high transmittance, indicating that thermal treatment had a homogenizing effect on the final stoichiometry. This factor must be considered when interpreting the optical and functional properties of the films, particularly when correlating deposition conditions with post-treatment behavior.

The thermal treatment in ambient atmosphere, however, led to the near-complete oxidation of the films, effectively erasing the originally imposed gradient and homogenizing the composition of the higher-index samples. Only WO_{3-x}–2 and WO_{3-x}–4 partially preserved the oxygen distribution, as corroborated by the presence of a characteristic anodic peak in the cyclic voltammetry curves, indicating the persistence of regions still rich in oxygen vacancies. This result highlights the necessity of employing inert atmospheres, such as argon or nitrogen, in subsequent thermal treatments in order to maintain the stoichiometric profile and enable the isolated investigation of the effects of oxygen vacancies on the photoelectrochemical response.

In summary, this study demonstrated that fine control of the O_2 flow during deposition and the appropriate choice of annealing atmosphere are decisive tools for modulating the structure–property–performance relationship in WO_{3-x} films. Maintaining a stable gradient simultaneously enhances light harvesting, charge separation, and interfacial kinetics, thus establishing clear guidelines for the optimization of photoelectrodes intended for green hydrogen production.

4.2 WO_{3-x} thin films by RGPP

4.2.1 Morphological and Compositional Characterization of WO_{3-x} Thin Films by RGPP

This section presents the morphological and compositional characterization of WO_{3-x} thin films deposited via Reactive Gas Pulsing Process (RGPP), comparing samples deposited at 60% and 90% of P. Analyses include Scanning Electron Microscopy (SEM), Energy Dispersive X-ray Spectroscopy (EDX), and X-ray Photoelectron Spectroscopy (XPS) performed before and after thermal treatment in ambient air and argon.

SEM Analysis

Top-view SEM images reveal that, prior to thermal treatment, the surface morphology of the films is mostly featureless, especially for the 60% duty cycle sample. After annealing, grain boundaries become visible in both air and argon conditions, suggesting thermally induced crystallization. The 90% duty cycle samples show a more textured and granular morphology even before annealing, indicating that a higher oxygen exposure during deposition promotes surface ordering. These morphological differences are illustrated in **Figure 25**, which displays the SEM images of WO_{3-x} films deposited at both 60% and 90% duty cycles before and after annealing.

Cross-sectional images show that, for most samples, the internal structure remains dense and amorphous before annealing. The exception is the 90% duty cycle film, which exhibits a partially columnar microstructure prior to annealing and a more defined, continuous columnar arrangement after thermal treatment. This confirms a stronger effect of annealing on the microstructure for films deposited with high oxygen exposure.

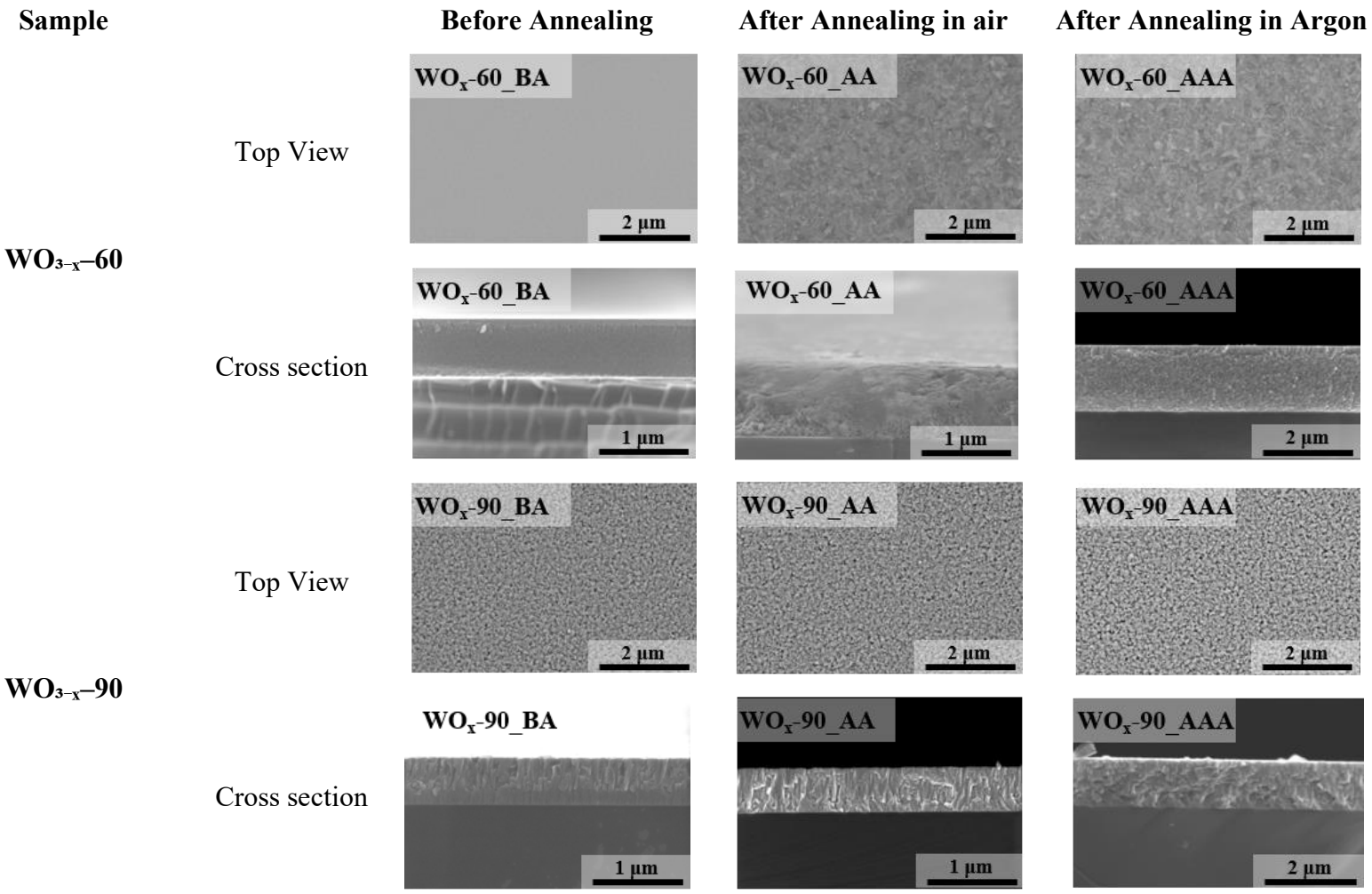

Figure 25 - SEM images of WO_{3-x} thin films deposited at 60% and 90% duty cycles, before and after annealing in air and argon. Top-view and cross-section images are shown.

EDX Analysis

EDX analysis confirmed that all samples are composed predominantly of tungsten (W) and oxygen (O), with compositions varying slightly depending on the duty cycle and thermal treatment condition (**Table 8**). For the 60% duty cycle films, oxygen content increased from 70.28 at. % (before annealing) to 73.70 at. % and 73.95 at. % after annealing in air and argon, respectively. A similar trend was observed for the 90% duty cycle films, which showed an increase from 74.29 at. % (before annealing) to 73.90 at. % (air) and 74.38 at. % (argon).

Correspondingly, the tungsten content decreased as the oxygen content increased. These results suggest that thermal treatment slightly enhances oxygen incorporation, particularly under argon atmosphere, possibly due to reordering or oxidation of oxygen-deficient regions. Nevertheless, the overall W:O stoichiometry remains within the expected range for sub-stoichiometric tungsten oxide films (WO_{3-x}), consistent with literature-reported values for reactive sputtered WO_3 [85,87]. These results indicate that thermal treatment influences film morphology but does not significantly alter the overall stoichiometry.

Table 8 - EDX results of WO_{3-x} thin films before and after annealing, for 60% and 90% of P.

Sample	Condition	O (at. %)	W (at. %)
WO_{3-x}–60	Before Annealing	70.28	29.72
	After Annealing in air	73.70	26.30
	After Annealing in Argon	73.95	26.05
WO_{3-x}–90	Before Annealing	74.29	25.71
	After Annealing in air	73.90	26.10
	After Annealing in Argon	74.38	25.62

XPS Analysis

XPS was performed to probe the surface chemical environment and oxidation states. Survey spectra (**Figure 26**) confirmed the presence of W, O, and C in all samples, with minor N traces in as-deposited samples.

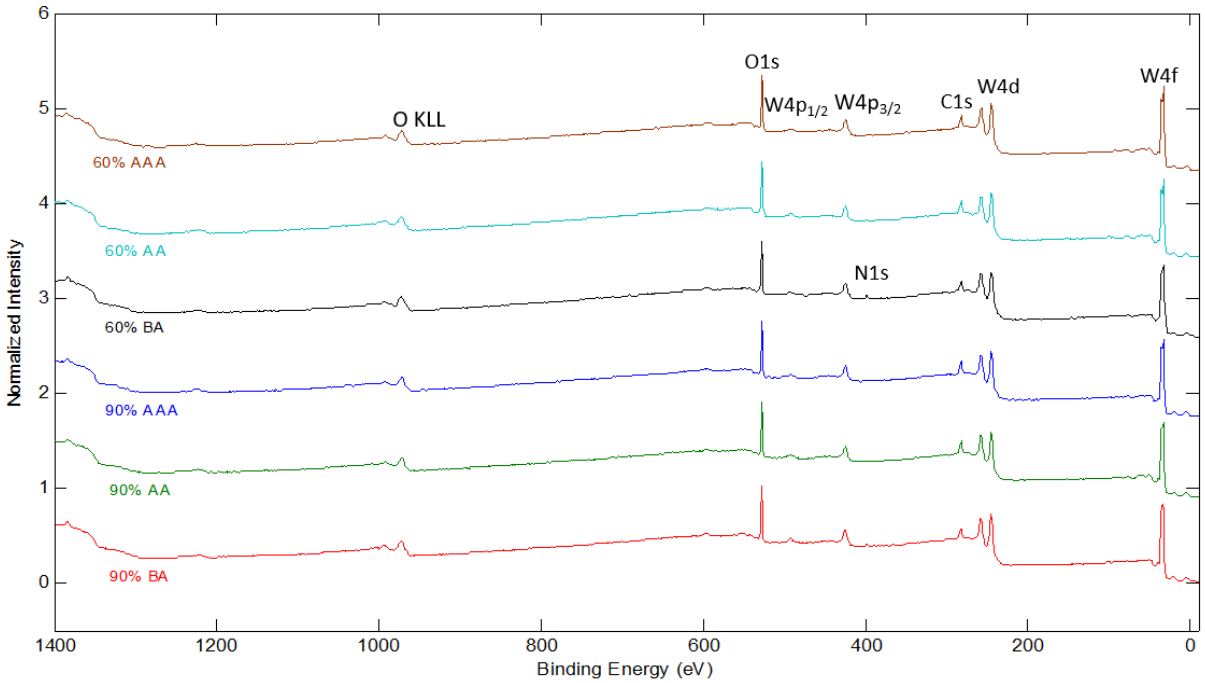

Figure 26 - XPS Survey Spectra of WO_x Films for the samples with 60% of P, the brown curve represents the film annealed in argon (60 AAA), the cyan curve indicates the film annealed in air (60 AA), and the black curve shows the as-deposited sample (60 BA). For the samples with 90% of P, the blue curve depicts the argon-annealed film (90 AAA), the green curve shows the air-annealed film (90 AA), and the red curve represents the as-deposited sample (90 BA).

C 1s spectra (**Figure 27**) revealed typical surface carbon contamination, with contributions from C–C, C–O, and C=O bonds. Slight increases in C–O/C=O contributions were observed after annealing, suggesting increased surface adsorption.

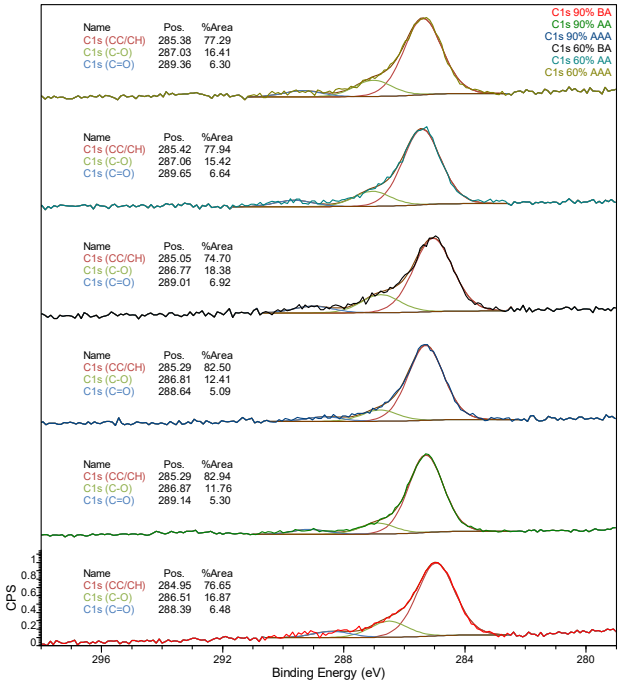

Figure 27 - Deconvoluted high-resolution C 1s spectra. For the samples with 60% of P, the brown curve represents the film annealed in argon (60 AAA), the cyan curve indicates the film annealed in air (60 AA), and the black curve shows the as-deposited sample (60 BA). For the samples with 90% of P, the blue curve depicts the argon-annealed film (90 AAA), the green curve shows the air-annealed film (90 AA), and the red curve represents the as-deposited sample (90 BA).

O 1s spectra (**Figure 28**) exhibited three components: lattice oxygen (~530.8 eV), hydroxyl or adsorbed species (~532 eV), and oxidized carbon (~533 eV). Annealed samples, especially in argon, presented higher hydroxyl contributions, consistent with increased surface reactivity.

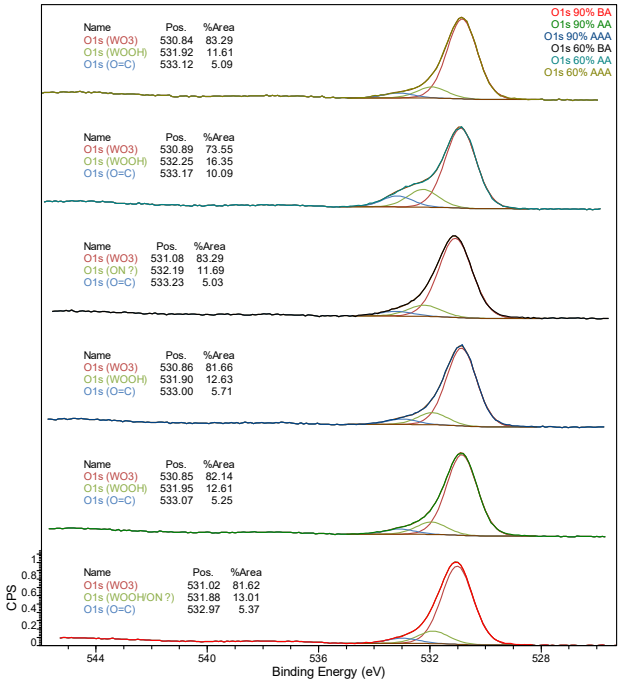

Figure 28 - Deconvoluted high-resolution O 1s spectra. For the samples with 60% of P, the brown curve represents the film annealed in argon (60 AAA), the cyan curve indicates the film annealed in air (60 AA), and the black curve shows the as-deposited sample (60 BA). For the samples with 90% of P, the blue curve depicts the argon-annealed film (90 AAA), the green curve shows the air-annealed film (90 AA), and the red curve represents the as-deposited sample (90 BA).

W 4f spectra (**Figure 29**) confirmed W^{6+} as the dominant oxidation state in all samples, with doublets at ~36.1 eV (W 4f7/2) and ~38.2 eV (W 4f5/2). In the 60% BA sample, additional peaks corresponding to W^{5+} or W–N species were detected, which disappeared after annealing.

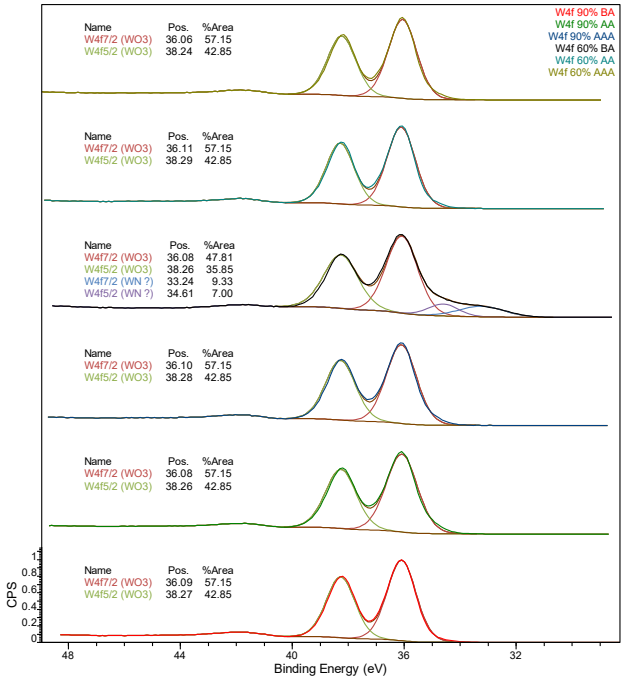

Figure 29 - Deconvoluted high-resolution W 4f spectra. For the samples with 60% of P, the brown curve represents the film annealed in argon (60 AAA), the cyan curve indicates the film annealed in air (60 AA), and the black curve shows the as-deposited sample (60 BA). For the samples with 90% of P, the blue curve depicts the argon-annealed film (90 AAA), the green curve shows the air-annealed film (90 AA), and the red curve represents the as-deposited sample (90 BA).

N 1s spectra (**Figure 30**) showed minor signals (~397–402 eV) in as-deposited samples, consistent with surface-adsorbed NO or NH_4^+ species. These signals were not detected after annealing.

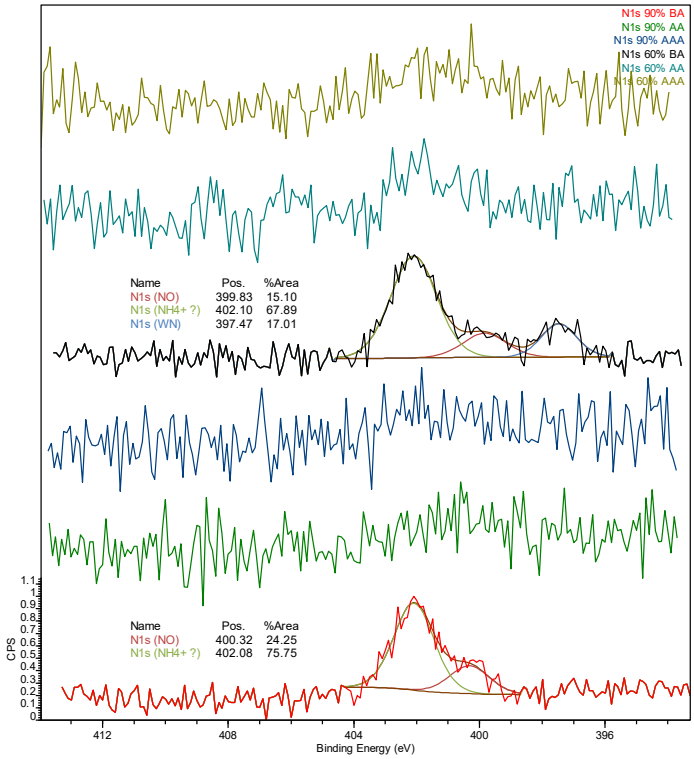

Figure 30 - Deconvoluted high-resolution N 1s spectra. For the samples with 60% of P, the brown curve represents the film annealed in argon (60 AAA), the cyan curve indicates the film annealed in air (60 AA), and the black curve shows the as-deposited sample (60 BA). For the samples with 90% of P, the blue curve depicts the argon-annealed film (90 AAA), the green curve shows the air-annealed film (90 AA), and the red curve represents the as-deposited sample (90 BA).

Overall, the XPS results confirm the presence of stoichiometric WO_3 with surface variations depending on annealing and deposition conditions. The data align with trends reported in the literature regarding oxidation states and surface composition of sputtered WO_{3-x} films.

4.2.2 Structural and Optical Characterization of WO_{3-x} Thin Films

This section presents the structural and optical characterization of WO_{3-x} thin films deposited via RGPP. X-ray diffraction (XRD) was used to investigate the crystallographic phases and the impact of annealing and oxygen pulsing on film crystallinity. Optical properties were assessed by UV–Vis transmittance spectroscopy, focusing on transparency, absorption edges, and their correlation with structural ordering. Together, these analyses provide insights into how processing parameters influence both the short-range and long-range order and the optical properties of the films.

XRD measurements

The X-ray diffraction patterns for the 60% P samples, deposited on silicon substrates under different annealing atmospheres, are shown in **Figure 31(a)**. Before thermal treatment, the samples were amorphous, with only reflections from the Si (100) substrate observed. After annealing at 450°C in air, the diffraction pattern revealed clear peaks at 23.1°, 23.6°, and 24.3° 2θ, followed by additional peaks at 33.1°, 34.1°, and 36.7° 2θ. These reflections correspond to the (002), (020), (200), (022), (202), and (–222) planes of monoclinic γ-WO_3 (ICDD PDF 01-089-4476). No metallic tungsten or sub-oxides were observed, confirming the pure formation of γ-WO_3.

In **Figure 31(b)**, the diffractograms for the 90% of P sample on silicon substrate are shown, exhibiting a completely different behavior compared to the 60% of P samples. Starting with the untreated sample, a well-defined and intense peak at 22.15° is observed, corresponding to the monoclinic WO_3 phase, indexed to the (002) plane. After thermal treatment in both atmospheres, the samples show the same behavior, indicating the monoclinic phase. This is consistent with the SEM results, where the 90% of P sample, prior to thermal treatment, already exhibits a columnar morphology with well-defined grain boundaries, suggesting it is already ordered without thermal treatment.

Additionally, these 60% P and 90% P samples, analyzed by X-ray diffraction, were also studied using XPS. The XPS results confirmed the presence of tungsten exclusively in the W^{6+} oxidation state, which is consistent with the formation of stoichiometric WO_3 in both cases, as indicated by the diffraction data.

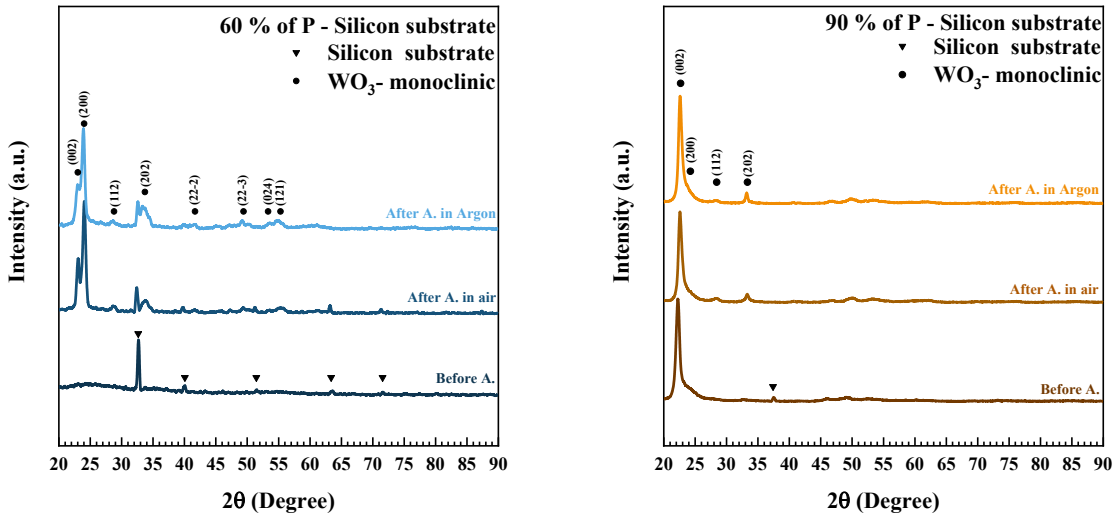

Figure 31 - GIXRD patterns of WO_{3-x} films deposited on Si(100) substrates using Reactive Gas Pulsing Process (RGPP) at (a) 60 % and (b) 90 % duty cycles. The diffractograms show the evolution of crystalline phases before annealing and after annealing in air and argon.

Figure 32(a) presents the diffractograms for the 60% P samples on glass substrates. Starting with the as-deposited films, they were amorphous. After annealing at 450°C, both in air and argon atmospheres, the diffraction patterns revealed a consistent set of reflections, predominantly corresponding to the monoclinic γ-WO_3 phase. The main peaks were observed at 2θ values of 22.9°, 23.44°, 24.14°, 25.67°, 28.67°, 32.43°, 33.14°, 35.25°, 41.52°, 48.15°, 49.70°, 50.29°, 54.05°, 62.01°, and 76.35°, which are in good agreement with the standard diffraction data for γ-WO_3 (ICDD PDF 01-089-4476). The presence of multiple sharp and well-defined reflections indicates a high degree of crystallinity of the oxide phase after annealing.

In addition to the tungsten oxide phase, new reflections at 20.6°, 26.43°, 28.02°, 29.49°, 33.90°, 35.49°, 46.97°, 51.39°, 53.31°, 54.71°, and 55.60° 2θ were observed and attributed to sodium tungstate (Na_2WO_4), as identified in the ICDD database (PDF 00-020-1163). This sodium tungsten is a result of Na^+ diffusion from the glass substrate during the thermal treatment, a phenomenon extensively documented for sputtered WO_3 films on soda-lime glass substrates [74]. The simultaneous presence of γ-WO_3 and Na_2WO_4 in both atmospheric conditions confirms the stability of this composite phase configuration in the 60% of P regime, indicating that sodium diffusion is a common occurrence in this system

For the 90% of P sample deposited on soda-lime glass and annealed at 450°C, both in air and argon atmospheres, the X-ray diffraction patterns revealed distinct phase compositions in each case (**Figure 32(b)**). Before thermal treatment, the sample was amorphous, which differs from the same 90% of P sample on silicon substrates, where a crystalline phase was

already observed. After annealing in air, the diffraction pattern displayed strong reflections characteristic of the hexagonal WO_3 phase, with the most prominent peaks at 21.13°, 23.23°, 24.03°, 27.86°, and 36.64° 2θ. These reflections align well with the hexagonal WO_3 phase, as reported in the literature [74]. Notably, no sodium tungstate (Na_2WO_4) was observed in this sample, differing from the 60% of P samples, where sodium was clearly identified as a secondary phase. Additionally, no substoichiometric WO_{3-x} phase was identified, although some peaks remain unassigned, which could suggest the presence of additional phases that require further investigation.

In contrast, for the sample annealed in argon, a more complex diffraction pattern was observed. Additional peaks appeared at 33.21°, 33.96°, 36.59°, 39.02°, 47.75°, 49.40°, 51.69°, 53.17°, 55.35°, 56.10°, 57.83°, 63.18°, 71.15°, 78.15°, and 84.25°, indicating the presence of a mixture of phases. While the hexagonal WO_3 remains the dominant phase, these additional peaks suggest the presence of other phases such as monoclinic WO_3 (γ-WO_3). The formation of these mixed phases may be related to the higher oxygen content during deposition, which is known to promote the coexistence of hexagonal and monoclinic phases, as demonstrated in previous studies [73]. The presence of these mixed phases indicates that the film grown in argon underwent different crystallization mechanisms compared to the sample annealed in air, likely due to variations in oxygen availability during annealing and the higher tungsten content in the 90% P films, which may favor the formation of multiple crystalline phases.

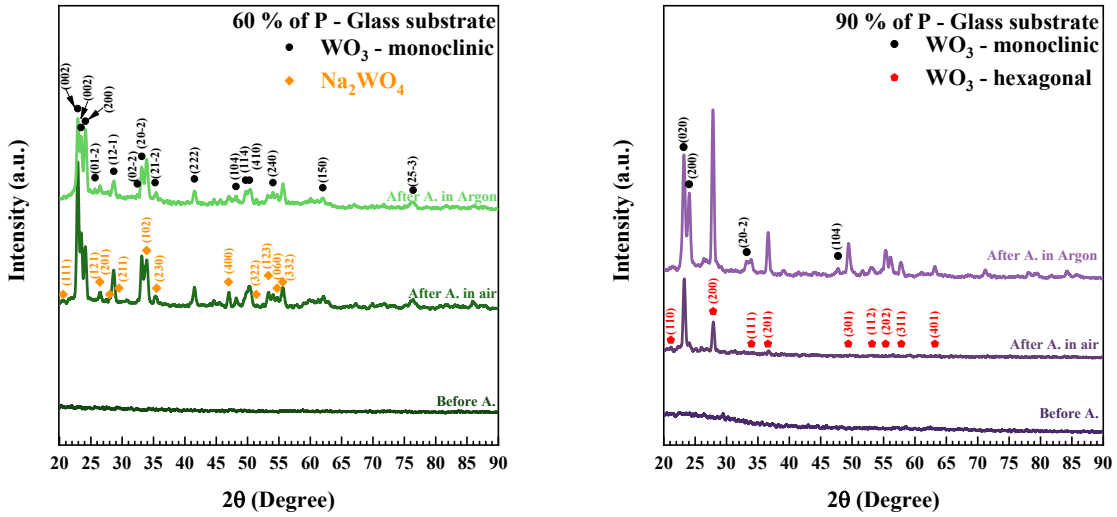

Figure 32 - GIXRD patterns of WO_{3-x} films deposited on glass substrates using Reactive Gas Pulsing Process (RGPP) at (c) 60 % and (d) 90 % duty cycles. The patterns show the samples before annealing and after annealing in air and argon.

Figure 33(a) presents the X-ray diffraction patterns for the 60% P samples deposited on FTO-coated glass substrates and annealed at 450°C, both in air and argon atmospheres, as well as before annealing. Similar to the observations for the soda-lime glass samples, the as-deposited films on FTO were amorphous, with only the characteristic reflections from the FTO substrate visible, particularly the (110), (101), and (211) peaks. After annealing in air, the monoclinic γ-WO_3 phase became predominant, with new peaks appearing at 23.1°, 23.6°, 24.3°, 33.1°, 34.1°, and 36.7° 2θ, corresponding to the (002), (020), (200), (022), and (202) planes of γ-WO_3 (ICDD PDF 01-089-4476).

In contrast to the soda-lime glass results, the diffractogram for the 60% of P sample on FTO showed a higher degree of crystallinity, with sharper and more defined peaks, suggesting better ordering. Notably, no peaks corresponding to sodium tungstate (Na_2WO_4) were detected, indicating that sodium diffusion was effectively suppressed by the FTO layer. After annealing in argon, the diffraction pattern remained virtually unchanged, confirming that the atmospheric difference had no significant impact on the phase composition or crystallinity. These findings underscore the stabilizing effect of the FTO substrate, which not only improves crystallinity but also prevents sodium diffusion, resulting in a more consistent, phase-pure WO_3 film compared to the glass-supported samples.

Figure 33(b) shows the diffraction patterns for the 90% of P samples deposited on FTO substrates and annealed at 450°C in both air and argon atmospheres, as well as before annealing. Similar to the 60% of P samples, the as-deposited films were amorphous, showing only reflections from the FTO substrate. After annealing in air, the monoclinic WO_3 phase emerged as the dominant phase, with prominent peaks at 23.1°, 23.6°, 24.3°, 33.1°, 34.1°, and 36.7° 2θ, corresponding to the (002), (020), (200), (022), and (202) planes of monoclinic γ-WO_3 (ICDD PDF 01-089-4476).

The same diffraction pattern was observed for the sample annealed in argon, with no additional phases detected, further indicating that the annealing atmosphere did not significantly affect the crystallization or phase composition of the films. The reflections from the FTO substrate (110), (101), and (211) remained the dominant peaks, reinforcing the stability of the substrate during thermal treatment. The absence of sodium tungstate or other secondary phases in both atmospheres suggests that sodium diffusion from the FTO layer was negligible in these conditions.

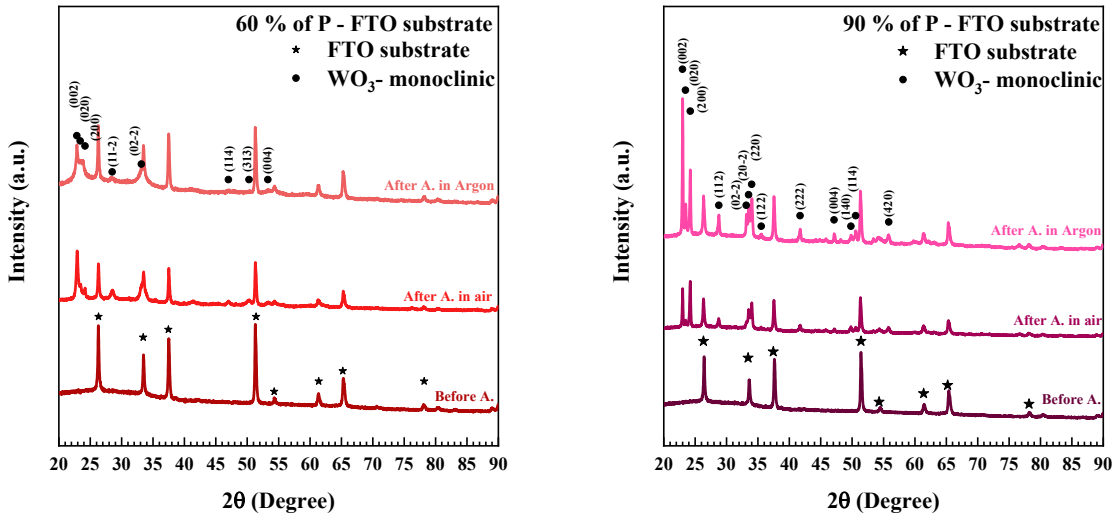

Figure 33 - GIXRD patterns of WO_{3-x} films deposited on FTO substrates using Reactive Gas Pulsing Process (RGPP) at (e) 60 % and (f) 90 % duty cycles. The diffractograms show the samples before annealing and after annealing in air and argon.

Transmittance measurements

The transmittance data, depicted in **Figure 34**, provides a detailed view of the optical properties and transparency changes before and after heat treatment.

In the first plot (**Figure 34(a)**), the transmittance of the sample deposited with 60% oxygen flow before any thermal treatment reveals relatively low transparency, typical of WO_{3-x} films at this oxygen content. The spectrum exhibits a marked absorption edge, indicating the presence of oxygen vacancies that reduce the overall optical transparency. The sample appears darker, especially in the visible region, and the transmittance decreases significantly as the wavelength decreases, reflecting a high absorption in the UV region.

Upon thermal annealing in air, the sample's transmittance shows a noticeable increase. The absorption edge shifts slightly towards higher wavelengths, and the film becomes more transparent in the visible region. This behavior suggests that the annealing process allows for a more complete oxidation of the film, reducing the number of oxygen vacancies and improving the optical quality of the film. The transmittance in the UV and visible range increases, indicating a shift towards a more stoichiometric WO_3 structure.

In contrast, the sample treated in an argon atmosphere exhibits an even more pronounced increase in transmittance, with a further shift towards higher transparency across the entire spectrum. This result suggests that the argon treatment promotes a different structural arrangement, likely favoring oxygen vacancy formation, which can enhance electronic conductivity but also improve light transmission due to the reduced scattering from vacancies.

To quantify these changes, the optical bandgap values were estimated using Tauc plots, as shown in **Figure 34(c)**. The sample with 60% oxygen flow exhibited a bandgap of approximately 2.4 eV before thermal treatment, which increased significantly to 3.1 eV after annealing in air and reached 2.9 eV after annealing in argon. These variations reflect changes in the degree of oxidation and the density of oxygen vacancies, with air treatment promoting more complete oxidation and argon treatment favoring a moderate reduction in defect states.

The second plot (**Figure 34(b)**) shows the transmittance of the WO_{3-x} sample prepared with 90% oxygen flow. Before any treatment, the sample is already more transparent than the 60% oxygen flow sample, with a noticeable increase in transparency across the visible range. This is consistent with the higher oxygen content, which likely leads to a more stoichiometric WO_3 phase, resulting in less absorption in the visible spectrum. The absorption edge also occurs at a slightly lower wavelength compared to the 60% oxygen flow sample, further supporting the reduced oxygen vacancy concentration.

Upon annealing in air, the sample with 90% oxygen flow shows minimal changes in transparency, as the structure is already closer to the fully oxidized WO_3. The main effect of this treatment is a slight broadening of the absorption edge, which may indicate some subtle shifts in the electronic structure, but the transmittance remains relatively high and consistent with the stoichiometric WO_3 phase.

For the argon treatment, the transmittance increases slightly, similar to the trend observed for the 60% oxygen flow sample. However, the increase in transparency is less pronounced compared to the 60% oxygen flow sample, indicating that the film's structure is already closer to a fully oxidized state. The argon treatment in this case likely stabilizes the oxygen vacancies, which enhances conductivity without significantly affecting transparency.

This interpretation is corroborated by the Tauc plot results in **Figure 34(d)** for the 90% oxygen flow sample. Before thermal treatment, the bandgap was 3.3 eV, increasing slightly to 3.4 eV after annealing in air, and decreasing to 3.2 eV after annealing in argon. The relatively high bandgap values across all conditions indicate a more stoichiometric composition with fewer oxygen-related defects compared to the 60% sample.

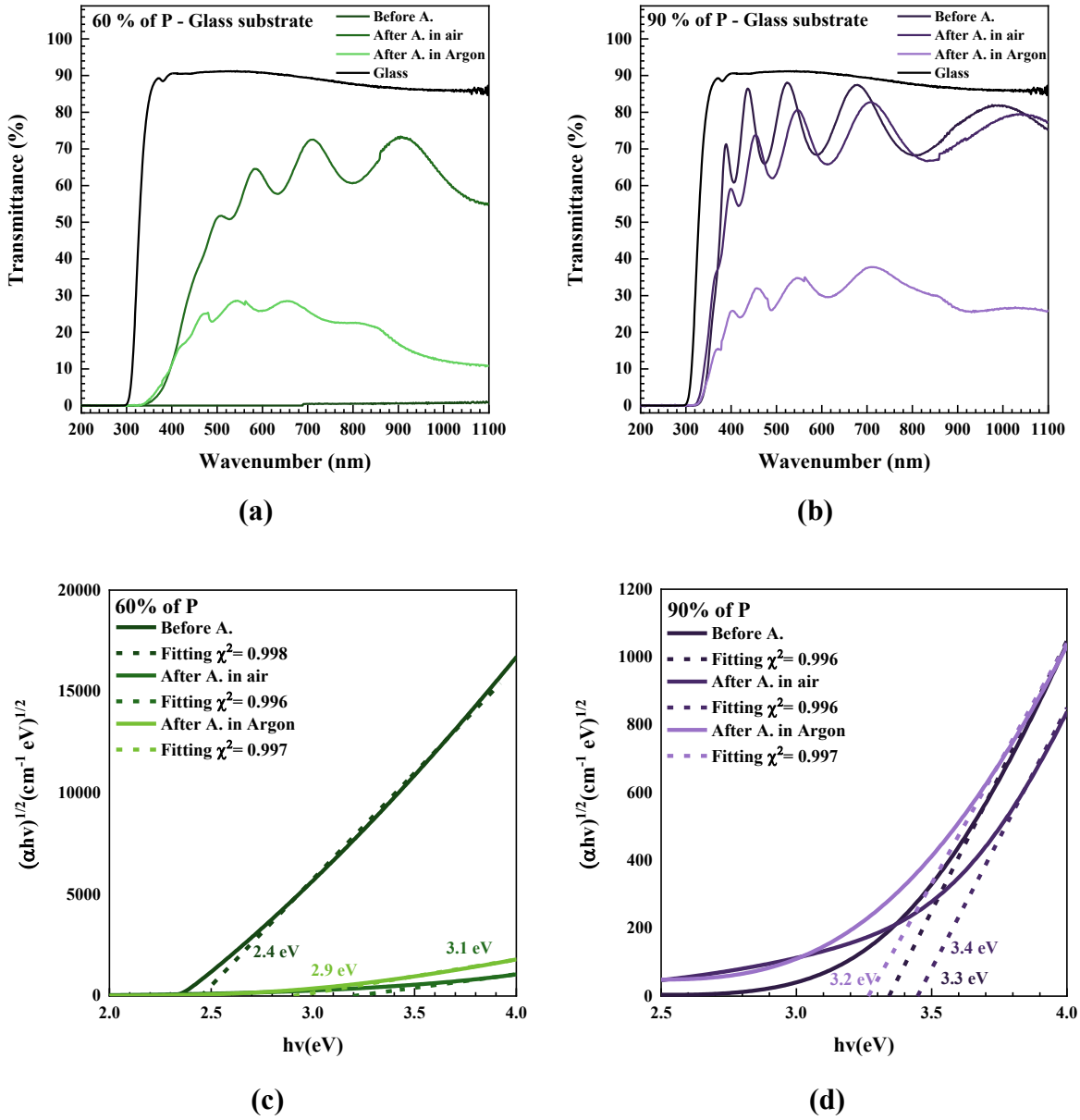

Figure 34 - Optical characterization of WO_{3-x} films deposited on glass using Reactive Gas Pulsing Process (RGPP) at 60 % (left) and 90 % (right) duty cycles. (a, b) UV–Vis transmittance spectra of the samples before and after annealing (A.) in air and argon. (c, d) Tauc plots for direct allowed transitions, used to estimate the optical band gap (E_9) of each condition.

Upon comparing the two sets of samples, it is clear that the initial transmittance for the 90% oxygen flow sample is higher than that of the 60% oxygen flow sample, both before and after thermal treatments. This suggests that higher oxygen flow during deposition results in better oxidation, leading to films with fewer oxygen vacancies and higher transparency in the visible range. The treatment in argon further enhances transparency for both samples, with the

60% oxygen flow sample showing the most significant increase, indicating that the structure benefits more from oxygen vacancy creation.

The findings from these measurements are in good agreement with those reported in the literature, such as the work by Olejníček et al. (2022), which discusses the impact of annealing on WO_{3-x} films in different atmospheres. In particular, the higher oxygen flow rates in the current study led to an increase in transparency, similar to the results observed by Olejníček et al., where oxygen-rich films exhibited better optical performance, particularly after annealing in argon, due to enhanced photoactivity and the stabilization of the monoclinic WO_3 phase [73].

In conclusion, the comparison of the two sets of films underscores the role of oxygen flow during deposition and post-deposition thermal treatments in tuning the optical properties of WO_{3-x} thin films. The 90% oxygen flow sample, already close to the stoichiometric WO_3 phase, showed less variation upon annealing, while the 60% oxygen flow sample exhibited more significant changes, indicating that sub-stoichiometric films are more sensitive to post-deposition treatments.

4.2.3 Partial Conclusions

The morphological, structural, compositional, and optical characterization of WO_{3-x} thin films obtained by magnetron sputtering using the Reactive Gas Pulsing Process (RGPP) provided a comprehensive understanding of the effects of deposition conditions (60% and 90% of P) and subsequent thermal treatments (in air and argon).

From a morphological standpoint, SEM analyses showed that films deposited with 90% of P exhibited a more textured and granular surface even before annealing, whereas films deposited with 60% of P initially presented a smooth surface, with evidence of thermally induced crystallization after treatment. The formation of a columnar structure in the 90% P films, especially after annealing, indicates a higher degree of ordering induced by increased oxygen exposure during deposition. The elemental composition obtained by EDX showed a slight additional incorporation of oxygen after thermal treatments, with an increase in O content and a corresponding decrease in W content in both regimes.

XPS analyses revealed the predominance of the W^{6+} oxidation state in all samples, corroborating the formation of stoichiometric WO_3. Secondary signals of W^{5+} and nitrogen-containing species were detected only in the as-deposited samples and were eliminated after annealing.

GIXRD analysis revealed differences between the samples depending on both the pulsing parameter and the type of substrate. The 60% P samples initially exhibited amorphous

behavior, with crystallization of the monoclinic γ-WO_3 phase occurring only after annealing. On soda-lime glass substrates, in addition to the γ-WO_3 phase, the presence of Na_2WO_4 was observed, clear evidence of sodium diffusion from the substrate during thermal treatment. In contrast, the 90% P sample deposited on glass, after annealing in air, showed the formation of both monoclinic and hexagonal WO_3 phases, with no signs of sodium contamination. On FTO-coated substrates, both the 60% and 90% P samples exhibited only the monoclinic WO_3 phase, with no secondary phases and only the characteristic peaks of the substrate itself.

In the optical measurements, the transmittance data and Tauc plots indicated that the optical bandgap varied significantly with the thermal treatment and oxygen content. For the 60% P films, the bandgap increased from 2.4 eV to 3.1 eV after annealing in air, while for the 90% P films, the values remained around 3.3 eV to 3.4 eV, reflecting a higher degree of initial stoichiometry.

Taken together, the results demonstrate that the RGPP technique is effective for fine control of WO_{3-x} film properties, allowing for the adjustment of morphology, crystallinity, stoichiometry, and optical properties through the control of pulse parameters and annealing atmosphere. Additionally, these results indicate that the type of substrate influences the formation of secondary phases: the presence of the FTO layer acts as an efficient barrier against sodium diffusion, whereas soda-lime glass promotes the formation of compounds such as Na_2WO_4. Similarly, the annealing atmosphere directly affects the type of crystalline phase formed, the number of surface defects, and optical conductivity, with the argon atmosphere being more favorable to oxygen vacancy generation, while air promotes complete oxidation of the structure.

4.3 g-C_3N_4

4.3.1 Structure, morphology and composition

To assess the morphology of the samples, field emission scanning electron microscopy (FE-SEM) measurements were performed. The obtained images are shown in **Figure 35**. It can be observed that the samples exhibit an irregular and aggregated morphology, which remains unchanged with increasing thermal treatment temperature.

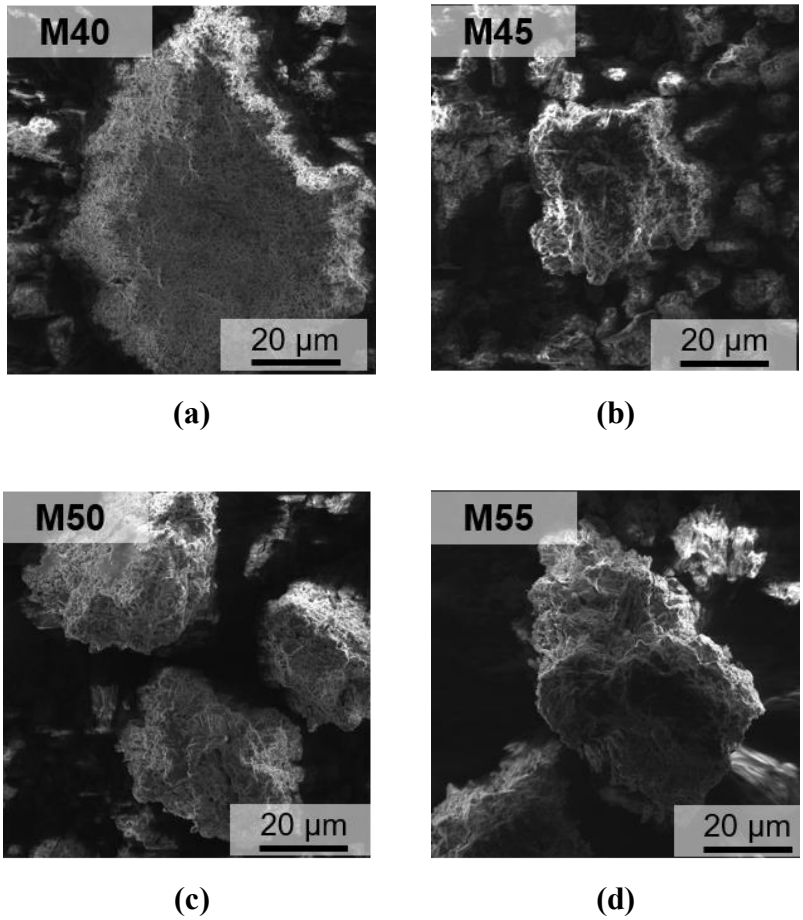

Figure 35 - SEM micrographs of g-C_3N_4 powders synthesized at different polymerization temperatures.

To characterize the chemical composition of the samples, energy-dispersive X-ray spectroscopy (EDX) measurements were performed. The EDX results are presented in **Table 9**. It can be observed that all samples are composed exclusively of carbon and nitrogen, indicating that no contamination occurred during the synthesis process.

Table 9 - Chemical composition of the samples obtained by EDX.

Sample	C (%)	N (%)
M40	36.2	63.8
M45	37.7	62.3
M50	40.7	59.3
M55	39.1	60.9

To analyze the functional groups and chemical structure of the samples, Fourier-transform infrared spectroscopy (FT-IR) measurements were performed. **Figure 36** compiles

the FT-IR spectra of uncalcined melamine (M) and of samples thermally treated at 400 °C (M40), 450 °C (M45), 500 °C (M50) and 550 °C (M55), enabling a molecular-level assessment of the polycondensation that converts the triazine precursor into progressively extended heptazine units. Within the 3 600–3 000 cm^{-1} range, melamine displays three sharp bands centred at 3 470, 3 420 and 3 330 cm^{-1}, assigned to the asymmetric and symmetric stretching modes of NH_2 groups linked through hydrogen bonding [89]. The systematic attenuation of these modes, culminating in their near disappearance in M50 and M55, attests to deamination and to the formation of N-bridging $(C)_3$ linkages characteristic of melem, melon and, ultimately, g-C_3N_4. The broad residual feature at 3 400–3 200 cm^{-1} in M55 is consistent with terminal –NH stretching and/or O–H species adsorbed on the graphitic surface [90].

Marked spectral changes concentrate between 1 650 and 1 200 cm^{-1}, the domain of skeletal C=N/C–N vibrations. Melamine presents narrow bands at 1 650, 1 578, 1 465 and 1 425 cm^{-1}, reflecting the high triazine symmetry conjugated to NH_2 groups [89]. From 450 °C onwards these vibrations coalesce into a broad envelope spanning 1 630–1 240 cm^{-1}; its amplitude and definition increase up to 550 °C, mirroring the extension of π-conjugation within the heptazine network that typifies g-C_3N_4 [90]. The 1 000–600 cm^{-1} region provides the most specific signature of polycondensation. The ring-breathing band at ~808 cm^{-1} is already present in melamine with moderate intensity, arising from out-of-plane deformation of the s-triazine ring [60,61]. During heat treatment this mode intensifies markedly at 450 °C and remains well defined at 500 and 550 °C.

Overall, the spectral evolution demonstrates that substantial conversion of melamine to nitrogen-rich graphitic structures occurs between 500 °C and 550 °C: NH_2 vibrations are almost completely suppressed, the characteristic C=N/C–N envelope between 1 630 and 1 240 cm^{-1} becomes consolidated, and the 808 cm^{-1} band remains intense yet now anchored to an extended heptazine framework. Although FT-IR provides robust qualitative evidence of this polycondensation process, a finer distinction between intermediates (melem, melon) and fully graphitic g-C_3N_4 requires crystallographic confirmation, which will be presented in the subsequent XRD section.

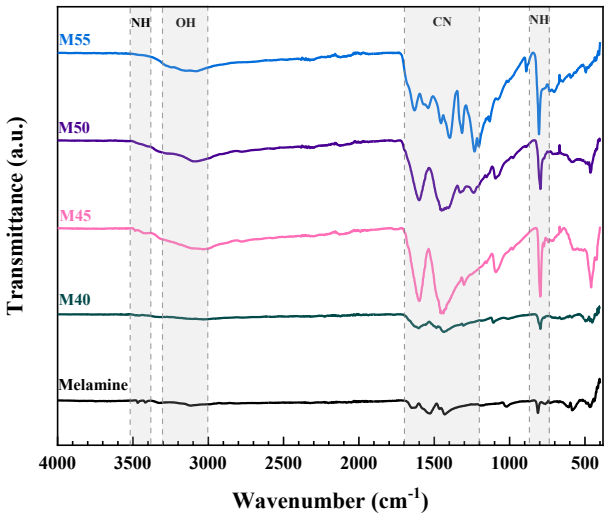

Figure 36 - FTIR spectroscopy measurements of the Melamine, M40, M45, M50, and M55 samples.

To analyze the crystalline phases of the samples, X-ray diffraction (XRD) measurements were performed, as shown in **Figure 37**. A gradual transition from the melamine structure to g-C_3N_4 can be clearly observed in the XRD patterns. g-C_3N_4 (ICSD 2217016) is identified by its characteristic peaks at approximately 13.1° and 27.3°, corresponding to the (100) and (002) planes, respectively [91]. These peaks indicate the formation of the desired polymeric structure. Based on the results, it can be concluded that the g-C_3N_4 structure is more distinctly and predominantly formed in the sample thermally treated at 550 °C, suggesting that this is the optimal temperature for the synthesis of the target material.

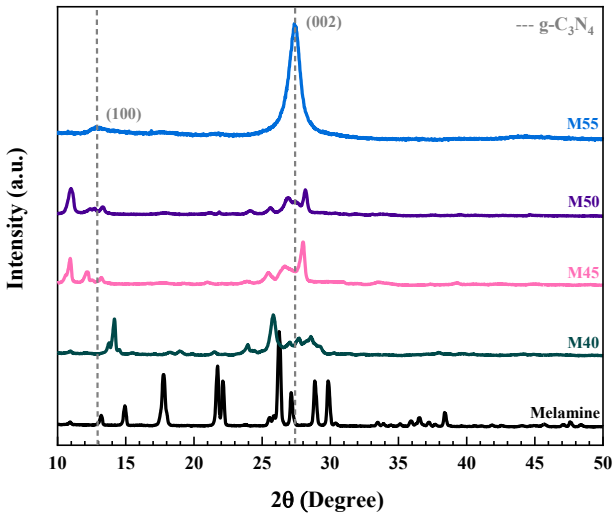

Figure 37 - XRD patterns of melamine-derived samples calcined at 400 °C (M40), 450 °C (M45), 500 °C (M50), and 550 °C (M55). The reflections at ~13.1° and ~27.4° correspond to the (100) and (002) planes of g-C_3N_4 (ICSD 2217016), associated with in-plane structural order and interlayer stacking, respectively

In continuation of the structural analyses previously discussed by FTIR and XRD, Raman spectroscopy was employed to provide a more refined understanding of the vibrational and electronic transformations occurring between the melamine precursor sample (MP) and the thermally treated material at 550 °C (M55). The Raman spectrum of MP (**Figure 38(a)**) exhibits well-defined bands at 123.7, 151.4, 383.2, 449.6, 583.3, 677.3, 778.6, 983.4, 1443.0, and 1555.0 cm^{-1}, along with additional low-frequency modes revealed using a 1800 gr/mm grating (**Figure 38(b)**). These features are characteristic of bending and torsional vibrations of the triazine units typical of melamine. This set of bands, along with the low fluorescence background, confirms that the structure remains weakly condensed, in agreement with the breathing band at 810 cm^{-1} observed in the FTIR spectrum.

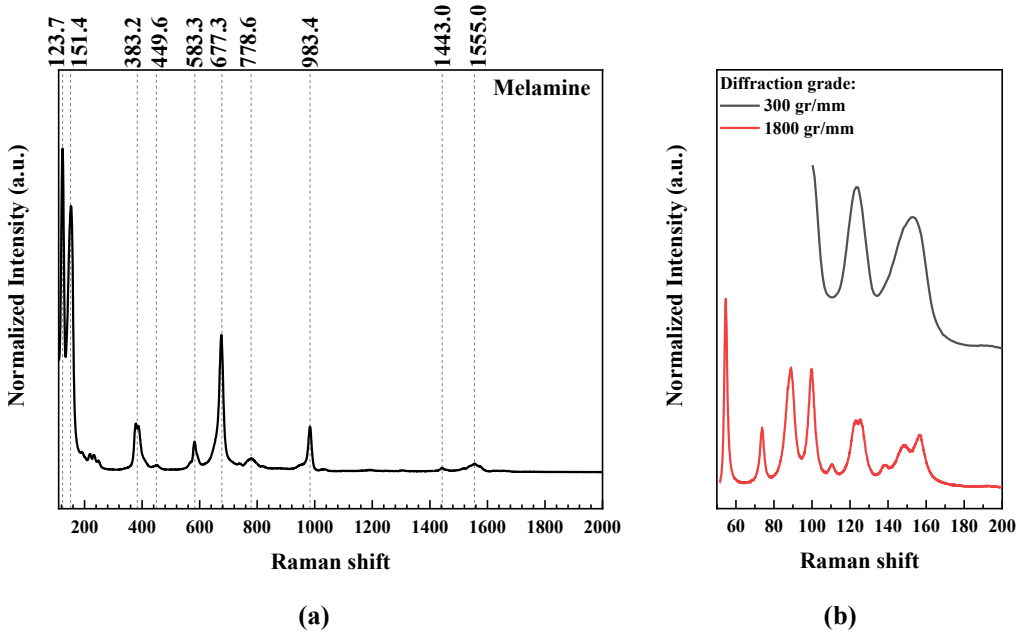

Figure 38 - (a) Raman spectra of melamine sample and (b) zoom-in of the 50-200 cm^{-1} region using 300 gr/mm (black line) and 1800 gr/mm (red line) diffraction grades.

After thermal treatment, the Raman spectrum of M55 (**Figure 39**) displays intense background fluorescence and a set of broad bands centered at 361.4, 482.4, 709.0, 762.2, 982.0, 1129.1, 1155.8, 1236.8, and 1314.1 cm^{-1}. The emergence of these modes, accompanied by the attenuation of those characteristic of melamine, indicates the formation of a graphitic g-C_3N_4 network. The band positions at 709/762 cm^{-1} (out-of-plane deformations) and 361/482 cm^{-1} (interlayer torsions) reproduce, within experimental resolution, the values reported by Jiang et al. for bulk g-C_3N_4 materials. Additionally, the slight blue-shift of the C(sp^2) bending mode—from 1234 cm^{-1} in the bulk to 1237 cm^{-1} in the present sample—suggests a certain degree of confinement, although insufficient to characterize mono- or bilayer nanosheets [92].

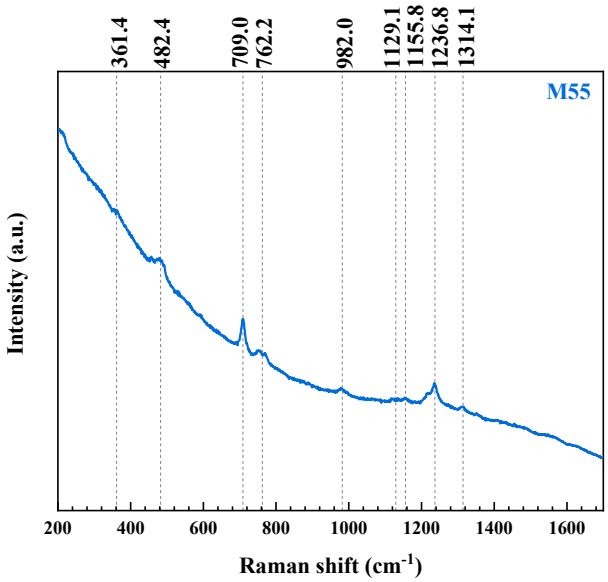

Figure 39 - Raman spectra of melamine treated at 550 ºC (M55)

The correlation between FTIR, XRD, and Raman thus outlines a coherent scenario: (i) the FTIR bands remain practically unchanged, confirming that polycondensation preserves the s-triazine framework; (ii) the XRD data reveal the formation of the (100) and (002) planes of g-C_3N_4, particularly pronounced in M55; and (iii) the Raman results capture the chemical conversion, showing that M55 exhibits a more ordered graphitic network, whereas Melamine retains the vibrational signature of melamine. These findings are consistent with recent literature and reinforce that calcination at 550 °C is a critical condition to achieve the desired polymeric structure.

4.3.2 Partial Conclusions

The morphological, structural, compositional, and spectroscopic characterization of the materials obtained from the thermal polymerization of melamine evidenced the progressive formation of nitrogen-rich structures, culminating in the synthesis of graphitic carbon nitride (g-C_3N_4) at 550 °C. From a morphological standpoint, FE-SEM images revealed an aggregated and irregular structure across the samples, with little variation as a function of treatment temperature. Elemental analysis by EDX confirmed the exclusive presence of carbon and nitrogen in all samples.

Fourier-transform infrared spectroscopy (FTIR) allowed monitoring of the polycondensation process, with a systematic reduction of the vibrations associated with NH_2

groups and strengthening of the characteristic bands of the C=N/C–N skeleton and the heptazine ring. The XRD patterns corroborated the formation of the desired polymeric phase, with the progressive appearance of peaks at ~13.1° and ~27.4° 2θ, assigned to the (100) and (002) planes of g-C_3N_4. The more pronounced intensity of these peaks in sample M55 indicates that thermal treatment at 550 °C favors the formation of the g-C_3N_4 structure.

Finally, Raman spectroscopy complemented the structural analyses by clearly distinguishing the conversion of the melamine precursor into g-C_3N_4. The sample calcined at 550 °C exhibited broad and intense bands consistent with vibrational modes of a graphitic network, whereas the untreated sample showed the sharp, well-defined modes typical of triazine.

Taken together, the results demonstrate that 550 °C is the optimal temperature to promote the efficient conversion of melamine into g-C_3N_4, yielding a material with high purity, structural organization, and vibrational characteristics consistent with those described in the literature for graphitic carbon nitride.

5 GENERAL CONCLUSIONS

This dissertation established a detailed processing–structure–property map for WO_{3-x} thin films and g-C_3N_4 powders, the two constituents envisioned for a future Z-scheme photoelectrode dedicated to solar-to-hydrogen conversion. Although fabrication of the WO_{3-x}/g-C_3N_4 heterostructure could not be completed within the experimental timeframe, the systematic exploration of each material delivers a robust knowledge base that will guide subsequent coupling and optimization steps.

For WO_{3-x} films, continuous modulation of the O_2 flow during reactive sputtering revealed a non-linear regime dominated by oxygen-vacancy chemistry. Intermediate flows of 6–8 sccm maximized γ-monoclinic crystallinity, enhanced surface polarity, and minimized charge-transfer resistance, producing the highest specific capacitance, energy density, and photocurrent under AM 1.5 G illumination. Subsequent annealing in ambient air partially leveled the stoichiometric gradient, underscoring the need for inert atmospheres when vacancy profiles must be preserved.

The Reactive Gas Pulsing Process (RGPP) introduced an additional control lever. A 90 % duty cycle generated transparent, columnar films, whereas a 60 % duty cycle produced denser, more reduced layers. Substrate selection proved decisive: glass fostered Na_2WO_4 formation after annealing, while FTO served as an alkali barrier and preserved phase-pure WO_3.

By jointly tuning duty cycle, annealing atmosphere, and substrate, it becomes possible to engineer vacancy gradients and multiphase architectures that tailor band alignment in future junctions.

Thermal polycondensation of melamine up to 550 °C yielded g-C_3N_4 powders with well-defined (100) and (002) XRD reflections and characteristic Raman modes. Although the resulting powders remain predominantly multilayer, their structural order offers a strong foundation for subsequent exfoliation or functionalization aimed at improving conductivity or interfacial contact.

Across both materials, photoelectrochemical performance proved highly sensitive to the balance between crystalline order and defect density. This balance informs clear coupling guidelines: employ moderately reduced WO_{3-x} (either grown at 6–8 sccm O_2 or at 90 % and 60% of P, annealed in Ar) to maintain efficient hole transport without excessive recombination; deposit g-C_3N_4 at 550 °C on WO_{3-x}; and select diffusion-barrier substrates such as FTO to prevent alkali contamination. These recommendations pave the way for fabricating durable, high-efficiency composite photoelectrodes and provide a sound basis for future investigations into interface energetics, *in-situ* band alignment, and long-term device stability.

In summary, the work achieves two milestones: it delineates optimized synthesis windows and performance correlations for isolated WO_{3-x} and g-C_3N_4, and it specifies the critical requirements for integrating these materials into composite photoelectrodes. These advances lay firm groundwork for forthcoming efforts to unite WO_{3-x} and g-C_3N_4 in Z-scheme architectures capable of efficient, stable, and economically viable solar hydrogen production.

6 PERSPECTIVES

Based on the results obtained and the analyses carried out in this work, the following future studies are proposed:

- To deposit g-C_3N_4 films using techniques such as spin coating and perform their photoelectrochemical characterization, aiming to evaluate the individual response of the material prior to heterostructure formation.
- To fabricate Z-scheme heterostructures by depositing g-C_3N_4 onto WO_{3-x} films prepared with oxygen gradients of 6 and 8 sccm, in order to investigate the synergistic effects of charge transport and band alignment using electrochemical and spectroscopic techniques.

- To characterize the samples produced via the Reactive Gas Pulsing Process (RGPP), with duty cycles of 60% and 90% of the period, after thermal treatment in an inert (argon) atmosphere, aiming to evaluate the impact of this treatment on the structural and photoelectrochemical properties of the films.
- To fabricate heterostructures also using WO_{3-x} films obtained via RGPP with 60% and 90% duty cycles, in order to explore the impact of periodic oxygen modulation on interfacial performance and charge separation within the heterojunction.
- To assess the influence of deposition order by investigating the possibility of using g-C_3N_4 as the bottom layer and WO_{3-x} as the top layer, with the goal of exploring new interfacial interactions and potential structural reorganization.

7 BIBLIOGRAPHY

[1] S.D. Tilley, Recent Advances and Emerging Trends in Photo-Electrochemical Solar Energy Conversion, Adv Energy Mater 9 (2019) 1802877. https://doi.org/10.1002/AENM.201802877.

[2] U. Energy Information Administration, International Energy Outlook 2020 (IEO2020), (n.d.). www.eia.gov (accessed May 30, 2025).

[3] N.S. Lewis, D.G. Nocera, Powering the planet: Chemical challenges in solar energy utilization, Proc Natl Acad Sci U S A 103 (2006) 15729–15735. https://doi.org/10.1073/PNAS.0603395103/ASSET/3DE8043E-D8A1-44B0-AFD0-FD0C4CC001CE/ASSETS/GRAPHIC/ZPQ03906360600E4.JPEG.

[4] R.M. Navarro Yerga, M. Consuelo Álvarez Galván, F. del Valle, J.A. Villoria de la Mano, J.L.G. Fierro, Water Splitting on Semiconductor Catalysts under Visible-Light Irradiation, ChemSusChem 2 (2009) 471–485. https://doi.org/10.1002/CSSC.200900018.

[5] O. Oruc, I. Dincer, Assessing the potential of thermo-chemical water splitting cycles: A bridge towards clean and sustainable hydrogen generation, Fuel 286 (2021) 119325. https://doi.org/10.1016/J.FUEL.2020.119325.

[6] J.L. Sloop, LIQUID HYDROGEN AS A PROPULSION FUEL, 1959.

[7] Z. Chen, H.N. Dinh, E. Miller, Photoelectrochemical water splitting: standards, experimental methods, and protocols, (2013) 126. https://doi.org/10.1007/978-1-4614-8298-7.

[8] M. Damiá N Monllor-Satoca, I. Dí Ez-Garcí, T. Lana-Villarreal, R. Gó Mez, Photoelectrocatalytic production of solar fuels with semiconductor oxides: materials, activity and modeling, 12272 | Chem. Commun 56 (2020) 12272. https://doi.org/10.1039/d0cc04387g.

[9] B.A. Pinaud, J.D. Benck, L.C. Seitz, A.J. Forman, Z. Chen, T.G. Deutsch, B.D. James, K.N. Baum, G.N. Baum, S. Ardo, H. Wang, E. Miller, T.F. Jaramillo, Technical and economic feasibility of centralized facilities for solar hydrogen production via photocatalysis and photoelectrochemistry, Cite This: Energy Environ. Sci (2013). https://doi.org/10.1039/c3ee40831k.

[10] T.J. Jacobsson, Photoelectrochemical water splitting: an idea heading towards obsolescence?, Cite This: Energy Environ. Sci 11 (2018) 1977–1979. https://doi.org/10.1039/c8ee00772a.

[11] R. Sathre, C.D. Scown, W.R. Morrow, J.C. Stevens, I.D. Sharp, J.W. Ager, K. Walczak, F.A. Houle, J.B. Greenblatt, Life-cycle net energy assessment of large-scale hydrogen production via photoelectrochemical water splitting †, 7 (2014) 3089–3444. https://doi.org/10.1039/c4ee01019a.

[12] P. Zhai, S. Haussener, J. Ager, R. Sathre, K. Walczak, J. Greenblatt, T. Mckone, Net primary energy balance of a solar-driven photoelectrochemical water-splitting device, (n.d.). https://doi.org/10.1039/c3ee40880a.

[13] A. Fujishima, K. Honda, Electrochemical Photolysis of Water at a Semiconductor Electrode, Nature 1972 238:5358 238 (1972) 37–38. https://doi.org/10.1038/238037a0.

[14] W. Yang, R. Ramanujam Prabhakar, J. Tan, S. David Tilley, J. Moon, Strategies for enhancing the photocurrent, photovoltage, and stability of photoelectrodes for photoelectrochemical water splitting, Chem. Soc. Rev 48 (2019) 4979. https://doi.org/10.1039/c8cs00997j.

[15] Y.H. Chiu, T.H. Lai, M.Y. Kuo, P.Y. Hsieh, Y.J. Hsu, Photoelectrochemical cells for solar hydrogen production: Challenges and opportunities, APL Mater 7 (2019) 80901. https://doi.org/10.1063/1.5109785/123144.

[16] O. Khaselev, J.A. Turner, A Monolithic Photovoltaic-Photoelectrochemical Device for Hydrogen Production via Water Splitting, Science (1979) 280 (1998) 425–427. https://doi.org/10.1126/SCIENCE.280.5362.425.

[17] M.H. Lee, K. Takei, J. Zhang, R. Kapadia, M. Zheng, Y.-Z. Chen, J. Nah, T.S. Matthews, Y.-L. Chueh, J.W. Ager, A. Javey, p-Type InP Nanopillar Photocathodes for Efficient Solar-Driven Hydrogen Production**, (n.d.). https://doi.org/10.1002/anie.201203174.

[18] H. Kumagai, T. Minegishi, N. Sato, T. Yamada, J. Kubota, K. Domen, Efficient solar hydrogen production from neutral electrolytes using surface-modified Cu(In,Ga)Se 2 photocathodes †, (2015). https://doi.org/10.1039/c5ta01058f.

[19] G. Gunawan, W. Septina, S. Ikeda, T. Harada, T. Minegishi, K. Domen, M. Matsumura, Platinum and indium sulfide-modified $CuInS_2$as efficient photocathodes for photoelectrochemical water splitting, Chem. Commun. 50 (2014) 8941–8943. https://doi.org/10.1039/C4CC03634D.

[20] S. Bandi, A.K. Srivastav, Review: Oxygen-deficient tungsten oxides, J Mater Sci 56 (2021) 6615–6644. https://doi.org/10.1007/s10853-020-05757-2.

[21] M. Desseigne, N. Dirany, V. Chevallier, M. Arab, Shape dependence of photosensitive properties of WO 3 oxide for photocatalysis under solar light irradiation, Appl Surf Sci 483 (2019) 313–323. https://doi.org/10.1016/j.apsusc.2019.03.269.

[22] A. Aljuaid, M. Almehmadi, A.A. Alsaiari, M. Allahyani, O. Abdulaziz, A. Alsharif, J.A. Alsaiari, M. Saih, R.T. Alotaibi, I. Khan, g-C_3N_4 Based Photocatalyst for the Efficient Photodegradation of Toxic Methyl Orange Dye: Recent Modifications and Future Perspectives, Molecules 28 (2023). https://doi.org/10.3390/molecules28073199.

[23] M.B. Costa, M.A. de Araújo, M.V. de L. Tinoco, J.F. de Brito, L.H. Mascaro, Current trending and beyond for solar-driven water splitting reaction on WO_3 photoanodes, Journal of Energy Chemistry 73 (2022) 88–113. https://doi.org/10.1016/j.jechem.2022.06.003.

[24] L. Xie, X. Wang, Z. Zhang, Y. Ma, T. Du, R. Wang, J. Wang, Photosynthesis of Hydrogen Peroxide Based on g-C_3N_4: The Road of a Cost-Effective Clean Fuel Production, Small 19 (2023). https://doi.org/10.1002/smll.202301007.

[25] W. Wang, X. Liu, Z. Li, H. Luo, Z. Meng, H. Wang, W. Chen, J. Chen, R. Chen, Q. He, Efficiency and mechanistic insights of photocatalytic degradation and sterilization utilizing g-C_3N_4/WO_{3-x} Z-scheme heterojunction under full-spectrum light, J Environ Chem Eng 12 (2024). https://doi.org/10.1016/j.jece.2024.114392.

[26] Z. Ashfaq, T. Iqbal, H. Ali, S.M. Eldin, M. Mahtab Alam, F.F. Al-Harbi, M. Arshad, A.M. Galal, Review of different CdS/TiO_2 and WO_3/ g-C_3N_4 composite based photocatalyst for hydrogen production, Arabian Journal of Chemistry 16 (2023). https://doi.org/10.1016/j.arabjc.2023.105024.

[27] M.I. Nabeel, D. Hussain, N. Ahmad, M. Najam-Ul-Haq, S.G. Musharraf, Recent advancements in the fabrication and photocatalytic applications of graphitic carbon

nitride-tungsten oxide nanocomposites, Nanoscale Adv 5 (2023) 5214–5255. https://doi.org/10.1039/d3na00159h.

[28] P. Longchin, T.T. Gebremariam, N. Kunthakudee, A. Thoumrungroj, T. Sutthiphong, M. Hunsom, Structural modification of defective WO_3 by g-C_3N_4 for photocatalytic gold recovery from non-cyanide-based plating effluent, Sci Rep 15 (2025) 1806. https://doi.org/10.1038/s41598-024-81928-4.

[29] T. Yao, X. An, H. Han, J.Q. Chen, C. Li, Photoelectrocatalytic Materials for Solar Water Splitting, Adv Energy Mater 8 (2018) 1800210. https://doi.org/10.1002/AENM.201800210.

[30] A. Polman, H.A. Atwater, Photonic design principles for ultrahigh-efficiency photovoltaics, Nature Publishing Group 11 (2012). https://doi.org/10.1038/nmat3263.

[31] X. Xu, M. Arab Pour Yazdi, J.Y. Rauch, R. Salut, A. Billard, V. Potin, N. Martin, Tungsten Oxide Thin Films Sputter Deposited by the Reactive Gas Pulsing Process for the Dodecane Detection, in: Mater Today Proc, Elsevier Ltd, 2015: pp. 4656–4663. https://doi.org/10.1016/j.matpr.2015.09.019.

[32] A.K. Bhojani, M. Jha, A. Joshi, K. Bhargava, G. Singh, D.K. Singh, S. Pathak, V. Kaushik, Layered transition metal oxides (MoO_3, WO_3, Ga_2O_3, V_2O_5) for energy conversion and storage: A comprehensive review, J Energy Storage 107 (2025). https://doi.org/10.1016/j.est.2024.114979.

[33] E. Muslu, E. Eren, A.U. Oksuz, Research progress on flexible WO_3 based thin film electrodes for supercapacitor applications: a comprehensive review, Emergent Mater (2024). https://doi.org/10.1007/s42247-024-00760-8.

[34] S. Gonçalves, P. Quitério, J. Freitas, D. Ivanou, T. Lopes, A. Mendes, J.P. Araújo, C.T. Sousa, A. Apolinário, Unveiling Morphology-Structure Interplay on Hydrothermal WO3 Nanoplatelets for Photoelectrochemical Solar Water Splitting, ACS Appl Mater Interfaces (2024). https://doi.org/10.1021/acsami.4c11729.

[35] Z. Ni, Q. Wang, Y. Guo, H. Liu, Q. Zhang, Research Progress of Tungsten Oxide-Based Catalysts in Photocatalytic Reactions, Catalysts 13 (2023). https://doi.org/10.3390/catal13030579.

[36] N. Dirany, M. Arab, V. Madigou, C. Leroux, J.R. Gavarri, A facile one step route to synthesize WO_3 nanoplatelets for CO oxidation and photodegradation of RhB: Microstructural, optical and electrical studies, RSC Adv 6 (2016) 69615–69626. https://doi.org/10.1039/c6ra13500e.

[37] O. Samuel, M.H.D. Othman, R. Kamaludin, O. Sinsamphanh, H. Abdullah, M.H. Puteh, T.A. Kurniawan, WO_3–based photocatalysts: A review on synthesis, performance enhancement and photocatalytic memory for environmental applications, Ceram Int 48 (2022) 5845–5875. https://doi.org/10.1016/J.CERAMINT.2021.11.158.

[38] G. Hodes, D. Cahen, J. Manassen, Tungsten trioxide as a photoanode for photoelectrochemical cell (PEC), Nature 260 (1976) 312–313.

[39] J. Feng, X. Zhao, B. Zhang, G. Yang, Q. Qian, S.S.K. Ma, Z. Chen, Z. Li, Y. Huang, Sol-gel synthesis of highly reproducible WO_3 photoanodes for solar water oxidation, Sci China Mater 63 (2020) 2261–2271. https://doi.org/10.1007/s40843-020-1430-4.

[40] Y. Li, W. Zhou, D. Li, J. Xu, Multifunctional non-stoichiometric tungsten oxides: Synthesis, properties and application, J Power Sources 631 (2025). https://doi.org/10.1016/j.jpowsour.2025.236222.

[41] X. Liu, F. Wang, Q. Wang, Nanostructure-based WO_3 photoanodes for photoelectrochemical water splitting, Physical Chemistry Chemical Physics 14 (2012) 7894–7911. https://doi.org/10.1039/c2cp40976c.

[42] J. Zhang, P. Zhang, T. Wang, J. Gong, Monoclinic WO_3 nanomultilayers with preferentially exposed (002) facets for photoelectrochemical water splitting, Nano Energy 11 (2015) 189–195. https://doi.org/10.1016/j.nanoen.2014.10.021.

[43] R. Barathy T, P.V.K. Yadav, A. Mondal, B. Ajitha, J. Jarugala, Y.A. Kumar Reddy, High porosity and oxygen vacancy enriched WO_{3-x} tr hin films for room temperature hydrogen gas sensors, Int J Hydrogen Energy 50 (2024) 878–888. https://doi.org/10.1016/j.ijhydene.2023.07.218.

[44] C. Chananonnawathorn, S. Pudwat, M. Horprathum, P. Eiamchai, P. Limnontakul, C. Salawan, K. Aiempanakit, Electrochromic property dependent on oxygen gas flow rate and films thickness of sputtered WO_3 films, in: Procedia Eng, Elsevier Ltd, 2012: pp. 752–758. https://doi.org/10.1016/j.proeng.2012.02.008.

[45] N. Martin, A.R. Bally, P. Hones, R. Sanjines, F. Levy´´, L. Levy´´, High rate and process control of reactive sputtering by gas pulsing: the TiO system, 2000.

[46] X. Xu, M.A.P. Yazdi, R. Salut, J.M. Cote, A. Billard, N. Martin, Structure, composition and electronic transport properties of tungsten oxide thin film sputter-deposited by the reactive gas pulsing process, Mater Chem Phys 205 (2018) 391–400. https://doi.org/10.1016/j.matchemphys.2017.11.048.

[47] N. Martin, J.M. Cote, J. Gavoille, J.Y. Rauch, Titanium oxynitride thin films by the reactive sputtering process with an independent pulsing of O_2 and N_2 gases, Thin Solid Films 796 (2024). https://doi.org/10.1016/j.tsf.2024.140340.

[48] L. Pirker, B. Višić, Recent Progress in the Synthesis and Potential Applications of Two-Dimensional Tungsten (Sub)oxides, Isr J Chem 62 (2022). https://doi.org/10.1002/ijch.202100074.

[49] Y. Liu, L. Kong, X. Guo, J. Xu, S. Shi, L. Li, Surface oxygen vacancies on WO_3 nanoplate arrays induced by Ar plasma treatment for efficient photoelectrochemical water oxidation, Journal of Physics and Chemistry of Solids 149 (2021). https://doi.org/10.1016/j.jpcs.2020.109823.

[50] J. Zhang, X. Chang, C. Li, A. Li, S. Liu, T. Wang, J. Gong, WO_3 photoanodes with controllable bulk and surface oxygen vacancies for photoelectrochemical water oxidation, J Mater Chem A Mater 6 (2017) 3350–3354. https://doi.org/10.1039/c7ta10056f.

[51] F. Zhan, Y. Liu, K. Wang, X. Yang, M. Liu, X. Qiu, J. Li, W. Li, Oxygen-Deficient Nanofiber WO_{3-x}/WO_3 Homojunction Photoanodes Synthesized via a Novel Metal Self-Reducing Method, ACS Appl Mater Interfaces 11 (2019) 39951–39960. https://doi.org/10.1021/acsami.9b13326.

[52] R. Cheng, X. Niu, H. Li, H. Liang, P. Tsiakaras, Oxygen vacancy-rich defective tungsten oxide (WO_{3-x}) modified by Prussian blue for efficient photocatalytic carbon dioxide conversion and tetracycline degradation, J Colloid Interface Sci 683 (2025) 807–816. https://doi.org/10.1016/j.jcis.2024.12.146.

[53] Y. Cheng, Z. Li, X. Yang, Enhanced CO_2 Photoreduction Performance of WO_{3-x}, Catalysts 15 (2025). https://doi.org/10.3390/catal15010013.

[54] W.J. Ong, L.L. Tan, Y.H. Ng, S.T. Yong, S.P. Chai, Graphitic Carbon Nitride (g-C_3N_4)-Based Photocatalysts for Artificial Photosynthesis and Environmental Remediation: Are We a Step Closer to Achieving Sustainability?, Chem Rev 116 (2016) 7159–7329. https://doi.org/10.1021/acs.chemrev.6b00075.

[55] S.K. Sharma, A. Kumar, G. Sharma, T. Wang, A. Iglesias-Juez, P. Dhiman, Recent advances in g-C_3N_4/Metal organic frameworks heterojunctions for high-performance photocatalytic environmental remediation and energy production, J Mol Liq 382 (2023). https://doi.org/10.1016/j.molliq.2023.121890.

[56] A.H. Navidpour, D. Hao, X. Li, D. Li, Z. Huang, J.L. Zhou, Key factors in improving the synthesis and properties of visible-light activated g-C_3N_4 for photocatalytic hydrogen

production and organic pollutant decomposition, Catal Rev Sci Eng (2023). https://doi.org/10.1080/01614940.2023.2228130.

[57] A. V. Zhurenok, D.B. Vasilchenko, E.A. Kozlova, Comprehensive Review on g-C_3N_4-Based Photocatalysts for the Photocatalytic Hydrogen Production under Visible Light, Int J Mol Sci 24 (2023). https://doi.org/10.3390/ijms24010346.

[58] W. Zhu, Y. Yue, H. Wang, B. Zhang, R. Hou, J. Xiao, X. Huang, A. Ishag, Y. Sun, Recent advances on energy and environmental application of graphitic carbon nitride (g-C_3N_4)-based photocatalysts: A review, J Environ Chem Eng 11 (2023). https://doi.org/10.1016/j.jece.2023.110164.

[59] P. Molaei, F. Rahimi-Moghadam, Porous g-C_3N_4 nanosheets through facile thermal polymerization of melamine in the air for photocatalyst application, Journal of Materials Science: Materials in Electronics 32 (2021) 19655–19666. https://doi.org/10.1007/s10854-021-06488-z.

[60] A. Alaghmandfard, K. Ghandi, A Comprehensive Review of Graphitic Carbon Nitride (g-C_3N_4)–Metal Oxide-Based Nanocomposites: Potential for Photocatalysis and Sensing, Nanomaterials 12 (2022). https://doi.org/10.3390/nano12020294.

[61] G. Zhang, J. Zhang, M. Zhang, X.W.-J. of M. Chemistry, undefined 2012, Polycondensation of thiourea into carbon nitride semiconductors as visible light photocatalysts, Pubs.Rsc.OrgG Zhang, J Zhang, M Zhang, X WangJournal of Materials Chemistry, 2012•pubs.Rsc.Org (n.d.). https://doi.org/10.1039/c2jm00097k.

[62] L. Zheng, Y. Wei, C. Wang, H. Liu, L. Li, M. Huang, Y. Huang, L. Fan, J. Wu, Construction of direct WO_3/g-C_3N_4 Z-scheme heterojunction for degrading flotation agent effectively, Ceram Int 50 (2024) 38860–38870. https://doi.org/10.1016/j.ceramint.2024.07.310.

[63] F. Su, M. Tian, H. Cao, Z. Wang, Q. Zhao, H. Xie, Y. Zhang, X. Jin, X. Li, Z. Li, Constructing a Z-scheme heterojunction of oxygen-deficient WO_{3-x} and g-C_3N_4 for superior photocatalytic evolution of H_2, Surfaces and Interfaces 55 (2024). https://doi.org/10.1016/j.surfin.2024.105346.

[64] J. Chen, Z. Yang, S.Y. Xie, F. Gong, K. Xie, Y.H. Zhang, Ultrathin 2D[sbnd]2D WO_{3-x}-C_3N_4 heterostructure-based high-efficiency photocatalyst for selective oxidation of toluene, Diam Relat Mater 149 (2024). https://doi.org/10.1016/j.diamond.2024.111534.

[65] R. Wang, X. Fu, Y. Guo, J. Zhang, R. Chen, X. Huang, Q. Tian, Y. Bai, WO_3/g-C_3N_4 synergistic photocatalysts for degradation and H_2 production, Ceram Int (2024). https://doi.org/10.1016/j.ceramint.2024.10.442.

[66] Y. Lu, S. Gao, T. Ma, J. Zhang, H. Liu, W. Zhou, A Z-Scheme Heterojunction g-C_3N_4/WO_3 for Efficient Photodegradation of Tetracycline Hydrochloride and Rhodamine B, Nanomaterials 15 (2025). https://doi.org/10.3390/nano15050410.

[67] J.T. Gudmundsson, Physics and technology of magnetron sputtering discharges, Plasma Sources Sci Technol 29 (2020). https://doi.org/10.1088/1361-6595/ABB7BD.

[68] R. Garg, S. Gonuguntla, S. Sk, M.S. Iqbal, A.O. Dada, U. Pal, M. Ahmadipour, Sputtering thin films: Materials, applications, challenges and future directions, Adv Colloid Interface Sci 330 (2024) 103203. https://doi.org/10.1016/J.CIS.2024.103203.

[69] C. Karthik, S.C. Sarngadharan, V. Thomas, Low-Temperature Plasma Techniques in Biomedical Applications and Therapeutics: An Overview, Int J Mol Sci 25 (2023) 524. https://doi.org/10.3390/IJMS25010524.

[70] A. Le Bail, Whole powder pattern decomposition methods and applications: A retrospection, Powder Diffr 20 (2005) 316–326. https://doi.org/10.1154/1.2135315.

[71] A. Le Bail, H. Duroy, J.L. Fourquet, Ab-initio structure determination of $LiSbWO_6$ by X-ray powder diffraction, Mater Res Bull 23 (1988) 447–452. https://doi.org/10.1016/0025-5408(88)90019-0.

[72] X. XU, Nanostructured W-O thin films by reactive sputtering: application as gas sensors, Université Bourgogne Franche-Comté, 2018.

[73] J. Olejníček, A. Hrubantová, L. Volfová, M. Dvořáková, M. Kohout, D. Tvarog, O. Gedeon, H. Wulff, R. Hippler, Z. Hubička, WO_3 and WO_{3-x} thin films prepared by DC hollow cathode discharge, Vacuum 195 (2022). https://doi.org/10.1016/j.vacuum.2021.110679.

[74] A. Hrubantova, R. Hippler, H. Wulff, M. Cada, J. Olejnicek, N. Nepomniashchaia, C.A. Helm, Z. Hubicka, Deposition of tungsten oxide films by reactive magnetron sputtering on different substrates, Journal of Vacuum Science & Technology A 40 (2022). https://doi.org/10.1116/6.0002012.

[75] S. Singh, P. Gurawal, G. Malik, D. Kaur, R. Chandra, Temperature-dependent wetting and other physical characteristics of sputtered grown WO_3 thin films, (2024). https://doi.org/10.1007/s12034-024-03243-yS.

[76] A. Hrubantova, R. Hippler, H. Wulff, M. Cada, J. Olejnicek, N. Nepomniashchaia, C.A. Helm, Z. Hubicka, Deposition of tungsten oxide films by reactive magnetron sputtering on different substrates, Journal of Vacuum Science & Technology A 40 (2022). https://doi.org/10.1116/6.0002012.

[77] R. Azimirad, N. Naseri, O. Akhavan, A.Z. Moshfegh, Hydrophilicity variation of WO_3 thin films with annealing temperature, J Phys D Appl Phys 40 (2007) 1134–1137. https://doi.org/10.1088/0022-3727/40/4/034.

[78] M. Miyauchi, M. Shibuya, Z.G. Zhao, Z. Liu, Surface wetting behavior of a WO_3 electrode under light-irradiated or potential-controlled conditions, Journal of Physical Chemistry C 113 (2009) 10642–10646. https://doi.org/10.1021/jp901097b.

[79] T. Degen, M. Sadki, E. Bron, U. König, G. Nénert, The high score suite, in: Powder Diffr, Cambridge University Press, 2014: pp. S13–S18. https://doi.org/10.1017/S0885715614000840.

[80] N. Dirany, M. Arab, C. Leroux, S. Villain, V. Madigou, J.R. Gavarri, Effect of WO_3 Nanoparticles Morphology on the Catalytic Properties, in: Mater Today Proc, Elsevier Ltd, 2016: pp. 230–234. https://doi.org/10.1016/j.matpr.2016.01.062.

[81] C. Shao, A.S. Malik, J. Han, D. Li, M. Dupuis, X. Zong, C. Li, Oxygen vacancy engineering with flame heating approach towards enhanced photoelectrochemical water oxidation on WO_3 photoanode, Nano Energy 77 (2020). https://doi.org/10.1016/j.nanoen.2020.105190.

[82] L.D. Zhao, Q. Zhang, J. Bin Fan, L.Q. Yin, P.W. Qi, H.C. Yao, Z.J. Li, Improvement of the photoelectrochemical performance of vertically aligned WO_3 nanosheet array film with a disordered surface layer by electroreduction, Journal of Solid State Electrochemistry 23 (2019) 1621–1630. https://doi.org/10.1007/s10008-019-04257-x.

[83] Ł. Haryński, A. Olejnik, K. Grochowska, K. Siuzdak, A facile method for Tauc exponent and corresponding electronic transitions determination in semiconductors directly from UV–Vis spectroscopy data, Opt Mater (Amst) 127 (2022). https://doi.org/10.1016/j.optmat.2022.112205.

[84] S. Jain, A. Sanger, S. Chauhan, R. Chandra, Hydrogen sensing properties of nanostructured Pd/WO_3 thin films: Role of hydrophobicity during recovery process, Mater Res Express 1 (2014). https://doi.org/10.1088/2053-1591/1/3/035046.

[85] C.G. Granqvist, Handbook of Inorganic Electrochromic Materials, Elsevier Science, 1995. https://doi.org/https://doi.org/10.1016/B978-0-444-89930-9.X5000-4.

[86] J. Liu, S.M. Xu, Y. Li, R. Zhang, M. Shao, Facet engineering of WO_3 arrays toward highly efficient and stable photoelectrochemical hydrogen generation from natural seawater, Appl Catal B 264 (2020). https://doi.org/10.1016/j.apcatb.2019.118540.

[87] J. Zhang, X. Chang, C. Li, A. Li, S. Liu, T. Wang, J. Gong, WO_3 photoanodes with controllable bulk and surface oxygen vacancies for photoelectrochemical water

oxidation, J Mater Chem A Mater 6 (2018) 3350–3354. https://doi.org/10.1039/c7ta10056f.

[88] Y. Wang, W. Tian, C. Chen, W. Xu, L. Li, Tungsten Trioxide Nanostructures for Photoelectrochemical Water Splitting: Material Engineering and Charge Carrier Dynamic Manipulation, Adv Funct Mater 29 (2019). https://doi.org/10.1002/adfm.201809036.

[89] X. Yuan, K. Luo, K. Zhang, J. He, Y. Zhao, D. Yu, Combinatorial vibration-mode assignment for the FTIR spectrum of crystalline melamine: A strategic approach toward theoretical IR vibrational calculations of triazine-based compounds, Journal of Physical Chemistry A 120 (2016) 7427–7433. https://doi.org/10.1021/acs.jpca.6b06015.

[90] S. Sunasee, K.H. Leong, K.T. Wong, G. Lee, S. Pichiah, I.W. Nah, B.H. Jeon, Y. Yoon, M. Jang, Sonophotocatalytic degradation of bisphenol A and its intermediates with graphitic carbon nitride, Environmental Science and Pollution Research 26 (2019) 1082–1093. https://doi.org/10.1007/s11356-017-8729-7.

[91] K. Li, M. Chen, L. Chen, S. Zhao, W. Xue, Z. Han, Y. Han, Synthesis of g-C_3N_4 Derived from Different Precursors for Photodegradation of Sulfamethazine under Visible Light, Processes 11 (2023). https://doi.org/10.3390/pr11020528.

[92] S. Jain, A. Sanger, S. Chauhan, R. Chandra, Hydrogen sensing properties of nanostructured Pd/WO_3 thin films: Role of hydrophobicity during recovery process, Mater Res Express 1 (2014). https://doi.org/10.1088/2053-1591/1/3/035046.

FOLHA DE REGISTRO DO DOCUMENTO

1. CLASSIFICAÇÃO/TIPO	2. DATA	3. REGISTRO N°	4. N° DE PÁGINAS
DM	01 de agosto de 2025	DCTA/ITA/DM-043/2025	104

5. TÍTULO E SUBTÍTULO:

Study of $WO_{3-X\ and}$ g-C_3N_4 photoelectrodes aimed at application in solar hydrogen generation

6. AUTOR(ES):

Helen Caroline de Souza Barros

7. INSTITUIÇÃO(ÕES)/ÓRGÃO(S) INTERNO(S)/DIVISÃO(ÕES):

Instituto Tecnológico de Aeronáutica - ITA

8. PALAVRAS-CHAVE SUGERIDAS PELO AUTOR:

Photoelectrodes; Magnetron Sputtering; Oxygen Gradient; Reactive Gas Pulsing Process; Green Hydrogen.

9.PALAVRAS-CHAVE RESULTANTES DE INDEXAÇÃO:

Pulverização por magnétron; Eletrodos; Hidrogênio; Conversão de energia; Difração por raios x; Microscopia eletrônica; Materiais semicondutores; Física de plasmas; Física.

10. APRESENTAÇÃO: **(X) Nacional ( ) Internacional**

ITA, São José dos Campos. Curso de Mestrado. Programa de Pós-Graduação em Física. Área de Física de Plasmas. Orientador: André Luis de Jesus Pereira; coorientador: Argemiro Soares da Silva Sobrinho. Defesa em 03/07/2025. Publicada em 2025.

11. RESUMO:

The direct conversion of solar energy into hydrogen through photoelectrochemical (PEC) cells has emerged as one of the most promising strategies for decarbonizing the energy sector, as it integrates into a single device photon harvesting, charge separation, and the hydrogen/oxygen evolution reactions. However, the overall efficiency of these systems remains limited by factors such as low spectral absorption, rapid electron–hole recombination, and structural instability of the photoelectrodes. In this context, the present work systematically mapped the relationships between processing conditions, structural features, and the resulting properties of two earth-abundant semiconductors: sub-stoichiometric tungsten oxide (WO_{3-x}) and graphitic carbon nitride (g-C_3N_4), aiming at the future development of Z-scheme photoelectrodes for solar hydrogen production. WO_{3-x} films were deposited by reactive sputtering with O_2 flow gradients (2–10 sccm) and through the Reactive Gas Pulsing Process (RGPP) with duty cycles of 60% and 90% of the period. Characterization by X-ray Diffraction (XRD), Raman spectroscopy, Scanning Electron Microscopy (SEM), Electrochemical Impedance Spectroscopy (EIS), cyclic voltammetry, and Mott–Schottky analyses demonstrated that, although all samples exhibited the γ-monoclinic phase of WO_{3-x}, those obtained with intermediate O_2 flows (6–8 sccm) showed superior photoelectrochemical performance, including lower charge transfer resistance, higher capacitance, energy density, and photocurrent under AM 1.5 G illumination. In the RGPP process, a 90% duty cycle led to the formation of transparent columnar films, while a 60% duty cycle produced denser and more reductive layers. These samples were thermally treated in both ambient air and flowing argon, revealing that the annealing atmosphere significantly influenced their optical transmittance and band gap variations. Upon annealing, sodium-containing glass substrates promoted the formation of Na_2WO_4, whereas Fluorine-doped Tin Oxide (FTO) substrates acted as ionic diffusion barriers, preserving the pure WO_3 phase. g-C_3N_4 powders were obtained by thermal polycondensation of melamine between 400 °C and 550 °C. Only calcination at 550 °C yielded (100)/(002) reflections in XRD and the characteristic Raman modes, indicating an ordered graphitic structure suitable for future film deposition. The results confirm that the photoelectrochemical performance of each material critically depends on the balance between crystalline order and defect density. Based on this, strategic guidelines were established for material coupling: employing moderately reduced WO_{3-x} (6–8 sccm O_2 or 60% and 90% of P thermally treated under argon), depositing g-C_3N_4 at 550 °C onto WO_{3-x}. Although the heterostructure has not yet been completed, this study defines optimal synthesis windows and interfacial requirements that support subsequent stages toward the development of more efficient, stable, and economically viable composite photoelectrodes for the direct conversion of solar energy into green hydrogen.

12. GRAU DE SIGILO:

(X) OSTENSIVO ( ) RESERVADO ( ) SECRETO